

PRECISION MEASUREMENT OF THE ISOTOPIC SHIFT IN
CALCIUM IONS USING PHOTON RECOIL SPECTROSCOPY

FLORIAN GEBERT

Precision measurement of the isotopic shift in calcium ions using photon recoil spectroscopy

Von der QUEST-Leibniz-Forschungsschule
der Gottfried Wilhelm Leibniz Universität Hannover
zur Erlangung des Grades
Doktor der Naturwissenschaften
Dr. rer. nat.
genehmigte Dissertation
von

Dipl.-Phys. Florian Gebert
geboren am 26. Juni 1980 in Braunschweig

2015

Referent: Prof. Dr. Piet O. Schmidt
Korreferent: PD Dr. Ekkehard Peik
Tag der Promotion: 16. Januar 2015

Florian Gebert: *Precision measurement of the isotopic shift in calcium ions using photon recoil spectroscopy*

ABSTRACT

Within the scope of this thesis, precision isotope shift measurements using a new spectroscopy technique were performed. The method is based on quantum logic spectroscopy, where the quantized motional states are utilized to transfer the spectroscopic information onto a second ion, the logic ion. This ion is used for sympathetically cooling and the detection of the spectroscopic signal. Photon recoil spectroscopy extends quantum logic spectroscopy to enable frequency measurements of transitions with relatively short lifetime of the excited state. For further optimizing the developed method, new technologies were investigated, which enable an improved control of the ions in the trap and consequently improve the signal to noise ratio of the spectroscopic technique. On the one hand, new photonic crystal fibers were investigated for single mode guidance of ultraviolet (UV) radiation and implemented in the setup. These fibers enable an improved coherent manipulation of the logic ion through a reduction of intensity fluctuations at the position of the ion. Another improvement was achieved using the technique of stimulated Raman adiabatic passage (STIRAP), where time-dependent laser pulses are used for coherent manipulation of the state of the ion. The technique enables efficient detection of the motional ground state population and consequently improves the expected spectroscopic signal.

After the characterization of the new spectroscopic technique, isotope shift measurements were performed on different calcium isotopes. For this purpose the different ions were isotope-selectively loaded into the trap and successively investigated spectroscopically. The isotope shift is (among others) caused by the change in the nuclear charge radius due to the different number of neutrons in the core. Therefore, measurements of the isotopic shift enable investigations of the structure of the nucleus. For this investigation Ca^+ is an interesting candidate since here two isotopes with so-called magical neutron numbers are stable and naturally abundant. Additionally, the results of the isotope measurements are needed to improve the comparison of laboratory data with astrophysical measurements to reveal possible time and space variations of fundamental constants.

Keywords: Precision spectroscopy, isotope shift, UV single mode fiber

ZUSAMMENFASSUNG

Im Rahmen dieser Dissertation wurden Präzisionsmessungen zur Isotopieverschiebung an Kalzium Ionen mit Hilfe einer neuartigen Spektroskopiemethode durchgeführt. Die Methode beruht auf der Quantenlogikspektroskopie, bei der die quantisierten Bewegungszustände in einer Ionenfalle ausgenutzt werden um die spektroskopische Information auf ein zweites Ion, das Logik Ion, zu übertragen. Dieses Ion dient der Coulomb-vermittelten Laserkühlung sowie der Detektion des spektroskopischen Signals. Mit der Photonenrückstoßspektroskopie wurde die Quantenlogikspektroskopie erweitert um Übergänge mit einer relativ kurzen Lebensdauer des angeregten Zustands vermessen zu können.

Zur weiteren Optimierung der entwickelten Methode wurden neuartige Technologien verwendet um die Kontrolle über die Ionen in der Falle zu verbessern wodurch das Signal-Rausch-Verhältnis der Spektroskopie erhöht werden konnte. Zum einen wurden photonische Kristallfasern auf einmodige Strahlungsleitung im ultravioletten Spektralbereich untersucht und in den Aufbau integriert. Diese Fasern ermöglichen die Verbesserung der kohärenten Manipulation des Logik Ions durch die Reduzierung von Intensitätsschwankungen an der Position des Ions. Eine weitere Verbesserung bietet die Technik des Raman stimulierten adiabatischen Übergangs (engl. Stimulated Raman Adiabatic Passage, **STRAP**), bei der die Zeitabhängigkeit von Laserpulsen zur kohärenten Manipulation ausgenutzt wird um den Zustand des Atoms zu beeinflussen. Die Methode erlaubt eine effektive Detektion der Bevölkerung des Grundzustandes und führt dadurch zu einer Verbesserung des zu erwartenden Spektroskopie Signals.

Nach der Charakterisierung der Methode wurden die Messungen zur Isotopieverschiebung unterschiedlicher Kalzium Isotope durchgeführt. Sie wird unter anderem durch den (aufgrund der geänderten Neutronenzahl) veränderten nuklearen Ladungsradius des Kernes hervorgerufen. Deshalb ermöglichen Messungen der Isotopieverschiebung Aussagen über die Struktur der Atomkerne. Für diese Untersuchungen ist insbesondere Ca^+ eine interessante Spezies, da hier zwei Isotope mit sogenannten magischen Neutronenzahlen stabil sind und natürlich vorkommen. Die gewonnenen Resultate werden ebenfalls zur Verbesserung des Vergleichs von Labordaten mit astronomischen Messungen benötigt, die mögliche zeitliche und räumliche Variationen von fundamentalen Konstanten aufklären sollen.

Schlagerworte: Präzisionsspektroskopie, Isotopieverschiebung, einmodige UV Faser

CONTENTS

List of Figures	xi
1 INTRODUCTION	1
2 THEORETICAL BACKGROUND	7
2.1 Ion trapping	8
2.2 Two ion crystals	10
2.3 Quantum mechanical states of motion in the ion trap	11
2.4 Trapped ion coupled to a classical light field	13
2.5 Three level system coupled with two light fields	17
2.6 summary	19
3 EXPERIMENTAL SETUP	21
3.1 The ion trap	21
3.2 Ionization laser systems	22
3.3 Experimental setup for coherent manipulation	23
3.3.1 Measurement principle and coherence of Raman beams	25
3.4 The calcium spectroscopy laser system	27
3.5 Laser instability	31
3.6 Complete setup	32
4 SINGLE MODE FIBER FOR UV APPLICATIONS	33
4.1 Guiding mechanisms in photonic crystal fibers	34
4.2 Characterization of PCFs	37
4.2.1 Characterization of the output modes of the fibers	38
4.2.2 Loss, bending, and polarization properties	40
4.2.3 Long-time transmission measurement	42
4.3 Application	43
4.4 Conclusions and outlook	46
5 MOTIONAL STATE INDEPENDENT TRANSFER USING STRAP	47
5.1 STIRAP theory	48
5.2 STIRAP simulation and implementation	52
5.2.1 STIRAP simulation	52
5.2.2 Experimental implementation of the STIRAP sequence	53
5.3 STIRAP results	54
5.3.1 Characterization of the STIRAP transfer	54
5.3.2 Motional dependence of the STIRAP transfer	58
5.3.3 Comparison of the transfer efficiency for STIRAP and Rabi oscillations	60
5.4 Discussion	61
6 ISOTOPE SHIFT MEASUREMENTS OF CALCIUM IONS	63
6.1 Isotope shift theory	64
6.2 Isotope-selective loading	68
6.3 Photon recoil spectroscopy	72

6.4	PRS on non-closed transitions	74
6.4.1	Measurement of the transition frequencies	75
6.5	Experimental Results	77
6.5.1	Systematic effects	80
6.6	King plot analysis	82
6.7	summary and outlook	85
7	SUMMARY AND OUTLOOK	87
	BIBLIOGRAPHY	91

LIST OF FIGURES

Figure 1	Schematic of the ion trap.	8
Figure 2	Population of motional states in the ion trap.	12
Figure 3	Relative Rabi frequencies	16
Figure 4	Three level atom coupled to two light fields.	17
Figure 5	Energy scheme and laser wavelength for photo-ionizing the neutral atoms.	22
Figure 6	Relevant level scheme of the $^{25}\text{Mg}^+$ ion and the lasers for coherent manipulation.	23
Figure 7	Vacuum chamber with beam alignment.	24
Figure 8	Off-resonant excitation	26
Figure 9	Calcium level scheme.	28
Figure 10	Electronic circuit for the frequency stabilization of the spectroscopy lasers.	29
Figure 11	Optical setup for the manipulation of the spectroscopy lasers	30
Figure 12	Stability of the spectroscopy laser	31
Figure 13	Complete laser setup needed for PRS.	32
Figure 14	Simulated Rabi oscillations	33
Figure 15	Sketches of different photonic crystal structures.	35
Figure 16	Scanning electron micrographs of the investigated fibers.	37
Figure 17	Fiber test setup.	38
Figure 18	Measured near-field intensity profiles.	39
Figure 19	Attenuation and bending loss measurements.	40
Figure 20	Polarization measurements.	41
Figure 21	Long-time transmission measurement.	42
Figure 22	Beam profile with and without fiber.	43
Figure 23	Measured Raman Rabi oscillations.	45
Figure 24	STIRAP pulse sequence.	49
Figure 25	Eigenenergies and basis of the dressed states.	50
Figure 26	Time dependence of the adiabatic criterion	51
Figure 27	Measured STIRAP sequence.	54
Figure 28	Simulated delay time dependence for the STIRAP sequence.	55
Figure 29	Scan of the delay time between the two STIRAP pulses.	56
Figure 30	Simulated and measured transfer probability for different delay scaling factors and pulse length for carrier transitions.	57

Figure 31	Simulated and measured transfer probability for different delay scaling factors and pulse length for BSB transition. 58
Figure 32	Simulated transfer probability of the population for the lowest 15 motional levels. 59
Figure 33	Scan of the transfer time for a STIRAP pulse sequence 60
Figure 34	Comparison Rabi and Stirap transfer for a thermal distributed state. 61
Figure 35	Modification of the potential energy of the electron due to the non-zero size of the core. 66
Figure 36	Estimated relative ionization probabilities. 68
Figure 37	Mass spectroscopy signal for the different isotopes 70
Figure 38	Photon recoil spectroscopy sequence 71
Figure 39	Pulse timing for photon recoil spectroscopy 72
Figure 40	Excitation during photon recoil spectroscopy. 73
Figure 41	Photon recoil spectroscopy sequence for spectroscopy on non-closed transitions 74
Figure 42	Pulse timing for photon recoil spectroscopy of non-closed transitions. 75
Figure 43	Resonance line scan. 76
Figure 44	Wait time dependence of the spectroscopy signal. 77
Figure 45	Determination of the frequency discriminant 78
Figure 46	Overlapped Allen deviation. 80
Figure 47	King plot of the measured isotope shifts. 83
Figure 48	King plot of isotopic shifts plotted against the nuclear charge radius. 84

LIST OF TABLES

Table 1	Important properties for loading different isotopes of calcium. 69
Table 2	Systematic shifts 81
Table 3	Measured isotope shift of the two investigated transitions 82
Table 4	Comparison of measured and calculated field and mass shift constants 83

Table 5 Extracted change of mean square nuclear charge
radius 85

ACRONYMS

AC	Alternating current
AOM	Acousto-optical modulator
ARROW	Antiresonant reflecting optical waveguide
CERN	European Organization for Nuclear Research
CW	Continuous wave
DC	Direct current
DDS	Direct digital synthesizer
ECDL	Extended cavity diode laser
EOM	Electro-optical modulator
FEM	Finite element method
FWHM	Full width at half maximum
IR	Infrared
PCF	Photonic crystal fiber
PRS	Photon recoil spectroscopy
PTB	Physikalisch Technische Bundesanstalt
QED	Quantum electrodynamics
QLS	Quantum logic spectroscopy
QPN	Quantum projection noise
RAP	Rapid adiabatic passage
RF	Radio frequency
RIN	Relative intensity noise
SEM	Scanning electron micrograph
STIRAP	Stimulated Raman adiabatic passage
TTL	Transistor transistor logic

UV Ultraviolet

VGA Voltage controlled gain amplifier

INTRODUCTION

Spectroscopy is one of the key instruments that provides insight into the structure of atoms and molecules. After the first experiments of the decomposition of visible light using a prism by Newton in the 17th century and later the discovery of dark lines in the spectra of the sun by Fraunhofer [1] at the beginning of the 19th century, Ångström identified bright lines in the spectra of an electric spark. For the first time he assigned them to the substance of the metal electrodes and the gas between them [2] and by that performed the first spectroscopic experiment [3]. By the beginning of the 20th century, spectroscopic experiments were one of the major experimental tools leading to the discoveries of the laws of quantum mechanics. With the invention and further developments of the laser as a monochromatic, tunable, coherent light source, a rapid increase in precision of spectroscopic experiments was achieved and spectroscopy became a prominent tool in the fields of physics, chemistry and medical science [4]. During the last decades, plenty of novel experimental techniques were developed to discover new physical effects and to test fundamental theories, such as the standard model. Higher and higher energies can be used in the experiments to test fundamental theories in energy regions not reached before. One prominent example of this approach is the discovery of the Higgs Boson at CERN in 2012 [5]. Another strategy to discover new physical effects is to investigate rare substances or elements. Here, for example isotopes with a short lifetime can be investigated to determine the structure of unstable nuclei. This led to the discovery of halo neutrons, that reside far away from the nuclear core and whose interaction with the core are not yet fully understood [6, 7]. A third approach to explore the limits of today's physical models is to perform spectroscopy on atomic properties with extremely high accuracy. One may detect small deviations from theoretical predictions and explore the limits of current theories. One prerequisite for high precision spectroscopy experiments is the accurate control of the environment of the investigated atoms or ions. Trapping of ions in electrical fields [8] or atoms in optical dipole traps (at the so called "magical wavelength") enabled measurements in a well controlled environment. After the first implementation of laser cooling [9, 10] to reduce Doppler broadening and shifts obscuring the measured spectra, these traps became an ideal tool to perform high precision measurements of atomic transition frequencies. Different techniques were developed to cool the ions further below the Doppler cooling limit [11, 12]. Furthermore, for trapped ions, side-

band cooling [13, 14] can be used to prepare the ion in the motional groundstate of the trap potential. Through laser cooling the Lamb-Dicke regime can be reached, where the ions are strongly localized in the trap, and transitions changing their motional state are strongly suppressed, thus enabling recoil free detection of the ion's transition frequencies. Therefore, experimental investigations of atomic transitions resolving the natural linewidth were possible, allowing the detection of the center frequency with sub-natural linewidth accuracy. This led to record precision measurements in optical clocks with unprecedented relative inaccuracies [15, 16].

This new level of precision permits the detection of very small quantities, such as the frequency shift caused by the earth's gravitational potential. Measuring the atomic frequency at different positions on earth reveals differences of its potential between these positions. Thus one can map out the earth's gravitational potential using portable optical clocks. Another application of high precision measurements is the search for a variation of fundamental constants to test predictions of fundamental theories. One appropriate observable for testing these variations is the fine-structure constant, which describes the strength of the electromagnetic coupling. Assuming the fine-structure constant changes with time and space, the atomic transition frequencies changes accordingly. To investigate this effect, different strategies can be followed to detect such small frequency variations.

One can compare two highly precise optical clocks using different atomic transitions over long timescales and search for a relative change of the two transition frequencies. Along these lines, recent experiments set a lower bound for a possible temporal variation of the fine-structure constant and the electron-to-proton mass ratio [17, 18, 19]. Another approach is to compare the results of laboratory measurements of different transition frequencies with astrophysical measurements of absorption spectra from interstellar clouds. These absorption lines are imprinted in the emitted light from a quasar detected with large telescopes on earth in the so called quasar absorption spectroscopy [20, 21]. Since it takes on the order of 10^{10} years for the light to reach the earth after traveling through the interstellar cloud, these measurements can be used to compare the transition frequencies from 10^{10} years ago with today's electronic spectra. For this analysis precise laboratory data of the absolute frequencies and isotope shifts of many different species and transitions are required [22]. Using this type of analysis indications of a spatial variation of the fine-structure constant over cosmological length scales have been found [23, 24]. Most of the data used in the analysis was measured using discharge cells. These experiments are not able to resolve the isotope shift of the transitions due to Doppler broadening. Furthermore, the analysis assumes the same abundance of isotopes in the interstellar medium as on earth. Therefore, the determined variation

of the finestructure constant can be mimicked by a change of the isotopic abundances. To eliminate isotopic effects in the analysis, precise laboratory data for isotopic shifts of the relevant lines is desired [25]. Depending on the atomic structure, or more specifically the lifetime of the involved states, the measurement of atomic transition frequencies require different spectroscopic techniques. Furthermore, for many species the lack of an appropriate transition for laser cooling results in Doppler broadening and the shifts obscuring the measured spectra. This problem was overcome in the quantum logic spectroscopy (QLS) technique [26], where a so called logic ion with an appropriate cooling transition was used to cool and detect the state of the ion under investigation. But this technique is limited to transitions involving a long-lived upper state. Building on the principle of QLS, we investigated a novel spectroscopy technique that enables the precise measurement of transitions and isotopic shifts in a regime of intermediate and short upper state lifetimes, the photon recoil spectroscopy (PRS). In future experiments the technique may be applied for measurements of transitions of highly charged or molecular ions which show an increased sensitivity to variations of fundamental constants [27]. Furthermore, it can be used to measure absolute frequencies and isotope shifts of complex metal ions like titanium and iron with high precision, as these values are important for the analysis of the quasar absorption data [22].

Precise isotope shift measurements are also of interest in nuclear physics. Nuclear properties such as the relative change in the nuclear charge radius can be derived from optical isotope shift measurements [28, 29], which serve as an ideal tool to complement direct measurements from electron scattering and muonic x-ray experiments. The isotope shift arises from two effects. The first one is associated with the change of the mass of the nucleus resulting in a shift of the recoil energy for different isotopes. The second one is due to the modified charge distribution in the nucleus resulting from the different number of neutrons in the core. The precise measurement of isotope shifts enables the determination of the mass and field shift constants related to these effects using a King plot analysis [30]. A higher level of precision may even permit the detection of very small effects in the determination of the isotope shift. This may be contributions from higher order nuclear charge radii, relativistic, or quantum electrodynamics (QED) effects. In these investigations alkali-earth metal ions are of special importance, since they incorporate a rather simple electronic structure, consisting of an inert-gas like electron core and a single valence electron [31]. The complex calculations for these systems [32, 33] can then be compared to the precisely measured isotope shift. Here we present measurements of the isotope shift of Ca^+ with an unprecedented accuracy of below 100 kHz and improved the uncertainty of these values by up to two orders of magnitude. From the

data we extracted the field and mass shift constants. The latter is to our knowledge the most accurately determined mass shift constant of a complex system. Using these high accurate isotope shift measurements, different theoretical models may be validated as performed for other elements in references [6, 7, 34], but the complex structure of the calcium ions make these calculations challenging. Additionally, an improved value of the nuclear charge radius was determined using the measured isotope shift.

For the successful implementation of the spectroscopy technique presented within this thesis, new technologies had to be developed. One helpful tool in laser spectroscopy experiments are optical fibers. Using fibers, the light necessary to perform spectroscopy can be guided efficiently to the investigated object, but to be applicable to spectroscopic investigations the fibers need to transmit only the fundamental mode. Many transition frequencies that are spectroscopically investigated are located in the ultraviolet (UV) spectral region. UV radiation creates defects, so called color centers, in the glass that absorb the radiation, making these fibers useless for spectroscopic applications [35]. Recently, a new class of fibers emerged that are able to guide light in a hollow core, avoiding UV induced damage [36]. In the work presented here, we extended the applicability of fibers in spectroscopic experiments to the ultraviolet spectral region by demonstrating single mode guidance of UV radiation using hollow core photonic crystal fibers of the Kagomé type [37].

During the last century many techniques emerging from quantum information processing are used in metrological investigations, especially in precision spectroscopy [26, 38, 39]. All these experiments show that coherent control of atoms and ions by laser fields and the preparation of non-classical states can serve as an important toolbox to improve spectroscopic experiments. Another well established class of techniques are adiabatic techniques used for precise control of the atom's internal state. In this thesis we implemented and characterized stimulated Raman adiabatic passage (STIRAP) to improve the detection of our spectroscopic signal. This technique studied for trapped ions in [40], provides efficient and robust control of the internal state of the ions. Here we show that it can be used to efficiently transfer population between two electronic states independent of the motional state of the ion. Together with the implementation of the single mode UV fiber, the STIRAP technique enabled the high accuracy of the spectroscopy technique described in this thesis.

The thesis is structured as follows. After an introduction, the theoretical framework of the experiments discussed in this thesis is provided in Chapter 2. Here, ion trapping as well as the coupling of the trapped ion to light fields is described. Afterwards, the experimental setup is presented in Chapter 3. To be able to perform spectroscopy with high precision new technologies were implemented in the ex-

periment. Therefore, the next chapters describe these improvements. We first present the characterization of a new photonic crystal fiber in Chapter 4. This fiber was used to reduce intensity fluctuations at the position of the ion by stabilizing the beam position close to the ion. In Chapter 5 we discuss the [STIRAP](#) technique to manipulate the ions internal state independent of the ion's motion. Thus improving the control of the ions in the trap and enabling the isotope shift measurements presented in Chapter 6. From these measurements relative and absolute field and mass shift constants were extracted and the uncertainty of changes of the mean square nuclear charge radius determined. The thesis ends with a summary and an outlook in Chapter 7.

All experiments described in this thesis are performed on ions in a linear Paul trap [8]. In these traps the ions are confined by ponderomotive forces, which arise for a charged particle in a high frequency, inhomogeneous potential. If the charged particle enters the trap it will oscillate due to the time dependent potential. Averaging over one oscillation period leads to a non-zero electrical field gradient as long as the ion is not oscillating around the minimum of the trap potential. This leads to a ponderomotive force directing the ion to the center of the trap where it is then confined. These traps incorporated in ultra high vacuum systems provide the possibility to trap atomic systems isolated from the environment. Together with coherent control techniques to manipulate the atomic systems they became the basis for experiments in different fields of physics like quantum simulation [41], quantum computation [42] and precision spectroscopy in optical clocks [19]. The importance of these experiments were acknowledged by the Nobel Prize in 2012 awarded in part to Dave Wineland who pioneered the advance of coherent manipulation in trapped ion systems.

In the following, a short introduction to ion trapping is presented and the motion of the ions in the trap is derived in Section 2.1. If two ions are trapped in the trap the motion of the two ions is coupled as will be shown in Section 2.2. The common motion of the ions can be used to transfer spectroscopic information between the ions as shown in the spectroscopy technique described in Chapter 6. Different motional states that are relevant for the work in this thesis are discussed in Section 2.3. Afterwards, the interaction of the ion with laser light is introduced by first providing a theoretical model of a two level atom interacting with a light field. Due to the motion in the trap the energy spectrum of the ion consists of an electronic and a motional part. As will be shown in Section 2.4 for a two level atom, transitions between electronic levels can be excited where the motion of the ion is reduced, excited or unchanged. These transitions can be used to cool the ion to the ground state of motion, which is the initial state for many experiments in this thesis. Since we use a Raman beam configuration for the coherent manipulation, the two level model of the atom is extended to consider three relevant levels of the atom interacting with two light fields in Section 2.5. A short summary closes this chapter.

2.1 ION TRAPPING

In the following the principle of ion trapping is introduced and the equation of motion of the ions in the trap is derived. The discussion is based on the descriptions in reference [43], where the equations of motion are derived classically. A quantum mechanical derivation can for example be found in references [44, 45] and leads to equivalent results. The interested reader is referred to references [8, 45, 46, 47] for more information on ion trapping.

There is no solution of Laplace's equation that could lead to a three dimensional confinement of a charged particle with static electric fields (Theorem of Earnshaw). But time dependent oscillating potentials can be used to confine the motion of a charged particle in all three dimensions, as, for example, in the linear Paul trap [8]. A schematic of such a trap is shown in Figure 1. Considering the cylindrical symmetry, we define the direction perpendicular to the symmetry axis of the trap as the radial direction and the direction along the symmetry axis as the axial direction. For radial confinement a voltage oscillating at a radio frequency (RF) is applied to two opposing blade-shaped electrodes, whereas the other two are grounded. For confinement along the axial direction a DC voltage is applied to two additional electrodes, the so called endcaps.

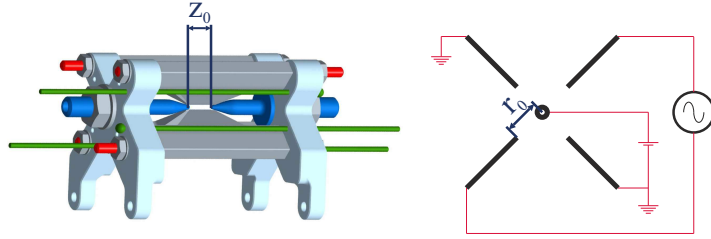


Figure 1: **Schematic of the ion trap.** A voltage oscillating at a radio frequency is applied between two opposing blades, whereas the other two blades are grounded. For axial confinement a DC voltage is applied to the two endcaps.

For a charged particle close to the symmetry axis of the ion trap, this configuration establishes an electric quadrupole potential along the radial direction which is given by [43]:

$$\phi_r(x, y, t) = \frac{V_0}{2} \left(1 + \frac{x^2 - y^2}{r_0^2} \right) \cos(\Omega_{rf}t), \quad (1)$$

where r_0 is the distance between two opposing blades, and Ω_{rf} and V_0 are the frequency and the peak voltage of the driving oscillating field applied to the blades. The potential in axial direction is given by:

$$\phi_a(z, t) = \frac{\kappa U_0}{z_0^2} \left(z^2 - \frac{1}{2}(x^2 + y^2) \right). \quad (2)$$

Here κ is a geometric factor and z_0 is the distance of the endcaps. The total potential generated by the trap is given by the sum of the radial (Equation (1)) and the axial potential (Equation (2)). The forces acting on a charged particle in the trap potential are given by the gradient of the potential and can be used to derive the equation of motion of a particle with mass m and charge q in the trap. According to Newton's second law of motion they read:

$$m \frac{d}{dt} \vec{r} = q \vec{E} = -q \nabla \phi(\vec{r}, t). \quad (3)$$

This equation can be rewritten in the form of the Mathieu equation:

$$\ddot{u}_i + [a_i + 2q_i \cos(\Omega_{rf}t)] \frac{\Omega_{rf}^2}{4} u_i = 0, \quad (4)$$

with u_i as the ion's position, the dots as the time derivative and the stability parameters a_i and q_i defined as:

$$a_x = a_y = -\frac{1}{2} a_z = \frac{4q\kappa U_0}{mz_0^2 \Omega_{rf}^2} \quad (5)$$

and

$$q_x = -q_y = \frac{2qV_0}{mr_0^2 \Omega_{rf}^2}, \quad q_z = 0. \quad (6)$$

The trap used to perform the experiments described in this thesis operates in the regime of small stability parameters $a, q \ll 1$, where the Mathieu equation has stable solutions. In first order in q they read:

$$u_i(t) \approx a_i \cos(\omega_i t + \phi_{si}) \left[1 + \frac{q_i}{2} \cos(\Omega_{rf}t) \right], \quad (7)$$

where ϕ_{si} is a phase related to the initial position and velocity of the particle and

$$\omega_i = \frac{\Omega_{rf}}{2} \left(a_i + \frac{1}{2} q_i^2 \right)^{1/2}. \quad (8)$$

The stable solution of Mathieu's equation (Equation (7)) shows that the motion consists of two parts, where the first is called the secular motion, which is equivalent to the motion of a particle in a static harmonic potential at frequency ω_i . The second part of Equation (7) is called micromotion and originates from the driving field. Its amplitude is suppressed by a factor of $q_i/2$ with respect to the secular motion and its oscillation frequency is equal to the drive frequency Ω_{rf} . Since $q_i \ll 1$ for the trap used to perform the experiments described in this thesis, this motion is neglected in the following.

The derivation of the equation of motion is assuming an ideal symmetric potential. If the ion is exposed to additional electrical fields that move the ion from its optimum position, an additional driven motion is induced. The amplitude of this so-called excess micromotion is strongly dependent on the position of the ion in the trap. Several

techniques are established to detect and minimize the undesired excess motion using electrodes providing electrical fields, which move the ion to the node of the potential [43]. The effect was characterized in reference [48] for our experimental setup and it was shown that the effect of the micromotion is negligible when the ion is placed at the position of lowest excess micromotion. This micromotion compensation was routinely carried out during our investigations. Thus, excess micromotion is neglected in the following description.

2.2 TWO ION CRYSTALS

For the spectroscopy technique described below we need to trap two ions simultaneously in the trap. Each ion experiences the repulsive potential due to the Coulomb interaction from the other ion in addition to the harmonic potential. The multi ion motion in a Paul trap which is important for many different experiments has been extensively studied in different laboratories. The interested reader is referred to references [49, 50, 51, 52, 53] for a detailed description. However, for the experiments described in this thesis only the motion of two ions along the trap axis is relevant. Hence we will focus on this motion in the following. Assuming that laser cooling has been applied, the two ions will localize at the two potential minima created by the superposition of the trap potential and the Coulomb repulsion given by:

$$V = \frac{1}{2}u_0x_1^2 + \frac{1}{2}u_0x_2^2 + \frac{1}{2} \frac{e^2/4\pi\epsilon_0}{|x_1 - x_2|} + \frac{1}{2} \frac{e^2/4\pi\epsilon_0}{|x_2 - x_1|} \quad (9)$$

Following the approach in reference [51] for small oscillations, the potential is approximated by its Taylor expansion. Then the system is transformed into the normal mode basis, where we calculate the frequencies of the normal modes:

$$\begin{aligned} \omega_{ip,z}^2 &= \frac{1 + \mu - \sqrt{1 - \mu + \mu^2}}{\mu} \omega_z^2, \\ \omega_{op,z}^2 &= \frac{1 + \mu + \sqrt{1 - \mu + \mu^2}}{\mu} \omega_z^2. \end{aligned} \quad (10)$$

In the equation we introduced the mass ratio $\mu = m_2/m_1$ and the oscillation frequency ν_z of a single ion with mass m_1 . The coupled motion of the ions along the axis is a superposition of two orthogonal modes, namely the in-phase (ip) mode and the out-of-phase mode (op). They can be considered as independent harmonic oscillators and can be addressed individually with laser pulses.

2.3 QUANTUM MECHANICAL STATES OF MOTION IN THE ION TRAP

In analogy to the classical description we can use the harmonic approximation in a quantum mechanical approach (see for example [44]), where the secular motion of the ion is approximated by the quantum mechanical harmonic oscillator model. Using this approach, we can define a basis of motional states according to the Fock state basis of the harmonic oscillator:

$$\begin{aligned}\hat{a}|n\rangle &= \sqrt{n}|n-1\rangle; \\ \hat{a}^\dagger|n\rangle &= \sqrt{n+1}|n+1\rangle; \\ \hat{n}|n\rangle &= n|n\rangle,\end{aligned}\tag{11}$$

where \hat{a} is the annihilation, \hat{a}^\dagger is the creation and \hat{n} is the number operator of a specific mode. In the trap, different motional states of the ion can be created [54]. The different motional states can be expanded in the Fock state basis according to:

$$|\psi\rangle = \sum_{i=0}^{\infty} p_n |n\rangle.\tag{12}$$

Here p_n denotes the probability of the ion to be in the specific Fock state. The most relevant states in the context of this thesis are the motional ground state, the thermal state and the coherent state of motion. The ground state is a pure quantum state in the Fock state basis and the lowest energy state of the harmonic oscillator. It can be written as:

$$|\psi\rangle = |0\rangle.\tag{13}$$

When the ion is in thermal equilibrium with an external reservoir of temperature T , the average occupation in the Fock state basis will follow the Boltzmann distribution:

$$p_n = p_n(T) = (1 - \exp(-\hbar\omega_z/k_B T)) \exp(-n\hbar\omega_z/k_B T),\tag{14}$$

with k_B as the Boltzmann constant. As shown in [55], a thermal state is created using the Doppler cooling technique [56, 57], where a laser beam with a lower frequency than the atomic resonance (red detuned) is used to extract energy out of the system utilizing the asymmetric energy balance during scattering in the presence of the Doppler effect. From energy considerations of the scattering process, a cooling limit can be derived as for example in [55, 58]. This is called the Doppler cooling temperature T_D :

$$T_D = \frac{\hbar\Gamma}{2k_B},\tag{15}$$

where Γ is the linewidth of the used transition and k_B is the Boltzmann constant. Since we describe two ions in a trap, the definition

of a temperature is inconvenient and it is more useful to express the probability with respect to the mean occupation number of Fock states. Then the state distribution can be written as:

$$p_n(\bar{n}) = \frac{\bar{n}^n}{(\bar{n} + 1)^{n+1}}, \quad (16)$$

As described below, we can use laser pulses to cool the ion from a thermal state to the motional ground state. From the ground state, which is also the lowest energy state in the coherent state basis, we can create any coherent state $|\alpha\rangle$ by application of the displacement operator onto the ground state:

$$\hat{D} = \exp(\alpha \hat{a}^\dagger + \alpha^* \hat{a}). \quad (17)$$

The coherent state can be expressed in the Fock state basis with the state distribution:

$$p_n(\bar{n}) = \bar{n}^n \exp(-\bar{n}) / n!, \quad (18)$$

where $\bar{n} = |\alpha|^2$ is the mean motional state occupation number. The displacement operator can be implemented in the experiment using several techniques. In Section 6.2 for example we coherently excite the motion of the two ion crystal by applying an oscillating electrical field between the endcaps of the ion trap [54, 59]. This can be described by the application of the displacement operator onto the motional state of the ion. In the spectroscopy technique described in Section 6.3, however, we implemented the coherent displacement using laser pulses, which are synchronized to the ion's motion in the trap. This efficiently depopulates the ground state of motion. As an illustration, the state distributions of a thermally distributed and a coherent state are plotted in the Fock state basis in Figure 2.

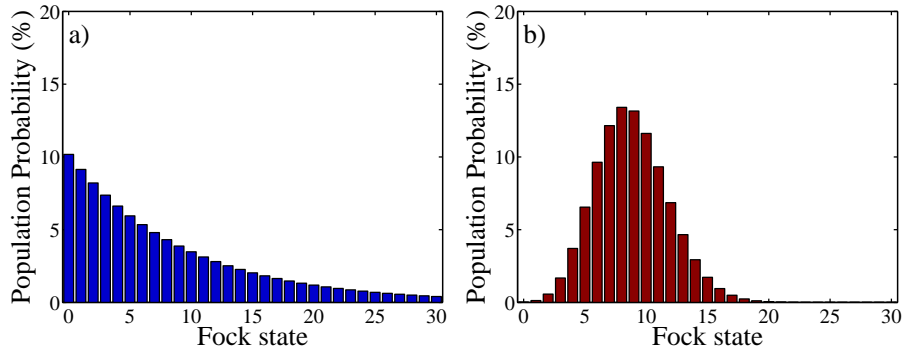


Figure 2: **Population of motional states in the ion trap.** In a) the thermal and in b) the coherent distribution is plotted for a mean motional state occupation number $\bar{n} \approx 9$, corresponding to the lowest reachable energy using Doppler cooling for a $^{25}\text{Mg}^+$ ion in our trap.

2.4 TRAPPED TWO LEVEL SYSTEM COUPLED TO A CLASSICAL LIGHT FIELD

In the experiments discussed in this thesis the trapped ions interact with laser light. In this section a theoretical description of the interaction of electromagnetic radiation with trapped ions is provided following the discussion in reference [46, 45]. Here we consider only two relevant electronic energy states of the ion in the harmonic pseudo potential of the trap.

For the derivation we assume that the atom can be considered as a positively charged core and a valence electron. Additionally, we make use of the dipole approximation, where we assume that the electrical field, with wavelength of hundreds of nanometers, does not vary over the spatial distribution of the atom, which is usually less than a nanometer. The Hamiltonian \mathcal{H} describing the system consists of three parts [46, 45, 60]:

$$\mathcal{H} = \mathcal{H}_a + \mathcal{H}_m + \mathcal{H}_i. \quad (19)$$

The first part is the atomic Hamiltonian, which can be expanded onto an orthonormal basis of atomic eigenstates. Considering only two relevant energy levels of the atom, defined as $|\downarrow\rangle$ and $|\uparrow\rangle$, the Hamiltonian is given by:

$$\mathcal{H}_a = \hbar (\omega_\downarrow |\downarrow\rangle \langle\downarrow| + \omega_\uparrow |\uparrow\rangle \langle\uparrow|). \quad (20)$$

where $\hbar\omega_\downarrow$ is the energy of the $|\downarrow\rangle$ state and $\hbar\omega_\uparrow$ is the energy of the $|\uparrow\rangle$ state. The Hamiltonian can be further simplified using the spin-1/2 algebra represented by the Pauli matrices and the identity operator, which are given by:

$$\begin{aligned} |\downarrow\rangle \langle\uparrow| + |\uparrow\rangle \langle\downarrow| &\rightarrow \hat{\sigma}_x; & -i(|\downarrow\rangle \langle\uparrow| - |\uparrow\rangle \langle\downarrow|) &\rightarrow \hat{\sigma}_y; \\ |\uparrow\rangle \langle\uparrow| - |\downarrow\rangle \langle\downarrow| &\rightarrow \hat{\sigma}_z; & |\downarrow\rangle \langle\downarrow| + |\uparrow\rangle \langle\uparrow| &\rightarrow \hat{I}; \\ |\uparrow\rangle \langle\downarrow| &\rightarrow \sigma_+; & |\downarrow\rangle \langle\uparrow| &\rightarrow \sigma_-. \end{aligned} \quad (21)$$

Using this representation and rescaling the energy by $\hbar(\omega_\uparrow + \omega_\downarrow)/2$ the atomic Hamiltonian reads:

$$\mathcal{H}_a = \hbar \frac{\omega_a}{2} \sigma_z, \quad (22)$$

with $\omega_a = \omega_\uparrow - \omega_\downarrow$, as the atomic transition frequency.

The second part of the Hamiltonian describing the system is the motional Hamiltonian. As discussed in the last section, the motion of the ion in the trap can be described approximately as that of a quantum mechanical harmonic oscillator:

$$\mathcal{H}_m = \hbar\omega_i \left(\hat{n}_i + \frac{1}{2} \right), \quad (23)$$

with $\hat{n}_i = \hat{a}_i^\dagger \hat{a}_i$ as the number operator, and \hat{a}_i^\dagger and \hat{a}_i as the harmonic oscillator creation and annihilation operators, respectively, as defined in the last section. The index i stands for different motional modes of the ions in the trap. In the following we limit the discussion to the center of mass motion along the trap axis z and omit the index i . Furthermore, we define the normal mode frequency of this mode as ω_z .

The third part of the Hamiltonian describes the coupling between the ion and the electrical field and is given by [45]:

$$\mathcal{H}_i = \frac{\hbar\Omega_0}{2} (\sigma_+ + \sigma_-) \left(e^{i(k\hat{z} - \omega_l t)} + e^{-i(k\hat{z} - \omega_l t)} \right) \quad (24)$$

where ω_l is the laser frequency and we have introduced the Rabi frequency, which, for dipole allowed transitions, is given by $\Omega_0 = \vec{\mu}_{\downarrow\uparrow} \vec{E}_0 / \hbar$. Here $\vec{\mu}_{\downarrow\uparrow}$ is the dipole matrix element of the transition from $|\downarrow\rangle$ to $|\uparrow\rangle$ and \vec{E}_0 the electrical field amplitude of the driving field. Here, we use a semi-classical model, in which the electrical field is considered classically. This is justified since we use sufficiently large laser powers, so that the light consists of many photons and quantum effects play a minor role. In the Hamiltonian we can identify the position operator \hat{z} , which, in the harmonic oscillator model, is given by [46]:

$$\hat{z} = \sqrt{\frac{\hbar}{2m\omega}} (\hat{a} + \hat{a}^\dagger) = z_0 (\hat{a} + \hat{a}^\dagger). \quad (25)$$

Additionally we introduce the Lamb-Dicke factor:

$$\eta = \vec{k} \hat{z}_0 = \frac{\hbar |k| \cos \theta}{\sqrt{2m\hbar\omega}}, \quad (26)$$

where θ describes the angle between the \vec{k} vector of the electromagnetic wave and the trap axis \hat{z} . The square of the Lamb-Dicke factor equals the ratio between the photon recoil energy and the energy splitting between the motional states. Now we transform the total Hamiltonian (Equation (19)) to a rotating frame by means of a unitary transformation:

$$\mathcal{H}'_i = \hat{U}^\dagger(t) \mathcal{H}_i \hat{U}(t). \quad (27)$$

For the transformation the Hamiltonian is split into two parts $\mathcal{H} = \mathcal{H}_0 + \mathcal{H}_i$ depending on the frame, in which we want to transform. The unitary operator \hat{U} is given by:

$$\hat{U}(t) = \exp\left(-\frac{i}{\hbar} \mathcal{H}_0 t\right). \quad (28)$$

We transform into a reference frame rotating at the laser frequency and the trap frequency and consequently define $\mathcal{H}_0 = \mathcal{H}_a + \mathcal{H}_m$ and

$\mathcal{H}_1 = \mathcal{H}_i$. After application of the rotating wave approximation and reordering the terms, the Hamiltonian in the rotating frame reads:

$$\mathcal{H}'_i = \frac{\hbar\Omega_0}{2}\sigma^+ \exp\left(i\left[\eta\left(\hat{a}e^{-i\omega_z t} + \hat{a}^\dagger e^{i\omega_z t}\right) - \Delta t\right]\right) + \text{h.c.} \quad (29)$$

where we defined $\Delta = \omega - \omega_0$ as the detuning of the laser field to the atomic transition. In the regime where the atomic wavefunction is much smaller than the wavelength $\lambda/2\pi$, which means that the ion is strongly localized in the trap center, we can expand the exponential function. The Hamiltonian in the so called Lamb-Dicke regime reads:

$$\mathcal{H}'_i = \frac{\hbar\Omega_0}{2}\sigma^+ \left(1 + i\eta\left(\hat{a}e^{-i\omega_z t} + \hat{a}^\dagger e^{i\omega_z t}\right)\right) e^{-i\Delta t} + \text{h.c.} \quad (30)$$

Here we can identify three resonances at $\Delta = -\omega_z, 0, \omega_z$. For the resonance at $\Delta = 0$ the Hamiltonian corresponds to so called carrier transition where only the electronic state of the atom is changed while the motional state stays the same. In the first order approximation the coupling strength for carrier transition corresponds to the Rabi frequency $\Omega_{n,n'} = \Omega_0$. The resonances at $\Delta = -\omega_z, \omega_z$ are called the red and blue sidebands, respectively. Starting from the electronic ground state, for the blue sideband the electronic state is changed and simultaneously one quantum of motion is added to the system, whereas for the red sideband the motion is reduced while changing the electronic state.

The repeated application of laser pulses tuned to the red sideband with a subsequent decay to the electronic ground state on a carrier transition can be used to cool the ion to its motional groundstate (sideband cooling). This state is the initial state of most of the experiments presented in this thesis.

Using the Hamiltonian in Equation (29), we can calculate the transition strength between different motional sub-states of the two atomic states by evaluating the matrix element:

$$\langle \uparrow, n' | \mathcal{H}'_i | \downarrow, n \rangle = e^{-i\Delta t} \frac{\hbar\Omega_0}{2} \langle n' | \exp\left(i\eta\left(\tilde{a} + \tilde{a}^\dagger\right)\right) | n \rangle, \quad (31)$$

with the rotating operators $\tilde{a} = \hat{a}e^{-i\omega_z t}$. Here we can extract the Rabi frequency of the trapped ion system:

$$\Omega_{n',n} = \Omega_0 \langle n' | \exp\left(i\eta\left(\tilde{a} + \tilde{a}^\dagger\right)\right) | n \rangle. \quad (32)$$

The Rabi frequency can be further evaluated and reads [46]:

$$\Omega_{n',n} = \Omega_0 \exp[-\eta^2/2] (n_<!/n_>!)^{1/2} \eta^{|n'-n|} \mathcal{L}_{n_<}^{|n'-n|}(\eta^2), \quad (33)$$

where $n_<$ and $n_>$ is the lesser and greater of n' and n , respectively. The \mathcal{L}_n^α are the generalized Laguerre polynomials given by:

$$\mathcal{L}_n^\alpha(X) = \sum_{m=0}^n (-1)^m \binom{n+\alpha}{n-m} \frac{X^m}{m!}. \quad (34)$$

According to Equation (33) we can calculate the coupling strength for carrier and sideband transitions in our setup, see Figure 3.

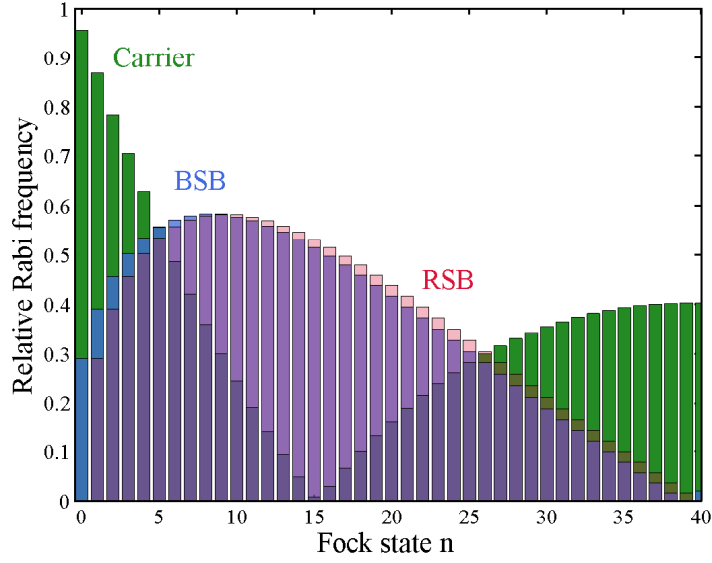


Figure 3: **Relative Rabi frequencies.** Relative Rabi frequencies of the transitions of different motional state of a single $^{25}\text{Mg}^+$ ion in the trap, with a Lamb-Dicke factor of 0.3, corresponding to a secular frequency of 2.22 MHz; green: carrier, blue: blue sideband, red: red sideband.

We can now investigate the dynamics of the system. Considering a resonant coupling between two states $|\downarrow, n\rangle$ and $|\uparrow, n'\rangle$, we consequently regard only these two states and the wavefunction of the atom can be written as:

$$\psi = c_{\downarrow, n} |\downarrow, n\rangle + c_{\uparrow, n'} |\uparrow, n'\rangle. \quad (35)$$

Inserting the wavefunction into Schrödinger's equation leads to:

$$\begin{aligned} \dot{c}_{\uparrow, n'} &= -i^{(1+|n'-n|)} e^{-i(\Delta t)} \Omega_{n', n} c_{\downarrow, n}; \\ \dot{c}_{\downarrow, n} &= -i^{(1-|n'-n|)} e^{-i(\Delta t)} \Omega_{n', n} c_{\uparrow, n'}. \end{aligned} \quad (36)$$

Solving Equation (36) using Laplace transformation we get for the resonant case where $\Delta = 0$:

$$\psi(t) = \begin{pmatrix} \cos(\Omega_{n', n} t) & -ie^{i\phi} \sin(\Omega_{n', n} t) \\ -ie^{-i\phi} \sin(\Omega_{n', n} t) & \cos(\Omega_{n', n} t) \end{pmatrix} \psi(0), \quad (37)$$

where the exponent is given by $\phi = (\frac{\pi}{2} |n' - n|)$. This equation shows so-called Rabi oscillations between different motional levels of the electronic transition. Therefore, by matching the laser pulse duration we can transfer the population between different states. For example

a pulse duration of $t = \pi/\Omega_{n',n}$ yields a complete population inversion and the laser pulse is called a π pulse. Instead of a dipole-allowed transition, in the experiment we have to drive transitions between long-lived metastable states using a Raman beam configuration, which is described in the next section.

2.5 THREE LEVEL SYSTEM COUPLED WITH TWO LIGHT FIELDS: RAMAN TRANSITIONS

In the experiment we use Raman transitions to couple two hyperfine states of an $^{25}\text{Mg}^+$ ion. The coupling is described by approximating the $^{25}\text{Mg}^+$ level scheme by the three level system with two laser couplings shown in Figure 4. The two laser beams are detuned to the excited level $|2\rangle$ but the frequency difference of the two laser beams is tuned to bridge the energy difference between the states $|1\rangle$ and $|3\rangle$. The laser coupling the state $|1\rangle$ with the state $|2\rangle$ is often called the pump beam and the one coupling the state $|3\rangle$ with the state $|2\rangle$ is called the Stokes beam. For clarity the additional energy splitting due to the trapping potential is neglected in the following. The Hamilto-

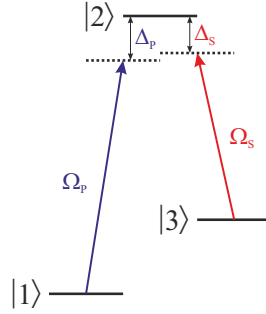


Figure 4: **Three level atom coupled to two light fields.** The so called Stokes laser couples the states $|3\rangle$ and $|2\rangle$ with a detuning Δ_s and Rabi frequency Ω_s whereas the Pump beam couples the states $|1\rangle$ and $|2\rangle$ with a detuning Δ_p and Rabi frequency Ω_p

nian of the system in the rotating wave approximation can be written as:

$$\mathcal{H} = \frac{\hbar}{2} \begin{pmatrix} 0 & \Omega_p & 0 \\ \Omega_p & 2\Delta_p & \Omega_s \\ 0 & \Omega_s & 2(\Delta_p - \Delta_s) \end{pmatrix} \quad (38)$$

Where the Ω_i are the Rabi frequencies and the Δ_i are the detunings of the pump and the Stokes lasers with respect to the one photon resonances. Neglecting the trap, the state vector can be written according to Equation (35):

$$\psi = c_1 |1\rangle + c_2 |2\rangle + c_3 |3\rangle. \quad (39)$$

Using Schrödinger's equation we can calculate the time evolution and get the coupled system of differential equations:

$$\begin{aligned} i\dot{c}_1 &= \frac{1}{2}\Omega_p c_2; \\ i\dot{c}_2 &= \frac{1}{2}\Omega_p c_1 + \Delta_p c_2 + \frac{1}{2}\Omega_s c_3; \\ i\dot{c}_3 &= \frac{1}{2}\Omega_s c_2 + (\Delta_p - \Delta_s) c_3. \end{aligned} \quad (40)$$

We are interested in the two photon resonance case, where $\Delta_p = \Delta_s = \Delta$ and the difference in the last equation is zero. Additionally we consider that the couplings Ω_i are small compared to the detunings Δ_i . Now we adiabatically eliminate state $|2\rangle$ using $\dot{c}_2 = 0$ [61, 62] and get:

$$\begin{aligned} i\dot{c}_1 &= -\frac{\Omega_p}{4\Delta} (\Omega_p c_1 + \Omega_s c_3); \\ i\dot{c}_3 &= -\frac{\Omega_s}{4\Delta} (\Omega_p c_1 + \Omega_s c_3). \end{aligned} \quad (41)$$

Here we can extract an effective Hamiltonian:

$$\mathcal{H}_{\text{eff}} = -\frac{1}{4\Delta} \begin{pmatrix} \Omega_p^2 & \Omega_p \Omega_s \\ \Omega_p \Omega_s & \Omega_s^2 \end{pmatrix} \quad (42)$$

This Hamiltonian is equivalent to the two level Hamiltonian in Equation (24) with the effective Rabi frequency:

$$\Omega_{\text{eff}} = \frac{\Omega_p \Omega_s}{2\Delta}. \quad (43)$$

We can compare this equation to the off-resonant scattering rate of the pump and the Stokes beam given by [58]:

$$\Gamma_{sc;p,s} = \frac{\Gamma}{2} \frac{\Omega_{p,s}^2/2}{\Delta^2 + \Omega_{p,s}^2/2 + \Gamma^2/4}, \quad (44)$$

with $\Gamma = 1/\tau$ and τ as the lifetime of the excited state $|3\rangle$. Here we see that for large detunings Δ the effective Rabi frequency scales with $1/\Delta$ and the off-resonant scattering with $1/\Delta^2$. Therefore a compromise has to be found where an acceptable Rabi frequency can be achieved for the used laser power while keeping the off-resonant scattering as small as possible. This will be further discussed for our setup in Section 3.3.1. Additionally to the effective Rabi frequency we identify in Equation (42) a shift of the energy levels with respect to each other by:

$$\delta = \frac{\Omega_p^2}{4\Delta} - \frac{\Omega_s^2}{4\Delta}. \quad (45)$$

This shift is the AC Stark shift due to the presence of the two light fields. In the experiment we scan the transitions frequencies and we coherently manipulate the ions using the transition frequency including the AC Stark shift.

2.6 SUMMARY

In this chapter the basic theoretical framework of the work presented in this thesis was provided. First ion trapping and the motion of an ion in the trap were described. Afterwards, two ion crystals and different states of motion in the ion trap have been discussed and an introduction of the atom light interaction is provided first in the two level atom model coupled with one light field. In the end of the chapter this model was extended to consider three energy levels of the atom coupled with two light fields by means of Raman transitions. The framework given in this chapter is extended at the beginning of each chapter to cover the more specific problems of the described content.

The experiments described in this thesis are based on coherent operations by means of laser pulses performed on a $^{25}\text{Mg}^+$ ion trapped in a linear Paul trap. These operations rely on the coherence between the optical carrier phase and the atomic phase. For the precision isotope shift measurements presented in Chapter 6, additional laser beams with frequencies near resonant to the $^2\text{S}_{1/2} \rightarrow ^2\text{P}_{1/2}$ and the $^2\text{D}_{3/2} \rightarrow ^2\text{P}_{1/2}$ transitions of the calcium isotopes are needed. Furthermore, the frequency of these lasers need to be counted. This is done by electronically stabilizing and comparing them to a frequency comb, referenced to the SI second in the German National Metrology Institute (PTB). Additional laser setups are used to photo-ionize the atoms from an atomic beam, thus providing the ions that are trapped in the electronic potential of the trap. The vacuum chamber and the linear Paul trap used in the experiments are described in detail in reference [48].

After a short description of the ion trap and its relevant parameters in Section 3.1, the laser systems needed for isotope-selective photoionization of the different ions are described. Afterwards, a short summary of the laser system for the coherent manipulation of $^{25}\text{Mg}^+$ is provided in Section 3.3. Furthermore, the orientation and polarization of all lasers with respect to the ions and the quantization axis is discussed. In Section 3.4 the laser systems used to excite and manipulate the Ca^+ spectroscopy ions and its frequency stabilization setup are introduced. In the last section of this chapter a simplified schematic of the complete spectroscopy setup is displayed.

3.1 THE ION TRAP

We use the ion trap shown schematically in Figure 1 and described in reference [48] for the experiments. An AC voltage oscillating at a frequency of 24.8 MHz is applied to a helical resonator for amplitude enhancement [48]. Here, typically an electrical power of 3–5 W is coupled into the resonator. Its output is then applied to two of the stainless steel blades, which together with the two grounded blades generate the potential, that confines the ions radially in the ion trap (see Figure 1). The axial confinement is provided by a DC voltage of up to 2 kV applied to the two endcaps. For our trap this leads to normal mode frequencies of 2.22 MHz in the axial and ≈ 5 MHz in the radial direction for a single $^{25}\text{Mg}^+$ ion. An additional differen-

tial voltage of up to 150 V between the two endcaps and additional stray field compensation electrodes, between which a voltage of up to 500 V can be applied, are used to move the ion to the point of lowest micromotion in the trap (see Section 2.1).

3.2 IONIZATION LASER SYSTEMS

For the isotope shift measurements two ion crystals, consisting of a $^{25}\text{Mg}^+$ logic ion and different Ca^+ spectroscopy isotopes, are loaded into the trap. This is done via two-step photoionizing an atomic beam from a resistively heated steel tube filled with a powder of the corresponding material. For the photoionization of the ^{25}Mg atoms, the frequency quadrupled output of an extended cavity diode laser (ECDL) with a wavelength of 285 nm after quadrupling is used. The laser first excites the atoms from the $^1\text{S}_0$ to the $^1\text{P}_1$ excited state and in a second step the same laser ionizes the atoms. Additionally, a laser beam at a wavelength of 280 nm used for Doppler cooling is applied simultaneously, to enhance the ionization rate and cool the generated ions.

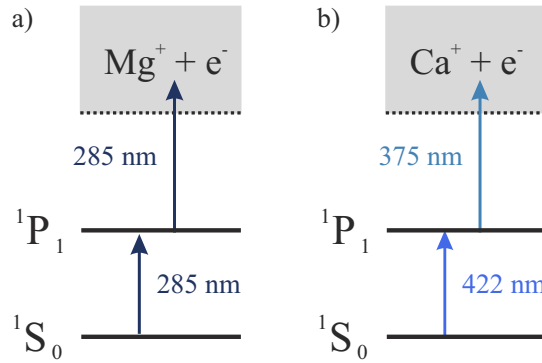


Figure 5: **Energy scheme and laser wavelength for photo-ionizing the neutral atoms.** a) Mg (wavelength taken from [63]) and b) Ca (wavelength taken from [64]). Isotopic shifts of neutral calcium and a detailed description of the isotope selective loading are given in Section 6.2. Energy levels not to scale.

The different Ca^+ isotopes are excited to the $^1\text{P}_1$ state using a frequency doubled ECDL with a frequency of 423 nm after doubling. By tuning the laser frequency resonant to the isotope specific transition frequencies [64], isotope selective loading can be achieved by adjusting the loading parameters as described in Section 6.2. Ionization of the excited calcium atoms is accomplished using the output of a laser diode with a wavelength of 375 nm. Both laser beams are guided through single mode optical fibers providing a Gaussian beam profile before entering the vacuum chamber along the trap axis.

3.3 EXPERIMENTAL SETUP FOR COHERENT MANIPULATION OF MAGNESIUM

For cooling and coherent manipulation on the $^{25}\text{Mg}^+$ ion we use the setup described in [65]. The frequency quadrupled output of an Ytterbium doped fiber laser¹ in addition with an electro-optical modulator² (EOM) generates the laser beams for Doppler cooling (see Section 2.3), Raman sideband cooling (see Section 2.4) and for the coherent manipulation. The plus first order sideband of the EOM, operated at a modulation frequency of $2\pi \cdot 9.2$ GHz, is in resonance with the $^2\text{S}_{1/2}(F = 3, m_F = 3) \rightarrow ^2\text{P}_{3/2}(F = 4, m_F = 4)$ transition for Doppler cooling and state discrimination, as explained in the next section (Section 3.3.1). Here, F denotes the total angular momentum and m_F its projection along the magnetic field direction. The optical carrier is used, with an additional acousto-optical modulator (AOM) setup, to create the Raman laser beams that couple the hyperfine states $|\uparrow\rangle = ^2\text{S}_{1/2}(F = 3, m_F = 3)$ and $|\downarrow\rangle = ^2\text{S}_{1/2}(F = 2, m_F = 2)$, forming the selected qubit. The level scheme of $^{25}\text{Mg}^+$ with the described couplings is displayed in Figure 6.

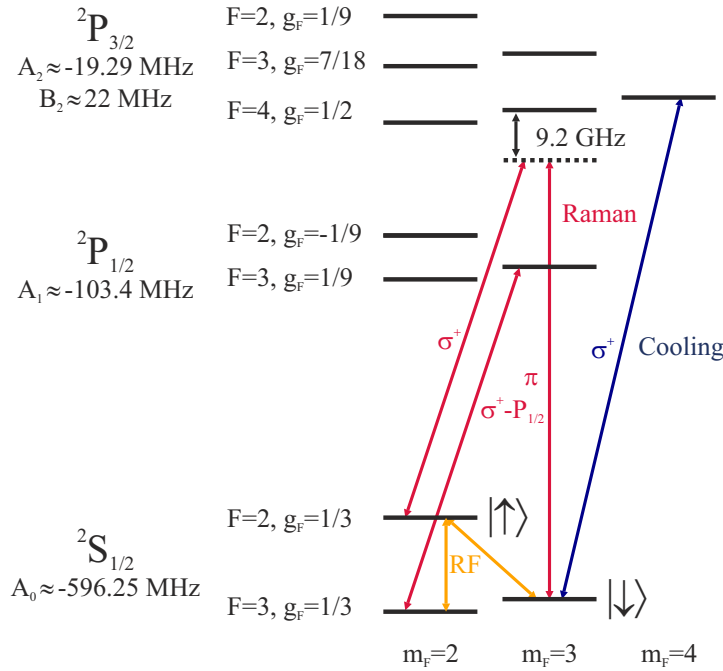


Figure 6: **Relevant level scheme of the $^{25}\text{Mg}^+$ ion and the lasers for coherent manipulation.** The different electronic states are split by the hyperfine splitting and the degeneracy of the magnetic substates is lifted by an external magnetic field. Energy levels not to scale.

¹ Koheras Boostik

² Laser 2000 GmbH NFO-4851-M

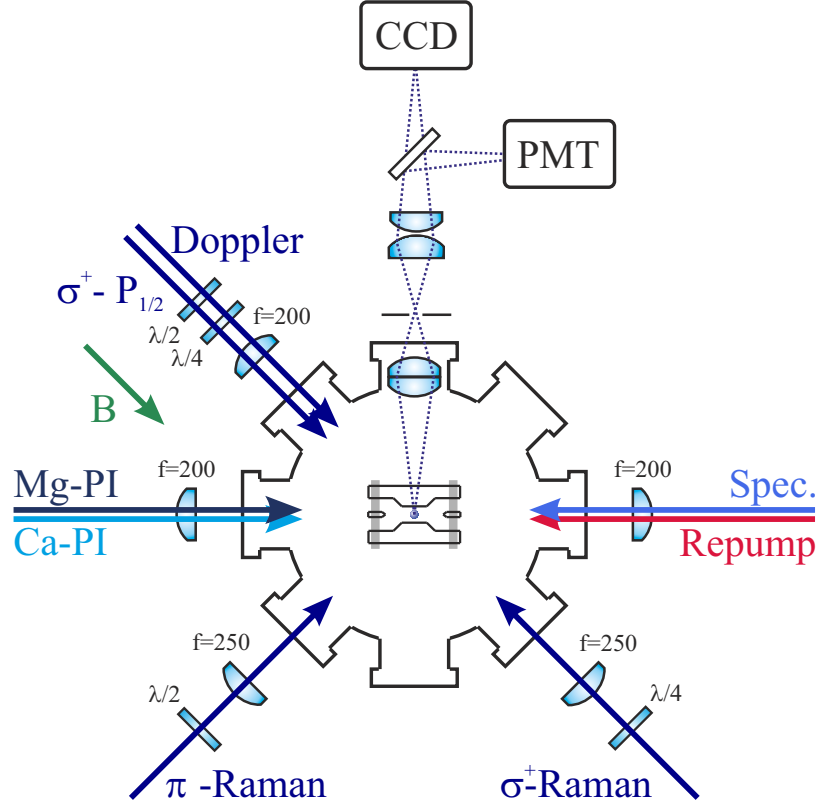


Figure 7: **Vacuum chamber with beam alignment.** The Doppler cooling beam is aligned along the magnetic field direction. The two Raman laser beams span a 90° angle with each other, such that their relative \vec{k} -vector is aligned along the trap axis. The photo-ionization laser as well as the two lasers used to excite the calcium ions are aligned along the axis of the ion trap.

Additionally, a second frequency quadrupled fiber laser supplying the σ^+ repump beam is used to couple the $S_{1/2}(F = 2, m_F = 2)$ with the $P_{1/2}(F = 3, m_F = 3)$ state for efficient ground state cooling as described in [66, 67].

The Doppler cooling laser beam axis is aligned parallel to an externally generated magnetic field. It spans an angle of 45° with the trap axis to provide cooling of the ion's motion in all three directions defined by the trap. Here we used circular σ^+ polarization to make use of the cycling transition of the $^{25}\text{Mg}^+$ ion ($^2S_{1/2}(F = 3, m_F = 3) \rightarrow ^2P_{3/2}(F = 4, m_F = 4)$), where the upper $^2P_{3/2}(F = 4, m_F = 4)$ state can only decay into the $^2S_{1/2}(F = 3, m_F = 3)$ state (see Figure 6). The Raman beams are aligned in the plane spanned by the magnetic field vector \vec{B} and the trap axis. One is counter propagating to the Doppler cooling beam and has a circular polarization (σ^+ polarization), while the other one is aligned perpendicular to it and is linearly polarized (π polarization). This, combined with a relative \vec{k} -vector along the trap axis, enabling coherent manipulation of the motional modes along that direction, provides the desired couplings

as depicted in the level scheme (Figure 6). To illustrate the laser configuration, a sketch of the vacuum chamber with the ion trap and the lasers used in the experiments is shown in Figure 7.

Additionally, to the laser couplings an electromagnetic wave oscillating at a radio frequency (RF) of ≈ 1.789 GHz can be applied to couple the qubit states utilizing a directional antenna outside the vacuum chamber (see Figure 6). The signals oscillating at radio frequencies driving the AOMs are generated and controlled via a pulse sequencer based on a field programmable gate array [68]. This is controlled using the experimental control computer via an open source python server. It provides eight phase coherent radio frequency signals created by direct digital synthesizer (DDS) boards which are controlled via on board voltage controlled gain amplifiers (VGA). Additionally, several transistor transistor logic (TTL) outputs can be controlled with the sequencer board.

3.3.1 Measurement principle and coherence of Raman beams

To determine the quantum mechanical state of a single ion we do a projective measurement using the electron shelving technique [69]. Here the two different qubit states of the ions are distinguished by resonantly coupling one of the states, in our case the $|\downarrow\rangle$, to an auxiliary state $|\text{aux}\rangle$ with a short lifetime (of the order of nanoseconds). If the ion is in this state (the so called bright state) it scatters on the order of millions of photons per second, whereas if it is in the $|\uparrow\rangle$ state (the dark state) the laser is not resonant and not many photons are scattered. We collect a fraction of these photons and detect them with a photo-multiplier tube. In this way we can distinguish the two states by counting the number of detected photons.

If, however, the ion is prepared in a superposition state $|\psi\rangle = c_{\downarrow} |\downarrow\rangle + c_{\uparrow} |\uparrow\rangle$ and we apply the laser coupling, in the measurement process the ion is projected either onto $|\downarrow\rangle$ or $|\uparrow\rangle$. To be able to determine the state amplitude we have to repeat the measurement and average the results. Due to the probabilistic nature of the measurement process and the limited number of measurements, we determine the state amplitude with an uncertainty, which is called quantum projection noise (QPN) and is given by [70]:

$$\text{QPN} = \sqrt{p_{\uparrow} \cdot (1 - p_{\uparrow}) / N} \quad (46)$$

where p_{\uparrow} represents the probability to be in the $|\uparrow\rangle$ state and is given by $p_{\uparrow} = |c_{\uparrow}|^2$. For measurements on a single ion, N is the number of measurements. This limit can be reached using the electron shelving technique, as described in [69] and is the fundamental limit in the spectroscopy technique described in Chapter 6.

If we prepare the $^{25}\text{Mg}^+$ ion in the $|\uparrow\rangle$ state and couple the $|\downarrow\rangle$ with

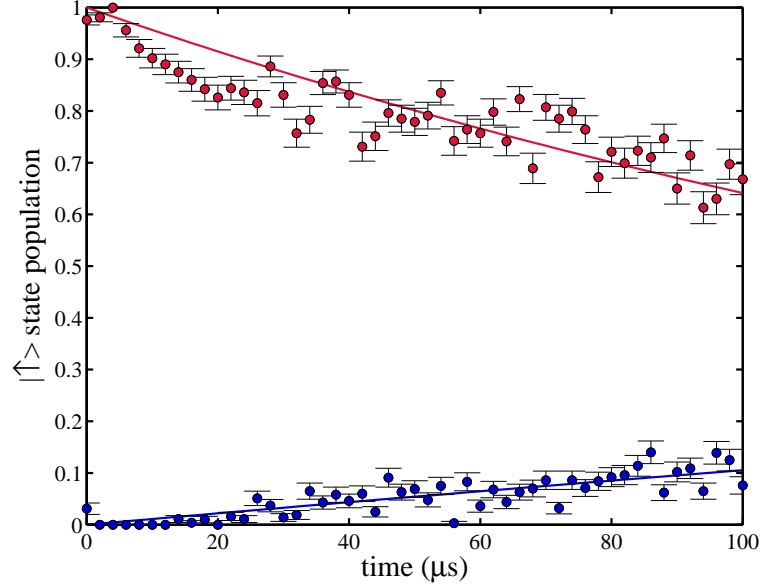


Figure 8: **Off-resonant excitation** Measured state depopulation from off-resonant Raman scattering for the ion initialized in the $|\uparrow\rangle$ (red) and the $|\downarrow\rangle$ state (blue). The fitted exponential decay yields the decay rates of $\gamma_{|\downarrow\rangle} = 1.1 \pm 0.1 \text{ ms}^{-1}$ and $\gamma_{|\uparrow\rangle} = 4.4 \pm 0.4 \text{ ms}^{-1}$ for the two states.

the $|\text{aux}\rangle = {}^2P_{3/2}(F = 4, m_F = 4)$ state, the laser frequency is detuned by 1.789 GHz to the $|\uparrow\rangle$ state. This leads to off-resonant depumping from the $|\uparrow\rangle$ to the $|\downarrow\rangle$ state as shown in [48]. Therefore, the detection time is limited, leading to an overlap of the detected photon distributions for the ion initialized in the bright and the dark state for a mean detected bright state photon number of about 3 photons for a detection time of 8 μs . This results in a detection error, since the histogram of the detected photons for the bright state has significant population at 0, resulting in false state discrimination using the threshold technique. In this technique the two qubit states are distinguished by setting a threshold and assign the ions state depending on whether more photons (assigned to $|\uparrow\rangle$ state) or less photons (assigned to $|\downarrow\rangle$ state) than this threshold are detected. To reduce the detection error we use the π detection technique, characterized in [71], where two detection pulses are applied with an intermediate radio frequency π -pulse, which inverts the two states. Keeping only anti-correlated detection events, errors are detected and discarded. This way the detection efficiency is improved to higher than 97 % and made more robust.

Besides the detection, the state preparation is important in the experiment. As described above, we use a Raman beam configuration to coherently manipulate the states of the ion. Here, the limited detuning leads to off-resonant scattering, that reduces the fidelity of all coherent manipulation operations. We investigated the influence of

the off-resonant excitation by initially preparing the ion in one of the two qubit states and successive application of the Raman laser beams. The frequency of the lasers is detuned to the two-photon resonance by half the distance to the next resonance (1.1 MHz). This way we preclude coherent couplings between the two states, thus revealing the effect of off-resonant excitation. Depopulation of the initial state as a function of the applied Raman laser time is displayed in Figure 8. Here we see that, due to off-resonant excitation, the dark state ($|\uparrow\rangle$) is depumped to the bright state and vice versa. An exponential fit to the experimental data yields a decay rate of $\gamma_{|\downarrow\rangle} = 1.1 \pm 0.1 \text{ ms}^{-1}$ and $\gamma_{|\uparrow\rangle} = 4.4 \pm 0.4 \text{ ms}^{-1}$ for the two states. The smaller decay rate for the $|\downarrow\rangle$ state can be explained considering the off-resonant couplings between the involved states. Taking the atomic level structure and the different coupling strength of the levels given by the Clebsch-Gordan coefficients (given for $^{25}\text{Mg}^+$ in [48]) into account, the number of off-resonant scattering events, where the internal state of the ion changes, is on the order of 4 times smaller for the $|\downarrow\rangle$ as for the $|\uparrow\rangle$. Additionally, for the $|\uparrow\rangle$ state, the detuning of the lasers to the excited $^2\text{P}_{3/2}$ state is smaller and leads to an increased off-resonant scattering rate. As described in Section 2.5, a larger detuning would reduce this effect, but to keep the same effective Rabi frequency, the laser power needs to be increased, which would require a new high power Raman laser system.

3.4 THE CALCIUM SPECTROSCOPY LASER SYSTEM

The lasers used to excite the calcium transitions are ECDLs electronically frequency stabilized to a frequency comb. The lasers are located in another laboratory and their output signals are transmitted via single mode fiber into the laboratory, where the experiments are performed. The AOM setup to control and scan the laser was build up on the experimental table and is controlled via the pulse sequencer described above. The level structure of the Ca^+ spectroscopy ion together with the laser couplings is depicted in Figure 9.

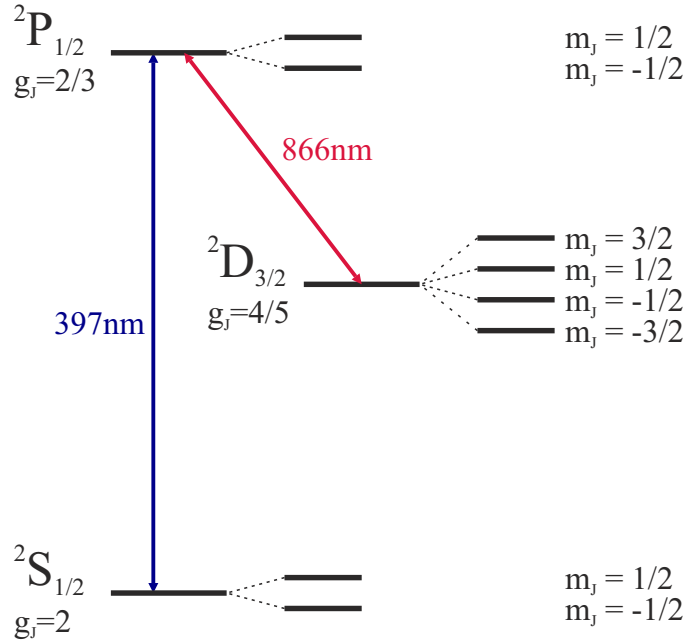


Figure 9: **Calcium level scheme.** Relevant level scheme of the even Ca^+ isotopes with the laser couplings. The degeneracy of the magnetic substates of the electronic levels is lifted by the external magnetic field.

The spectroscopy light at a wavelength of 397 nm is created by a frequency doubled [ECDL](#)³. A few mW of light of its fundamental signal at 794 nm is used to stabilize its frequency with respect to the second harmonic output signal of a fiber optical frequency comb⁴, using a phase/frequency comparator. The two characteristic frequencies of the comb, determining the absolute frequency of its teeth, namely the carrier-envelope-offset frequency and the repetition rate, are stabilized to the 10 MHz reference signal obtained from a hydrogen maser, which is referenced to the SI second in [PTB](#). The second laser used to manipulate the calcium ions is an [ECDL](#)⁵ providing light with a wavelength of ≈ 866 nm. Here, a few mW of light are coupled out and used to frequency stabilize the laser to a second amplified and frequency doubled output signal of the same frequency comb. For both lasers a similar electronic setup is used to provide the error signal for frequency stabilization. After overlapping the laser beams with the comb light, the measured beat signal is mixed with a referenced [DDS](#) board. To compensate slow frequency drifts on timescales of seconds, the filtered difference frequency $f_{\text{ref}} - f_{\text{beat}}$ is compared to the 10 MHz reference signal using a phase/frequency comparator. This comparator produces the error signal which is fed back via a piezo actuator to the grating of the laser for frequency correction. The electronic setup for the frequency stabilization is depicted in [Figure 10](#).

³ Toptica DL SHG

⁴ Menlo systems FC1500

⁵ Toptica DL Pro

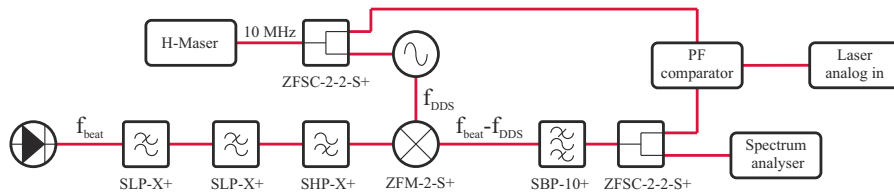


Figure 10: **Electronic circuit for the frequency stabilization of the spectroscopy lasers.** The beat signal of the spectroscopy lasers is recorded with a photodiode. The consecutive low (SLP-X+) and high (SHP-X+) pass filters are chosen in a way that they build a bandpass filter around the desired beat frequency. After filtering, the signal is mixed with the output frequency of a referenced DDS board so that the difference frequency is around 10 MHz. After a second filtering stage, this frequency is compared to the 10 MHz reference and the error signal of the comparator is fed back to the grating of the [ECDL](#).

As described above, the stabilized laser light of the two lasers used to excite the calcium ions are transmitted to the experimental laboratory via single mode optical fibers. After the fiber an [AOM](#)⁶ in double-pass configuration is used to shift the frequency of the laser resonant with the $^2S_{1/2} \rightarrow ^2P_{1/2}$ transition. Scanning the [AOM](#) drive frequency leads to detuning-dependent distortions of the beam profile (see Section 4.3), which are transformed into intensity fluctuations by coupling the diffracted light into a single mode optical fiber. To eliminate these residual intensity fluctuations, the output power of the laser light is electronically stabilized after the fiber using a proportional-integral control loop. After stabilization, a subsequent [AOM](#)⁷ is used to create the short laser pulses and a second single mode optical fiber⁸ is used for spatial filtering, i.e. to provide a Gaussian beam shape of the spectroscopy light. The beam is then overlapped with the beam from a second laser resonant with the $^2D_{3/2} \rightarrow ^2P_{1/2}$ transition in Ca^+ . This beam at a wavelength of 866 nm passes a double-pass [AOM](#) (for frequency scanning) and a subsequent fiber (for spatial filtering). Since the desired pulse length for the application of this laser is much longer than the one for the laser at 397 nm, the same [AOM](#) is used for switching and scanning the frequency of this laser beam. A schematic of the setup is shown in Figure 11.

6 Brimrose Corp. TEF-200-50-397

7 IntraAction Corp. ASM-2202B8

8 Oz optics QPMJ-3A3A-400-3/125-3-5-1

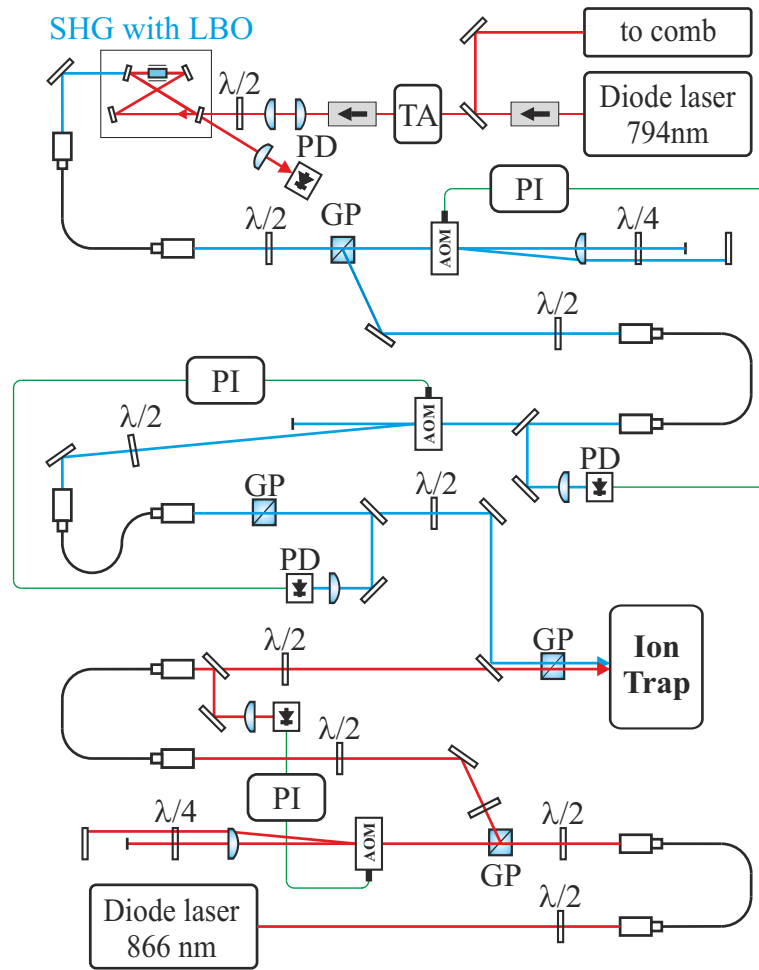


Figure 11: **Optical setup for the manipulation of the spectroscopy lasers.** Abbreviations: $\lambda/2$: half waveplate; PD: Photodiode; GP: Glan Polarizer; PID: Proportional Integral Controller Loop; TA, Tapered Amplifier. After frequency doubling the laser light at 397 nm passes through an AOM in double pass configuration for frequency scanning. After a single mode optical fiber the light passes through a second AOM for switching and a second fiber. The light of the second laser at 866 nm passes one AOM in double pass configuration which is at the same time used to switch the light.

After overlapping, the two laser beams are guided into the vacuum chamber along the trap axis (see Figure 7). A Glan laser polarizer in front of the vacuum chamber provides linear polarization of both laser beams. The polarization is aligned in the horizontal plane spanning an angle of 45° with an external magnetic field of approximately 5.8 G. As described above, this field lifts the degeneracy of the Zeeman sublevels, and with the linear polarization of the spectroscopy lasers we drive all π transitions as well as equal amounts of σ^+ and σ^- transitions. We thus expect a symmetric excitation profile of the relevant transition.

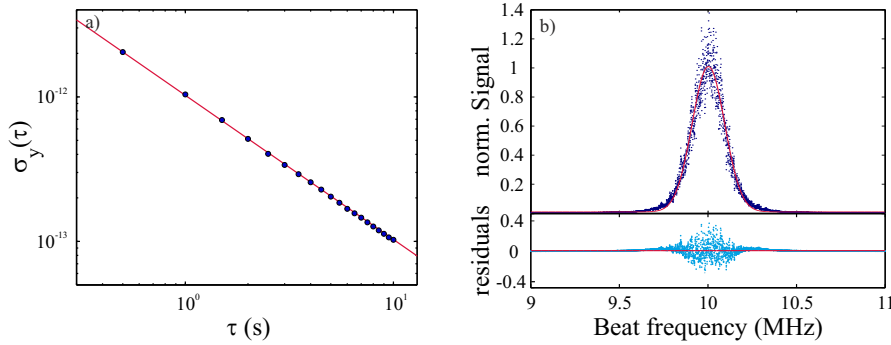


Figure 12: **Stability of the spectroscopy laser** a) Overlapped Allan deviation of the spectroscopy laser. b) Measured line profile and residuals of the measured data from the fitted Gaussian function. No asymmetry of the line profile could be detected within the measurement uncertainty.

3.5 LASER INSTABILITY

For the spectroscopy we use [ECDLs](#) which provide linewidth on the order of 100 kHz for integration times of 5 μ s. This linewidth is much smaller than the frequency resolution of our measurement on this timescale. Frequency drifts on timescales larger than a few milliseconds are compensated by minimizing the frequency deviations of the laser from a chosen tooth of the frequency comb, as described above. This is done using the piezo actuator that controls the frequency of the laser via a grating in the laser cavity. Additionally, we examined the symmetry properties of the line shape of the lasers, since asymmetries would cause an undetected systematic shift in the frequency measurement. Therefore, we measured the beat frequency of the comb with an ultra-stable laser provided by a neighboring laboratory (reference laser 1 in [72]) to be able to detect asymmetries of the individual comb tooth. In a similar experiment we measured the beat of the spectroscopy lasers with the comb (shown in Figure 12). The slope of a linear fit to the residuals was $> 4 \cdot 10^{-4} \text{ MHz}^{-1}$, whereas the measured point to point fluctuation of the signal was on the order of 10^{-3} . In conclusion, no asymmetry was detected within the measurement uncertainties.

Additionally to the symmetry properties of the laser line shape, we investigated the in-loop frequency stability of the 866 nm laser by counting the beat frequency with an electronic counter referenced to the maser frequency. The overlapped Allan deviation [73] of the beat signal is displayed in Figure 12. This two sample variance is a tool used to investigate the statistical properties of a measured data set and can be used to identify noise processes in the measurement. Here we see that for increasing measurement time the deviation reduces with $1/\tau$, which indicates that the dominant noise source is flicker phase noise in the measured time regime (see for example

[74]). For averaging times longer than 1 s, the relative frequency uncertainty (as measured with respect to the frequency comb) is lower than 10^{-12} . This is on the same order as the maser frequency uncertainty on this timescale. Such frequency fluctuations are negligible for our measurements, where frequency deviations on the order of a few kilohertz are tolerable. A similar analysis of the stability of the spectroscopy laser providing light with a wavelength of 397 nm leads to an uncertainty on the same order of magnitude.

3.6 COMPLETE SETUP

Now we can put all parts used in the experiment together and show a simplified schematic of the complete setup, displayed in Figure 13. To give an impression of the size of the experiment the dimensions of the parts of the setup located in the laboratories are shown. From these dimensions it can be seen, that a large free space AOM setup is used to control the laser beams for the coherent manipulation of the $^{25}\text{Mg}^+$ logic ion. Beam pointing fluctuations cause errors in the coherent manipulation and limit the fidelity of our operations. How we reduced this errors using hollow core photonic crystal fibers (PCF) is discussed in the next chapter.

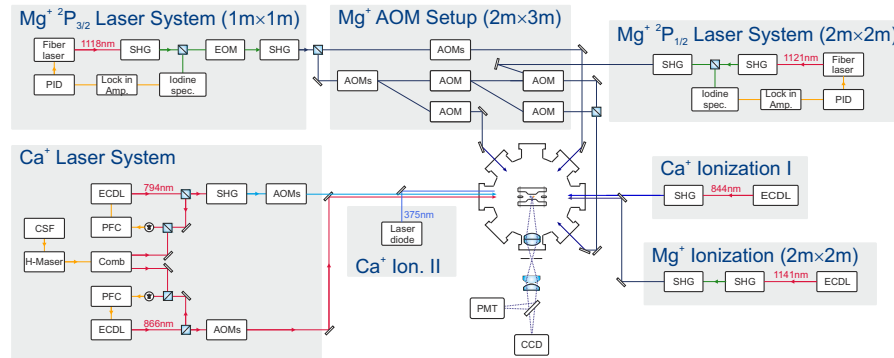


Figure 13: **Complete laser setup needed for PRS.** The complete laser setup used to perform photon recoil spectroscopy (PRS) on different calcium isotopes is shown. For the Magnesium laser systems, which are located in the laboratory where the experiments are performed, the dimensions of the different parts of the setup are shown. Abbreviations: SHG: second harmonic generation cavity; CSF cesium fountain clock; PFC; phase/frequency comparator; comb: frequency comb; Lock in amp.: Lock in amplifier

In the precision spectroscopy experiment described in Chapter 6 the trapped ions are controlled using coherent operations utilizing laser pulses. As shown in [75], one of the dominant errors in coherent manipulation of hyperfine qubit states is the relative intensity noise (RIN) at the position of the ion. If the frequency of the atomic transition is located in the ultraviolet spectral region, the laser beams used to control the ions are normally transmitted via long free space beam paths before they interact with the ion. Here, mirror vibrations and air turbulences lead to large beam pointing fluctuations. The resulting intensity fluctuations at the position of the ion lead to Rabi frequency fluctuations, which are translated into variations of the prepared atomic state between consecutive experiments using a laser pulse with a fixed duration. Assuming the Rabi frequency fluctuations to be Gaussian distributed, we can model the detected mean atomic state for different interaction times, as shown in Figure 14.

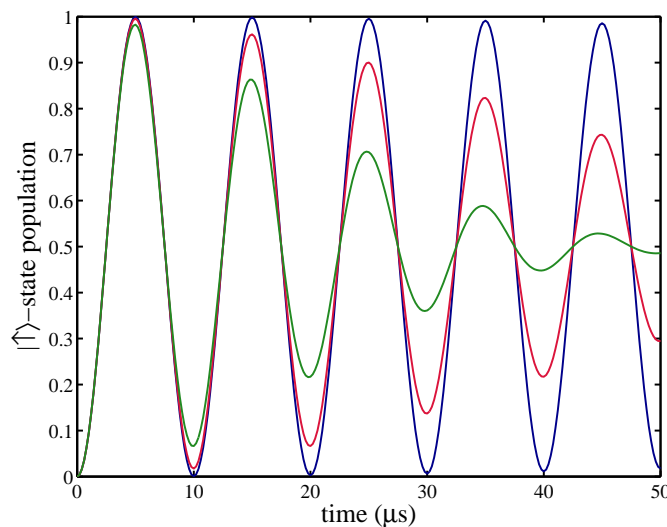


Figure 14: **Simulated Rabi oscillations.** Simulated Rabi oscillation for Gaussian distributed intensity fluctuations. The full width at half maximum of the Gaussian distribution is 1 % (blue), 5 % (red) and 10 % (green) of the mean Rabi frequency.

Here we see that the intensity noise lead to a reduced contrast if the fluctuations in Rabi frequency are on the order of a few percent. Therefore, a high stability of the laser intensity at the position of the ion is desired for experiments using coherent manipulation. There are different ways to achieve a stable beam position. For example, one could avoid air currents using tubing that surround the beam

path. In our setup a complete sealing would prevent optical access needed to align the acousto optical modulators. Other approaches are based on spatial filtering using pinholes or active beam path stabilization schemes. In applications using visible or infrared IR radiation, single mode optical fibers are most commonly used to remove beam pointing errors. However, up until recently, such fibers were not available for the UV. In this spectral region glass undergoes the effect of solarization, where defects called color centers form and hinder the transmission of UV radiation. This can be overcome using photonic crystal fibers (PCF) of the Kagomé type, where the light is transmitted in the hollow core of the fiber. We had the opportunity to test new fibers produced by the group of Philip Russell at the Max Planck Institute for the Science of Light in Erlangen, promising promising a good beam quality and pointing stability by single-mode guidance of UV radiation. In view of the higher fidelity of coherent manipulations with stable single-mode fiber beam delivery, a trade-off in laser power is acceptable, in particular, since high power laser systems are readily available [65].

Here we report on the characterization of a series of Kagomé-PCFs with different core diameters $D \approx 20 \mu\text{m}$ and different core wall thickness. After introducing the guiding mechanisms of different kinds of photonic crystal fibers in Section 4.1, the optical properties of the investigated fibers are presented in Section 4.2. Finally, we show that use of Kagomé-PCF in our trapped ion experiment increases the coherence time of the internal state transfer due to a reduction in beam-pointing instabilities in Section 4.3.

Parts of the following results were published by the author and his co-authors in [76].

4.1 GUIDING MECHANISMS IN PHOTONIC CRYSTAL FIBERS

In conventional fibers the guiding mechanisms that confines the light in the fibre core is well understood and can be explained by total internal reflection at the interface of two materials with different refractive index, the cladding and the core. The number of guided modes in the core is determined by the dimensionless V parameter defined as [77, 78]:

$$V = \frac{2\pi\rho}{\lambda} (n_{co}^2 - n_{cl}^2), \quad (47)$$

where ρ is the core radius and n_{co} and n_{cl} are the core and cladding refractive indices. From this parameter, the number of guided modes of the fiber can be calculated. For V numbers smaller than 2.405 a single degenerate pair of modes is guided by the fiber and it is said to be single mode [77, 78]. Although according to Equation (47), single-mode guidance can be maintained (for the same core-cladding index

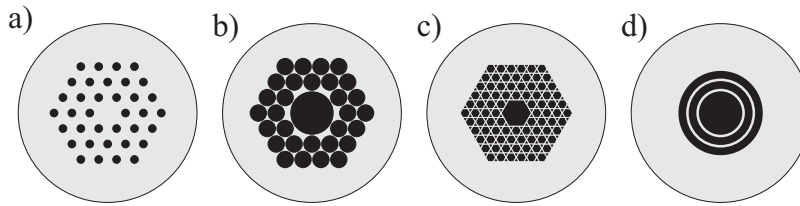


Figure 15: **Sketches of different photonic crystal structures.** The black regions are hollow and the gray regions are glass. a) Solid core PCF. b) triangular-lattice Photonic bandgap fiber. c) Kagomé fiber. d) Bragg fiber.

step) by reducing the core diameter by the ratio of the wavelengths, the optical power density in the core increases and the transmission degrades over time due to UV-induced color center formation and optical damage in the core [35].

A different class of fibers that have the potential to overcome these problems are photonic crystal fibers first demonstrated in 1997 [79]. These fibers consist of a periodic transverse microstructure surrounding and confining the light in the core.

For photonic crystal fibers depending on the periodic structure three distinct guiding mechanisms were identified [80, 81]. The first mechanism is a modified form of total internal reflection [79], for PCFs where the core index is larger than the average index in the cladding (Figure 15 a)). An effective V number can be derived and by adjusting the fiber parameters, like hole size d and pitch Λ (center-center spacing of the holes), single mode guidance can be achieved over a large transmission band. These fibers have the intriguing property that for $d/\Lambda < 0.42$ they only support the fundamental mode and are therefore called endlessly single mode. These fibers can be designed to have a large mode field diameter which reduces the optical power density in the glass, but since they possess a solid core, they still suffer from UV induced damage. For example, Yamamoto et al. found that in a PCF with a solid silica core the transmission dropped by more than 90 % after ≈ 4 hours when using 3 mW continuous wave CW light at 250 nm [35].

The second guiding mechanism is based on photonic bandgaps and was first demonstrated in 1998 [82]. In analogy to electronic semiconductors, where due to the crystal symmetry an electronic band gap is established, the periodicity in these materials creates a photonic band gap [78, 80, 81, 36]. The periodic cladding structure can have different shapes, e.g. a honeycomb structure [82] or a triangular structure (Figure 15 b)) [36]. Modes in the periodically ordered glass fractions, which together with the air holes form the cladding of the fiber, establish frequency dependent transmission bands separated by bandgaps, where no modes can be transmitted in the cladding. Therefore, light transmitted in a hollow-core, which in the electronic bandgap analogy corresponds to a defect, can be confined as long as its frequency

lies in the range of these bandgaps. Here, no coupling to the cladding exists and the light is confined. The confinement loss of these fibers should theoretically be much lower than the limit for standard step index fibers of ≈ 0.16 dB/km set by Rayleigh scattering in the glass. But due to scattering at the intrinsic roughness of the air/glass interface in the photonic bandgap fibers, the minimum loss has not reached this theoretical limit [81]. An additional drawback of these fibers is their limited transmission bandwidth.

The third guiding mechanism is not yet fully understood. The photonic structure of this class of fibers consist of relatively large air-filled areas surrounded by glass struts on the order of hundreds of nm. The fiber cladding can contain different structures, e.g. a square lattice [83] or the Kagomé structure (Figure 15 c)) as the fibers investigated in the following sections. For these fibers, the cladding structure does not establish photonic bandgaps, but light is still guided in a hollow core. One proposed explanation is based on a low density of photonic states in the cladding of the fiber [84]. This together with the extremely low overlap of the core mode with the surrounding glass inhibits the coupling between core and cladding modes and confines the light in the fiber core [83]. Furthermore, a phase mismatch between core and cladding modes reduces the coupling and consequently enhances the confinement [84]. Another explanation for the guiding mechanism in these fibers is using a model based on Bragg fibers (Figure 15 d)), where the cladding contains concentric glass rings separated by air. In the actual structure, the glass connections needed to mechanically support the rings are causing loss resonances [85]. Recent studies on Kagomé-PCF indicate that only the inner silica ring is necessary to guide the light and the guiding does not benefit from additional layers of air holes [86], in contrast to the predictions from the inhibited coupling and the Bragg fiber model. Further investigations are necessary to develop a complete description of the guiding mechanism in the low loss regions of these fibers. However, the principal high loss bands of the fibers can be calculated using the antiresonant reflecting optical waveguide (ARROW) model [87, 88]. According to the model, the loss bands occur for wavelengths, where the core mode phase-matches to modes guided in the core wall, i.e., when [87, 81]:

$$\kappa h_{cw} \sqrt{n_g^2(\lambda) - n_m^2} = m\pi \quad (48)$$

where m is an integer number, n_m is the modal index (slightly less than 1 for the fundamental mode), h_{cw} is the core wall thickness, $\kappa = 2\pi/\lambda$ is the vacuum wavevector and $n_g(\lambda)$ is the wavelength-dependent refractive index of the glass. By proper adjustment of the parameters during drawing of the fiber, the wall thickness can be adjusted so that the loss bands are furthest away from the wavelength of interest.

Recent experiments on nonlinear spectral broadening in gas-filled

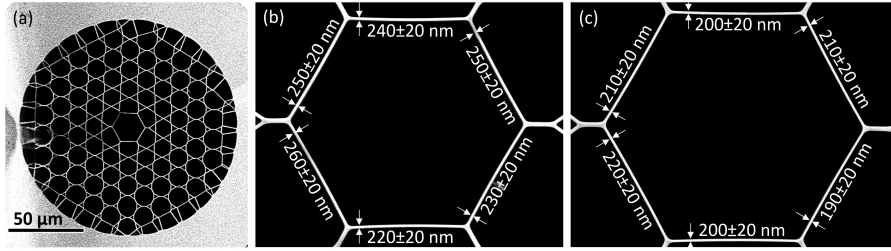


Figure 16: **Scanning electron micrographs (SEMs) of the investigated fibers.** (a) SEM of fiber sample A. (b) Close-up of the core structure of fiber A with core-wall thickness measurements. The core diameter (measured flat-to-flat) is $\approx 19 \mu\text{m}$. (c) Similar close-up for fiber B, with flat-to-flat core diameter of $\approx 20 \mu\text{m}$. SEM images were provided by the Max Planck Institute for the Science of Light, Erlangen.

hollow core Kagomé-style PCF have shown that these fibers are able to guide ultrashort pulses of UV light with losses of order 3 dB/m [89]. Other experiments have demonstrated single-mode beam quality in Kagomé-PCF. Additionally, finite element simulations indicate that the light-in-glass fraction in these fibers is typically $< 0.01 \%$ [90], which circumvents the problem of UV-induced long-term damage in the glass. Recently a Kagomé-PCF with 2 dB/m loss at 355 nm was demonstrated, but due to the relatively large core diameter ($\approx 30 \mu\text{m}$) it was highly multimode [91]. Kagomé-PCF can be made effectively single-mode by decreasing the core size until higher-order modes have significantly higher propagation losses than the fundamental mode. Since in Kagomé PCF the loss is expected to depend strongly on variations in the core wall thickness, we investigated fibers with different core wall thicknesses for single mode guidance of light at 280 nm as described in the following.

4.2 CHARACTERIZATION OF PCFS

The investigated PCFs were drawn in the group of Philip Russell at the Max Planck Institute for the Science of Light. The output of the fibers with core diameter larger than $20 \mu\text{m}$ was interspersed with contributions of higher order modes. For two fibers with a core diameter of $D \approx 20 \mu\text{m}$, effectively single mode guidance was observed. Scanning electron micrographs (SEMs) of the structures of these two fibers are displayed in Figure 16.

Careful analysis of the SEMs show that for the first fiber (fiber A in the following) the core wall thickness h_{cw} varies over the range $240 \pm 20 \text{ nm}$, whereas for the second fiber (fiber B) it varies over the range $205 \pm 15 \text{ nm}$. For the characterization of the UV guiding properties of the two fibers, the frequency quadrupled output of a fiber

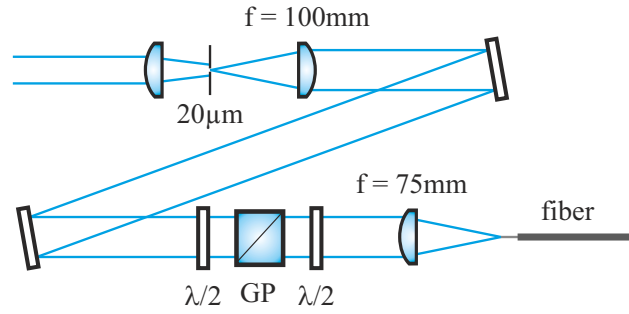


Figure 17: **Fiber test setup.** After mode cleaning the beam shape with a $20\ \mu\text{m}$ pinhole a telescope with a magnification of 0.75 is used for mode matching into the PCF. Abbreviations: $\lambda/2$: half waveplate; GP: Glan Polarizer.

laser at around $280\ \text{nm}$ was used. After the second doubling cavity the beam was extracted from the setup providing an output power of approximately $4\ \text{mW}$ after spatial filtering. Since more output power was desired for the long-time test, the second laser in our setup usually used for the coherent control, driving the ${}^2S_{1/2} \rightarrow {}^2P_{3/2}$ transition, was used. This laser provides an output power of more than $20\ \text{mW}$ at a wavelength of around $280\ \text{nm}$ after mode cleaning.

A schematic of the fiber test setup is displayed in Figure 17. After the second frequency doubling cavity, the beam is extracted from the experimental setup and focused onto a pinhole with a diameter of $20\ \mu\text{m}$. After collimation, using a lens with a focal length of $100\ \text{mm}$, a Glan polarizer is used to assure linear polarization in front of the fiber. The beam is then focused onto the fiber end using a lens with a focal length of $75\ \text{mm}$. This results in a beam diameter of approximately $15\ \mu\text{m}$, matched to the mode field diameter ($\text{MFD} \approx \frac{\pi}{4}D$, where D is the core diameter) of the Kagomé PCF [92].

4.2.1 Characterization of the output modes of the fibers

The robustness of the single-mode guidance was tested by monitoring the output beam profile while translating the input coupling beam across the input facet of the fiber. Little evidence of higher-order modes was observed (Figure 18). We note that in Ref. [91] the $350\ \text{nm}$ light output from a fiber with $30\ \mu\text{m}$ core diameter showed a highly multimoded pattern. The Kagomé-PCFs considered here are effectively single-mode due to a smaller core diameter ($\approx 20\ \mu\text{m}$). Therefore higher-order modes experience larger propagation losses, which means that the fibers act as mode-cleaners.

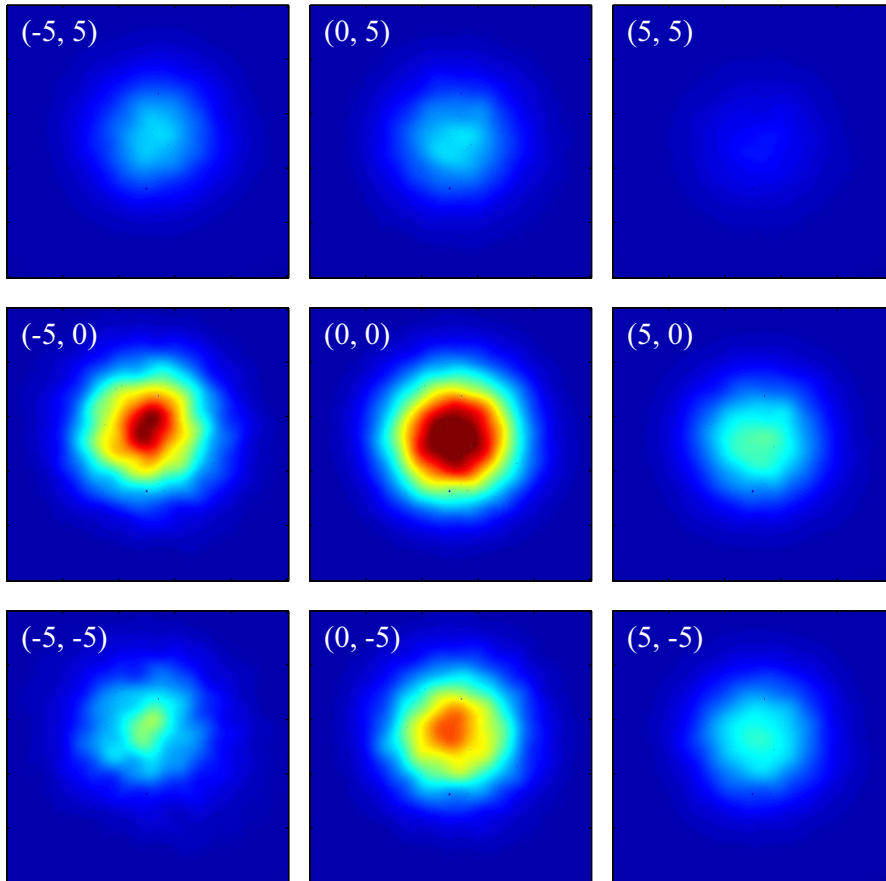


Figure 18: **Measured near-field intensity profiles.** The output profiles of fiber A were measured for different transverse positions of the input beam. The coordinates refer to the horizontal and vertical displacements (in μm) of the focused laser spot from the core center. The intensity profiles are not perfectly symmetrical with respect to off-center displacements; this could both be due to asymmetry in the fiber structure as well as because the transverse position could not be controlled to better than $\approx 1 \mu\text{m}$

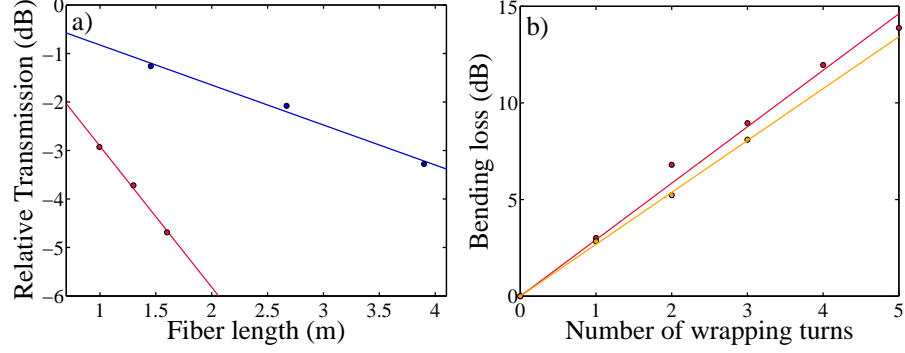


Figure 19: **Attenuation and bending loss measurements.** (a) Cut-back loss measurement for fiber A (red) and fiber B (blue) at a wavelength of 280 nm. The dB scale is normalized so that 0 dB corresponds to the transmitted power without the fiber. The linear fits correspond to a loss of 2.9 dB/m (red, fiber A) and 0.8 dB/m (blue, fiber B). (b) Bending loss measurements for fiber A for bending radii of 1.6 cm (red) and 4.0 cm (blue). The linear fits correspond to 2.7 dB/m (red) and 2.9 dB/m (blue) for the two different bend radii.

4.2.2 Loss, bending, and polarization properties

The loss of the fiber was measured using the cut-back technique, without changing the fiber in-coupling and keeping the fiber as straight as possible to minimize bending loss. The results are shown in Figure 19 a). As described in Section 4.2, fiber A had a measured core-wall thickness in the range $\approx 220 - 260$ nm (Figure 16), and yielded a loss of ≈ 3 dB/m, whereas for fiber B the measured loss was ≈ 0.8 dB/m for a core-wall thickness in the range $\approx 190 - 220$ nm. As shown in finite element method FEM simulation performed by the group of Philip Russell [76], there is a strong sensitivity of the loss resonances to the core wall thickness. Azimuthal asymmetry of the core walls and their expected variation along the actual fiber therefore do not allow a direct quantitative comparison between experiment and simulation. However, the measured losses are compatible with the simulated ones. In particular, the fiber with smaller core-wall thickness exhibits lower losses, since the mean core wall thickness is further away from the main loss resonance around $h_{cw} = 255$ nm. Several mW of power at 280 nm were transmitted, typically $\approx 50\%$ of the launched power for fiber A (≈ 1 m fiber length) and $\approx 70\%$ for fiber B (≈ 1.3 m length). Bending was found to cause large variations in the transmitted power, probably due to enhanced leakage into the cladding and coupling to high-loss higher-order modes. However, we found no bending loss-induced degradation in transmission for fibers which were kept either straight or at bend-radii larger than 20.0 cm. To quantify the bend-sensitivity for smaller bending radii, the output

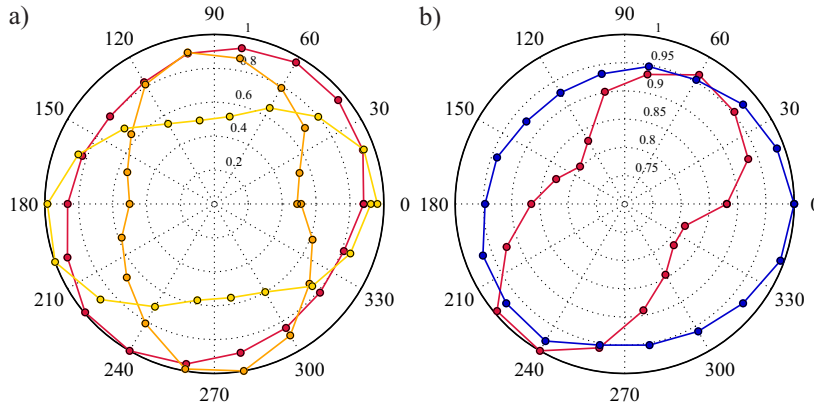


Figure 20: **Polarization measurements.** Polarization dependence of the normalized output power (a) for a 4 m (orange and yellow) and a 1 m (red) piece of fiber A. Between the two measurements of the 4 m piece of the fiber the whole fiber was turned by 4° . (b) comparison of fiber A and fiber B with different core wall thickness; red: fiber A, blue: fiber B.

power was measured while winding fiber A around a mandrel. The transmitted power exhibited strong fluctuations depending on the exact position and twist of the fiber. We believe that this additional loss is caused by geometrical deformation during bending of the fiber. To minimize this effect, the output power was recorded while rearranging the fiber and the maximum measured power was used to derive the bending loss. A fit to the relative transmission for different numbers of wrapping turns led to a loss of 2.9 dB/m for a bending radius of 1.6 cm and a loss of 2.7 dB/m for a bending radius of 4.0 cm as shown in Figure 19 b). The similarity of these values might be due to different remaining contributions from the loss caused by geometrical deformation and the associated enhanced leakage into the cladding. A more elaborate method excluding this additional loss would be necessary to resolve this issue.

It was also found that the transmission depends on the polarization state of the light. This is normally not expected in Kagomé-PCFs with perfect six-fold symmetry, but as discussed above, the loss is sensitive to nm-scale variations in core-wall thickness. Azimuthal variations in core-wall thickness can therefore result in polarization-dependent loss. In Figure 20 a) the normalized transmission along 4 m (yellow and orange) and 1 m (red) lengths of fiber is plotted, while varying the linear input polarization. For the 4 m piece of fiber A we find $\approx 50\%$ (0.8 dB/m) difference in output power between orthogonal input polarizations, whereas for the 1 m length of the same fiber there is a maximum difference of $\approx 20\%$ (1.0 dB/m). We verified that this effect was really due to the structure of the fiber by rotating the 4 m piece of the fiber in the setup. As shown in Figure 20 a) this just rotated the shape of the polarization dependence, supporting that the

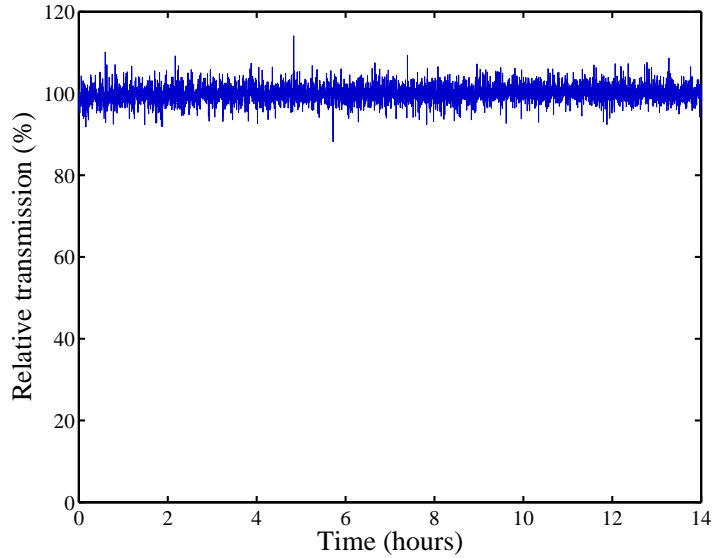


Figure 21: **Long-time transmission measurement.** Relative transmitted power in the Kagomé-PCF over time when 15 mW of 280 nm CW light is coupled into the fiber.

effect was indeed due to the structure of the fiber. We further compared two different fibers with different core wall thicknesses in Figure 20 b). There is a maximum $\approx 20\%$ (1.0 dB/m) difference in output power between orthogonal polarizations for fiber A, and a maximum $\approx 10\%$ (0.5 dB/m) difference for fiber B. Given the high sensitivity of loss on the core-wall thickness, the observed $\approx 10 - 20\%$ variation in transmission is compatible with the observed azimuthal asymmetry in core-wall thickness (Figure 16 b), c)). This is supported by the even stronger polarization dependent loss for the 4 m long fiber. Other asymmetries in the structure (e.g. small variations in core-wall length) could also play a role.

4.2.3 Long-time transmission measurement

As mentioned in the introduction, there is a demand for optical fibers that can deliver UV light with high beam quality without degradation due to UV-induced damage to the glass core. FEM calculations indicate that less than 0.01 % of the light in a perfect Kagomé-PCF is guided in the glass [90], which suggests that UV-induced damage should be largely eliminated. To investigate this, 15 mW of 280 nm CW light was launched into fiber A and the transmission monitored continuously over time. As shown in Figure 21, there are no signs of UV-induced damage over the 14 hours of continuous measurements. We additionally made experiments in which the Kagomé PCF was left to transmit around 50 % of more than 15 mW input UV light for altogether more than 100 hours. Within the measurement error we could not detect a change in the transmission over this time period.

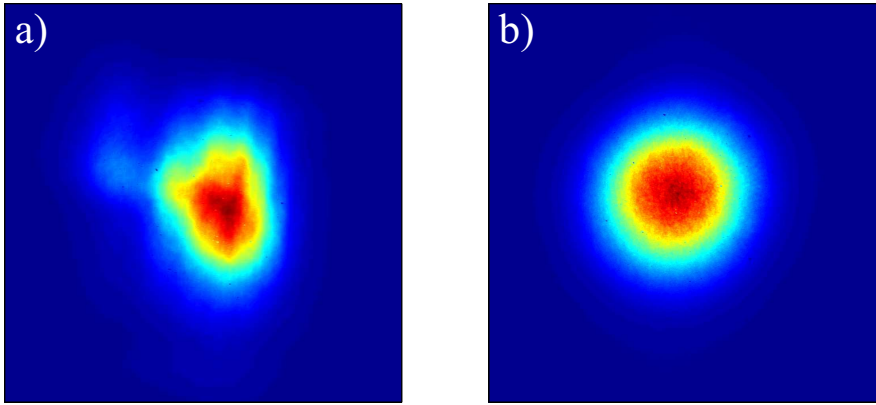


Figure 22: **Beam profile with and without fiber.** a) The AOMs in the optical setup distort the beam profile, which leads to an additional intensity gradients across the beam profile. b) The Kagomé PCF cleans the profile to a near-Gaussian transverse mode shape.

4.3 APPLICATION

In order to study the applicability of the fiber in trapped ion experiments, an intensity stabilization set-up was implemented. The ends of two 1.2 m long pieces of fiber B were fixed with adhesive tape in V-grooves of an aluminum block. The fibers were used to replace two periscope systems that connected two stacked platforms. The beam was widened to a waist of approximately 0.7 mm ($1/e$ radius) using a telescope and then focused down using a lens with a focal length of 75 mm. With this simple setup, we achieved typically more than 50 % transmission through both fibers using approximately 6 mW of input power. The distance from the output face of the fibers to the trapped ion was kept as short as possible to minimize residual pointing fluctuations. The distance was approximately 50 cm, limited by the distance of the vacuum windows from the trap and the needed optical setup for intensity stabilization. As mentioned above, pointing instabilities lead to intensity fluctuations at the position of the ion and can therefore limit the laser control of its internal state. As described in Section 3.3, we use a setup of several AOMs to bridge the frequency difference between the two qubit states for the coherent manipulation of the $^{25}\text{Mg}^+$ ions. Since no single-mode fibers were previously available at a wavelength of 280 nm, the original setup consisted of free-space beam-paths more than 5 m long. Air turbulence and small vibrations of mirrors as well as other optical components led to noticeable pointing fluctuations at the position of the ion.

Furthermore, the AOMs distorted the beam shape, which caused additional intensity gradients across the beam profile as shown in Figure 22. These distortions arise from the limited size of the transducer that creates the sound wave and additional thermal effects [93]. We minimize thermal effects during the sequence by supplying addi-

tional RF pulses to the AOMs at the end of the sequence to keep their temperature as constant as possible. After the AOMs, the two Raman laser beams were cleaned to a near-Gaussian transverse mode shape using the hollow core Kagomé-PCFs discussed here. This effectively turns beam pointing fluctuations before the fiber into intensity fluctuations after the fiber. After the fiber, the intensity was stabilized using an electronic control loop. The effect of beam-pointing fluctuations was investigated by measuring the contrast of laser-driven coherent internal state oscillations both with and without a Kagomé-PCF. To this end we recorded the internal state of the ion after coupling the two hyperfine states via the Raman lasers for different pulse durations (Rabi flopping). The excitation probability is determined by averaging the result of approximately 250 repetitions of the experiment per Raman interaction time. If the position of the laser beam and therefore the light intensity on the ion fluctuates, the Rabi frequency (which is a function of the laser intensity) will change between subsequent experiments. During the averaging process this results in a reduction of the measured Rabi oscillation contrast (see Figure 14), which can be described as a damped oscillation of the ground state population [94]:

$$P_{|\downarrow\rangle}(t) = \frac{1}{2} [1 + e^{-\gamma t} \cos(\Omega_0 t)], \quad (49)$$

where Ω_0 is the mean Rabi frequency, $\gamma = \Gamma\Omega_0^2/2$ the decay rate of the Rabi oscillations, and Γ a scale-factor for the intensity noise. Competing effects that reduce the Rabi oscillation contrast further are the motional excitation of the ion in the trap due to its non-zero temperature, and off-resonant scattering of the Raman beams [95]. Off-resonant scattering is not a fundamental limitation, since it can be mitigated by detuning the Raman resonance further from the atomic transition. Preparation of the ion close to the motional ground state of the $|\downarrow\rangle$ -state via Raman sideband cooling [65] at the beginning of each experimental cycle, eliminates the influence of motional excitation on the Rabi-flopping contrast. After cooling to a mean motional excitation of $\bar{n} = 0.02 \pm 0.02$, we applied the Raman coupling for different pulse durations while actively stabilizing the intensity of the Raman lasers using a sample-and-hold intensity stabilization circuit.

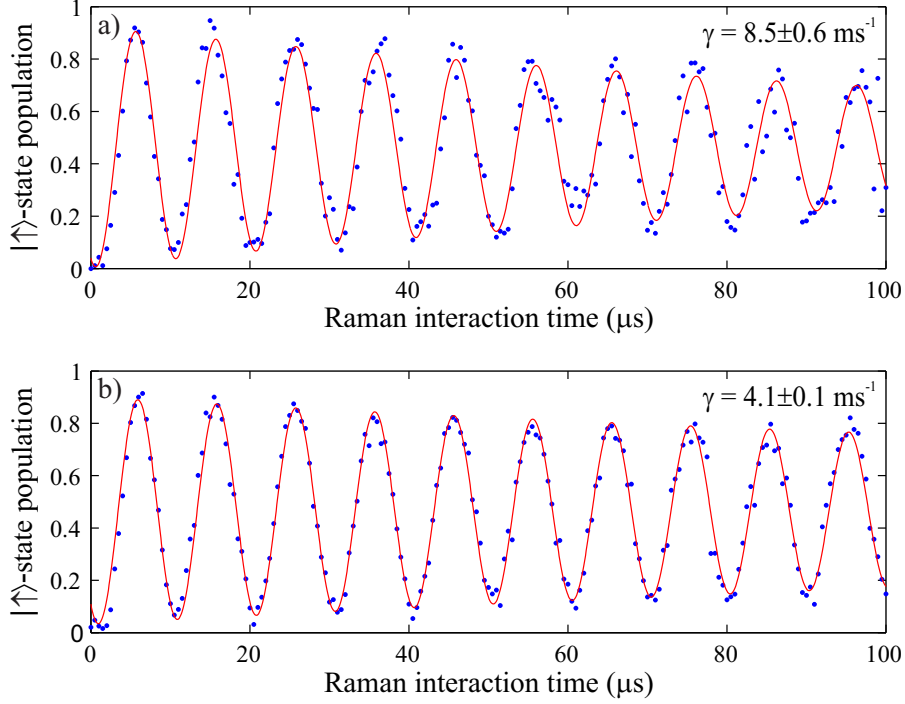


Figure 23: **Measured Raman Rabi oscillations.** Raman Rabi oscillations (a) without Kagomé-PCF and (b) with Kagomé-PCF in the set-up. The decay rate is extracted from a fit to Equation (49) and the mean value over 7 measurements is displayed in the corresponding graphs. The residual decay is dominated by off-resonant excitation from the Raman lasers due to the limited Raman detuning of ≈ 9.2 GHz. Errorbars are on the order of 3 % and are omitted for clarity.

Figure 23 shows experimental data for the Rabi flopping curves with and without the Kagomé-PCF, together with a corresponding fit according to Equation (49). The extracted dephasing rate γ is averaged over 7 different measurements in each configuration, where one of the 7 measurements is displayed in Figure 23. The resulting weighted average of the decay rates is $4.1 \pm 0.1 \text{ ms}^{-1}$ with, and $8.5 \pm 0.6 \text{ ms}^{-1}$ without the Kagomé-PCF in place, respectively. The relatively strong residual decay is dominated by off-resonant excitation of the ion to the electronically excited $^2P_{3/2}$ state, due to the limited Raman detuning of ≈ 9.2 GHz. As shown in Section 3.3.1, the measurements of off-resonantly coupled internal state of the ion yielded the decay rates of the two states $\gamma_{|\downarrow\rangle} = 1.1 \pm 0.1 \text{ ms}^{-1}$ and $\gamma_{|\uparrow\rangle} = 4.4 \pm 0.4 \text{ ms}^{-1}$, which are comparable with the residual dephasing rate of the Rabi oscillation with the Kagomé-PCF in the set-up (see Figure 23 b)). Further investigations at a larger Raman detuning would be necessary to determine the ultimate limit of residual Rabi frequency fluctuations. The experimental results indicate that Kagomé-PCF can significantly reduce one of the dominant errors in coherent manipulation of trapped ions [75]. An additional advantage

of adding the Kagomé-PCF to this type of setup for trapped ion experiments is that any realignment of the beam-path before the fiber does not shift the focal position on the ion, which is typically cumbersome to achieve in free-space set-ups.

4.4 CONCLUSIONS AND OUTLOOK

In this chapter we investigated the applicability of Kagomé-style photonic crystal fibers for transmission of UV radiation. We showed that Kagomé-PCFs are able to guide several mW of UV radiation in a single mode fashion with losses below 1 dB and with no additional loss due to bending for typical bend radii larger than 20.0 cm. Additionally we showed, that unlike in solid-core fibers, there is no perceptible drop in transmission due to UV-induced damage, even after 100 hours of operation at 15 mW.

Furthermore, in this chapter we showed that the Kagomé PCF mounted in a simple setup and without additional treatments can be used to significantly reduce beam pointing fluctuations and serve as an alignment tool for large optical setups, as the output facet of the fiber is fixed with respect to the ion's position.

The performance of the fibers may be further improved by shaping the core differently to optimize the core surround during the fiber fabrication process, instead of having a hexagonal shape. Recent experiments on hypocycloid core shaped hollow-core Kagomé PCF show transmission in the infrared and the optical regime with loss of 17 dB/km at 1064 nm [96]. This reduction in loss can be explained by a reduced spatial overlap of the core field and the silica-surround, which is mainly responsible for the loss of these fibers.

An alternative approach to provide single mode fibers in the UV regime was recently reported and is based on hydrogen-loading of a solid-core photonic crystal fiber [97]. Large mode area fibers were used to achieve a relatively low optical power density in the core and provide the guidance of only a single mode. The effect of UV solarization [98] was reduced by exposing the fiber to high pressure hydrogen and subsequently illuminating the fiber with UV radiation. The UV radiation forms color centers in the glass, that react with the hydrogen. This reaction deactivates the color centers or shifts their resonance frequency. This prevents the degradation of the fiber and reduces its attenuation in the wavelength range from 200 nm to 400 nm. These fibers provide a low bending sensitivity and a comparable loss to the Kagomé fibers presented in this chapter. However, the Kagomé PCF may be advantageous for high power or pulsed laser applications since the light is guided in air for the Kagomé PCFs presented here, whereas the radiation in the hydrogen loaded fibers is still guided in glass.

MOTIONAL STATE INDEPENDENT TRANSFER USING STIMULATED RAMAN ADIABATIC PASSAGE

In this chapter we investigate the stimulated Raman adiabatic passage (STIRAP) technique to transfer population between two electronic levels independent of the ions' motion. In the spectroscopy technique described in Chapter 6 we use the STIRAP technique to detect the residual motional ground state population after motional excitation. To do so, we use a red sideband pulse that transfers all the population that is not in the motional ground state to an electronic excited state. Here, the coupling between electronic levels depends on the specific motional state of the ion in the trap (see Section 2.4). The signal obtained from PRS is based on motional excitation of a common normal mode of the ions, leaving the motional state of the ion distributed over several trap levels. Under these conditions, it is not possible to implement a π pulse for all motional states simultaneously. Consequently, we need a technique that is independent of the coupling strength, to ensure efficient transfer between the electronic levels. This is the case for adiabatic transfer schemes. Here the population inversion between two levels is achievable as long as the adiabatic theorem is fulfilled. This theorem was first proven by Max Born and Vladimir Fock in 1928. It states that [99]:

If a physical system is initialized in a specific quantum state and it is changed adiabatically, the transition probability to another state of the system is infinitely small.

Adiabatic means that the total energy of the system, which is described by the time dependent Hamiltonian, varies slowly in time compared to the energy gap between the eigenstates. Thus, a preparation process obeying this theorem can be used to transfer population between atomic states. The general idea is to use laser fields to create new eigenstates of the coupled laser-atom system. Then, these eigenstates are rotated adiabatically, with respect to the bare atomic state basis, from the initial to the target state. As long as the rotation is slow compared to the energy gap between the states, the system will stay in its eigenstate and the population is transferred between the two atomic states. Adiabatic passage was first demonstrated in nuclear magnetic resonance experiments, where the nuclear magnetic moment of atoms in a solid were controlled using oscillating magnetic fields [100]. Later, adiabatic techniques have been demonstrated in atomic and molecular systems using laser pulses [101, 102, 103]. A

detailed review of adiabatic processes used to control populations in atoms and molecules can be found in references [104, 105].

In trapped ion systems dominantly two techniques were investigated, namely the rapid adiabatic passage RAP [106] and the stimulated Raman adiabatic passage [40] (STIRAP) technique. In the RAP technique a frequency and amplitude chirped pulse is used to tailor the dynamics of the dressed state used for the transfer of population between the two atomic states. In the experiment, the time dependence of the intensity has a Gaussian shape, whereas the frequency is varied linearly in time. The STIRAP technique, on the other hand, employs delayed pulses for the transfer. Additionally, in a trapped ion system the manipulation of motional states using RAP on sideband transitions was demonstrated [107]. Here we present for the first time theoretical and experimental studies of the STIRAP transfer using sideband transitions and show the applicability of the technique to efficiently detect the residual groundstate population of a motionally excited ion.

This chapter is structured as follows. The next section provides an introduction to the STIRAP theory followed by a short description of the density matrix simulations and the experimental implementation in section Section 5.2. Afterwards, the simulated results are used to describe the transfer process and experimental parameters for efficient transfer in our setup are derived and compared to measurements. After optimizing the parameters, the main result, the motional independent transfer, is investigated in Section 5.3.2. Afterwards, the transfer efficiency of the STIRAP process is compared to the π pulse technique in Section 5.3.3. The chapter ends with a discussion of the results.

5.1 STIRAP THEORY

In the following, we investigate the population transfer between two energy states of an atom using the stimulated Raman adiabatic passage (STIRAP) technique. The technique can be described considering the Hamiltonian of a three level system coupled to two light fields in the rotating wave approximation (see Equation (38)). As in chapter Section 2.5, the laser coupling the $|1\rangle$ and the $|3\rangle$ state is called the pump laser and the laser coupling the $|2\rangle$ and the $|3\rangle$ state is called the Stokes laser. For the technique we introduce time dependent couplings $\Omega_p(t)$, $\Omega_s(t)$ between the energy levels, shown together with the corresponding energy diagram in Figure 24. The dynamics of the system can be described in the eigenbasis of the Hamiltonian, but the derivation of the eigenvalues and the eigenvectors of the Hamiltonian is not trivial. Explicit and case sensitive expressions of the eigenvalues and eigenvectors are given in reference [108]. For the relevant case in our system, where we assume two photon resonance $\Delta_p = \Delta_s = \Delta$,

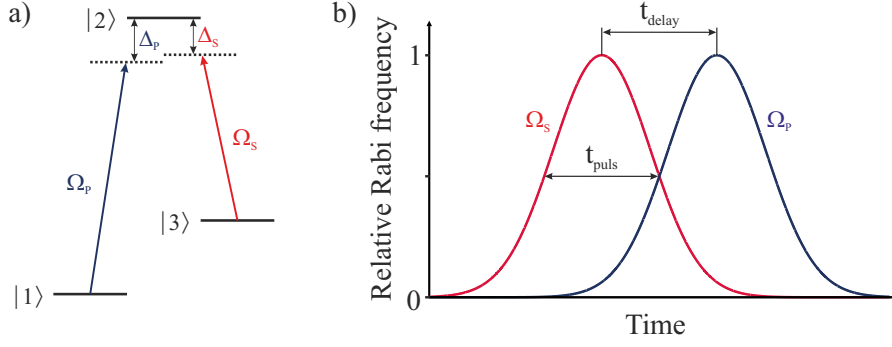


Figure 24: **STIRAP pulse sequence.** a) Three level atom together with the coupling laser Rabi frequencies Ω_p and Ω_s . b) Time dependence of the Rabi frequencies normalized to their maximum value. Additionally the pulse length is defined as the full width at half maximum and the delay of the two pulses is defined, as the separation of the Rabi frequency maxima.

the eigenvalues of the Hamiltonian can be derived and dividing by \hbar , the corresponding eigenfrequencies are given by:

$$\begin{aligned}\omega_0 &= 0, \\ \omega_+ &= \frac{1}{2} \left(\Delta + \sqrt{\Delta^2 + \Omega_p^2 + \Omega_s^2} \right), \\ \omega_- &= \frac{1}{2} \left(\Delta - \sqrt{\Delta^2 + \Omega_p^2 + \Omega_s^2} \right).\end{aligned}\quad (50)$$

Furthermore, the energy eigenstates of the coupled atom-light-system are given by:

$$\begin{aligned}|a^0\rangle &= \cos \Theta |1\rangle - \sin \Theta |3\rangle, \\ |a^+\rangle &= \sin \phi \sin \Theta |1\rangle + \cos \phi |2\rangle + \sin \phi \cos \Theta |3\rangle, \\ |a^-\rangle &= \cos \phi \sin \Theta |1\rangle - \sin \phi |2\rangle + \cos \phi \cos \Theta |3\rangle,\end{aligned}\quad (51)$$

where the so-called mixing angles Θ and ϕ are related to the Rabi frequencies and the detuning of the coupling lasers from the upper state as follows:

$$\tan \Theta = \frac{\Omega_p}{\Omega_s}, \quad (52)$$

$$\tan \phi = \frac{(\Omega_p^2 + \Omega_s^2)^{1/2}}{(\Omega_p^2 + \Omega_s^2 + \Delta^2)^{1/2} + \Delta}. \quad (53)$$

The eigenstates of the Hamiltonian are called the dressed states of the combined matter-field-system, or in the context of **STIRAP**, the adiabatic states. In the experiment we use the Raman beam configuration described in Section 3.3 for the **STIRAP** sequence where the beams are detuned by 9.2 GHz from the excited state $|2\rangle$. The resonant Rabi frequencies of the two beams are approximately 43 MHz. Therefore, $\Delta \gg \Omega_p, \Omega_s$ and the mixing angle ϕ becomes 0, leading

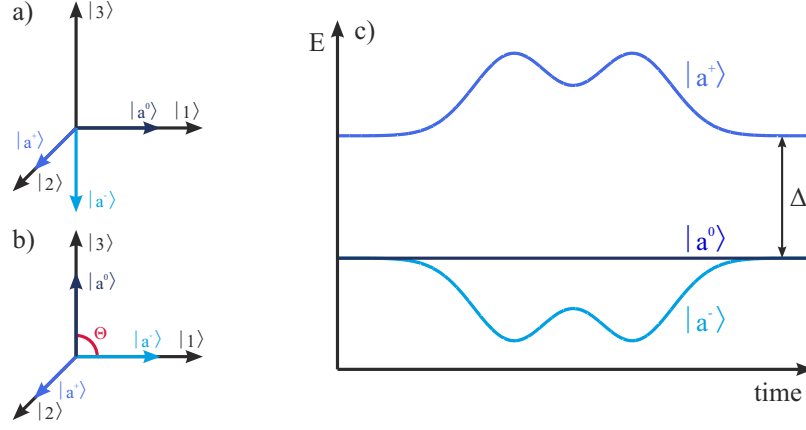


Figure 25: **Eigenenergies and basis of the dressed states.** Dressed state basis for a) the beginning and b) the end of the STIRAP sequence. c) Time evolution of the eigenenergies of the dressed states. The energy of state $|a^+\rangle$ is separated by the detuning from the other two states, which are split by the applied laser field.

to $\tan \phi \rightarrow 0$ according to Equation (53). Then the eigenvectors of the system simplify to:

$$\begin{aligned}
 |a^0\rangle &= \cos \Theta |1\rangle - \sin \Theta |3\rangle \\
 |a^+\rangle &= |2\rangle \\
 |a^-\rangle &= \sin \Theta |1\rangle + \cos \Theta |3\rangle
 \end{aligned} \tag{54}$$

For the discussion of the transfer process, we plot the eigenenergy values of the system using the STIRAP sequence displayed in Figure 24. Additionally, the dressed state eigenvectors with respect to the bare state basis are shown for the beginning and the end of the STIRAP sequence in Figure 25. The basic principle of the transfer can be understood from the eigenstate equations Equation (54), the pulse sequence shown in Figure 24, and the eigenenergies. At the beginning of the sequence, only the Stokes laser field interacts with the atom and the adiabatic state $|a^0\rangle$ is aligned parallel to the initially populated electronic ground state $|1\rangle$. Due to the presence of the Stokes laser field, the initially degenerate energies of the system ω_- and ω_0 are split due to the ac stark effect. As long as this energy splitting is large compared to the change of the total energy of the system, no transition to other states will occur and the system stays in its instantaneous eigenstate, as stated by the adiabatic theorem. By ramping the strength of the relative couplings between the three states such that only the pump laser induces a significant coupling at the end of the sequence, we can change the mixing angle Θ from 0 to $\pi/2$ ("counterintuitive" pulse sequence). Doing so, we rotate the dressed state basis with respect to the bare state basis by 90° , which means rotating $|a^0\rangle$ from $|1\rangle$ to $-|3\rangle$ around $|2\rangle$, as shown in Figure 25 a) and b). If adiabaticity is maintained during the process, the population

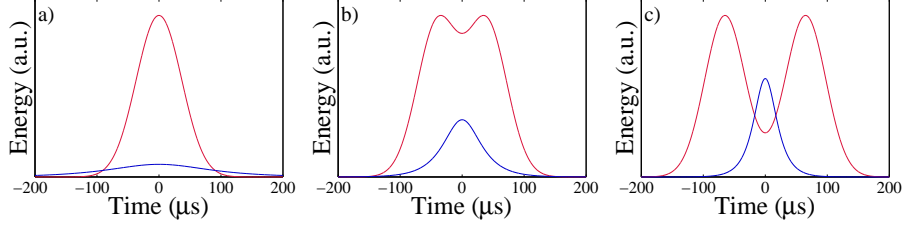


Figure 26: **Time dependence of the adiabatic criterion** The couplings (left side of Equation (57), red) and the energy (right side of Equation (57), blue) are shown for a fixed pulse length of 100 μs and (a) a delay time of 30 μs , (b) a delay time of 80 μs and (c) a delay time of 130 μs .

will stay in the eigenstate $|a^0\rangle$ and will follow the rotation, transferring it from the bare state $|1\rangle$ to state $|3\rangle$ without populating state $|2\rangle$. Here we can see that the transfer is also possible if the pump and the Stokes lasers are resonant with the one photon transitions, although state $|2\rangle$ has a short lifetime. This is one of the salient features of the **STIRAP** process discussed in the literature, which is not possible using other coherent manipulations techniques. From Equation (54) we can see that in the far detuned case we can use the "intuitive" pulse sequences as well to transfer the population, i. e. pump pulse preceding the Stokes pulse. For this case, the eigenstate $|a^-\rangle$ is aligned parallel to $|1\rangle$ at the beginning of the sequence and is then rotated to $|3\rangle$. As mentioned above, the adiabatic criterion has to be fulfilled in the **STIRAP** sequence, i.e. the energy splitting must be larger than the couplings between the states [102, 109]:

$$\langle a^0 | \frac{d}{dt} | a^\pm \rangle \ll |\omega^\pm - \omega^0| \quad (55)$$

The left side of the equation can be evaluated and it reads for the two states $|a^\pm\rangle$:

$$\begin{aligned} \langle a^0 | \frac{d}{dt} | a^+ \rangle &= 0, \\ \langle a^0 | \frac{d}{dt} | a^- \rangle &= -\dot{\Theta} = \frac{\dot{\Omega}_p \Omega_s - \Omega_p \dot{\Omega}_s}{\Omega_p^2 + \Omega_s^2} \end{aligned} \quad (56)$$

Here we see that transitions to state $|2\rangle$ are not allowed due to the large detuning. We now insert the second equation in Equation (55) and get:

$$\frac{\dot{\Omega}_p \Omega_s - \Omega_p \dot{\Omega}_s}{\Omega_p^2 + \Omega_s^2} \ll |\omega^\pm - \omega^0| \quad (57)$$

We get a time dependent adiabatic criterion which is plotted for three cases, i.e. for a pulse length of 100 μs and a delay time of 30 μs , 80 μs and 110 μs in Figure 26. We see that, in the case of long delay times, the adiabatic criterion is not fulfilled in between the two pulses. In contrast, if short delay times are used, the adiabatic criterion is not fulfilled at the beginning and the end of the pulse sequence. This means

that transitions between the adiabatic states $\langle a^0|$ and $\langle a^+|$ may occur for these cases. At the time in between the two pulses adiabaticity can be obtained by either using long pulses or choosing a short delay. But, as shown in Figure 26, the adiabatic criterion is not fulfilled for small delay times at the beginning and the end of the sequence. Therefore, transitions between $|a^0\rangle$ and $|a^-\rangle$ occur, leaving the ion in a superposition of state $|a^0\rangle$ and state $|a^-\rangle$, when the adiabatic criterion starts to be fulfilled and thus hindering complete population inversion. As we have seen in this section, there is a certain parameter regime where adiabatic transfer is possible. To determine appropriate experimental parameters, where the population transfer is efficient, we have performed density matrix simulation and implemented the technique experimentally, as described in the following.

5.2 STIRAP SIMULATION AND IMPLEMENTATION

5.2.1 STIRAP simulation

We used the density matrix formalism to perform numerical simulations and determine the parameter regime for efficient population transfer using the STIRAP process. Therefore, we integrated the master equation numerically and derived the time dependence of the atomic state populations. In general, the master equation can be expressed as:

$$\frac{d\rho}{dt} = \mathcal{L}\rho. \quad (58)$$

Here \mathcal{L} is the Liouvillian operator. Our qubit states $|1\rangle$ and $|3\rangle$ are magnetic sub-states of the hyperfine splitted ground state of the $^{25}\text{Mg}^+$ ion and spontaneous emission from these long-lived states is neglected in the simulation. The detuning of the lasers with respect to the excited $|2\rangle$ state is $2\pi \cdot 9.2\text{GHz}$ and, as discussed in Section 3.3, the off-resonant scattering rates are on the order of 1.1 ms^{-1} and 4.4 ms^{-1} for the two hyperfine ground states. This off-resonant scattering destroys the coherence between the atom and reduces the detected signal. However, this effect is small and since the consideration of off-resonant scattering increases the complexity of the simulation excessively, we neglected this effect in the simulations. In this case the time evolution of the system can be described by a Hamiltonian \mathcal{H} and the Liouvillian acts on the density matrix as follows:

$$\mathcal{L} = -i[\mathcal{H}, \rho] = -i(\mathcal{H}\rho - \rho\mathcal{H}) \quad (59)$$

The quantized motion of the ion in the trap is included in the simulations as the tensor product of the electronic and the harmonic trap

levels:

$$|\psi\rangle = |e\rangle \otimes |n\rangle \quad (60)$$

where $|e\rangle$ and $|n\rangle$ describe vectors containing the electronic levels and the trap levels, respectively. This way, we are able to simulate carrier as well as sideband transitions. The time dependence of the **STIRAP** process is incorporated by time-dependent Rabi frequencies in the Hamiltonian, where for the simulation a Gaussian pulseshape was assumed. The parameters of the pulses are defined as:

$$\begin{aligned} \Omega_s(t) &= \Omega_{s,\max} \cdot \exp\left(-\frac{(t-t_s)^2}{2t_{\text{width}}^2}\right) \\ \Omega_p(t) &= \Omega_{p,\max} \cdot \exp\left(-\frac{(t-t_p)^2}{2t_{\text{width}}^2}\right), \end{aligned} \quad (61)$$

where we define $t_{\text{pl}} = 2\sqrt{2\ln 2} \cdot t_{\text{width}}$ as the pulse length. Furtheron, the $t_{p,s}$ are the centers and the $\Omega_{p,\max}$ and $\Omega_{s,\max}$ are the maximum Rabi frequencies of the two pulses. Additionally, we denote the delay between the pulses as $t_{\text{delay}} = t_s - t_p$.

All the simulations presented in the following were performed using the quantum optics toolbox in the Matlab programming language [110]. Here the density matrix formalism is used to integrate the master equation. Because the Hamiltonian of the system is time dependent, the solver "**solvemc**" is used. This program performs a direct integration of the master equation to calculate the density matrix ρ for consecutive times. More details of this procedure can be found in [111].

5.2.2 Experimental implementation of the STIRAP sequence

In order to compare the simulated with the experimental results we fitted a Gaussian function to the measured pulses. The measured pulse length of the π Raman beam is around 12 % shorter than the pulse length of the σ beam, due to technical imperfections. Therefore we derive an effective pulse length (mean of the Gaussian full width at half maximum **FWHM**) from the fit and measured the effective delay time of the two pulses. These values, which were ranging from a few to two hundred microseconds, are used to compare the measured data to the simulations.

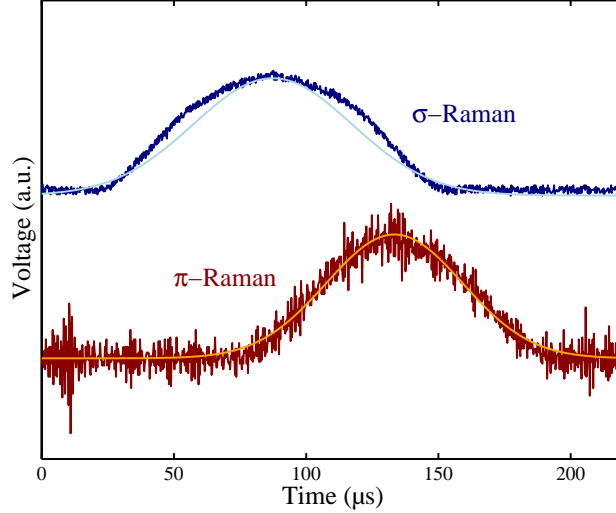


Figure 27: **Measured STIRAP sequence.** Time evolution of the laser intensities of the two Raman beams measured with a photodiode. For comparison fits to Gaussian-shaped pulses are displayed.

5.3 STIRAP RESULTS

5.3.1 Characterization of the STIRAP transfer

In the following, we use the simulation results to investigate the influence of the delay of the two laser pulses for a fixed pulse length of 100 μs for carrier transitions.

We see that both pulse orders, pump preceding Stokes and vice versa, are able to transfer all the population from the initial to the final state. This behavior is a result of neglecting spontaneous emission in the simulation, justified by the large detuning. This is in contrast to the resonant STIRAP process, where during the intuitive pulse order (i.e. pump pulse precede Stokes pulse), the upper state $|2\rangle$ gets significantly populated and due to its short lifetime decays, which destroys the coherence between the atom and the lasers. For the counterintuitive pulse order (i.e. Stokes pulse precede pump pulse) even in the resonant case the state $|2\rangle$ is not populated and complete population transfer is possible. As can be seen in the lower part of Figure 28, for a delay time of 26 μs , the transfer process consists of two contributions, one oscillating and one adiabatic part. For this pulse length the adiabatic criterion is not fulfilled at the beginning of the sequence and the time evolution can be understood as a superposition of Rabi oscillations, which is the transfer mechanism for the case of overlapping pulses (zero delay time), and an adiabatic part of the population transfer, which is the case for an appropriately chosen delay time (shown in Figure 28 c)). In this regime the population transfer strongly depends on the pulse length of the two Raman beams. For a delay time of 80 μs we see adiabatic transfer where the population is transferred

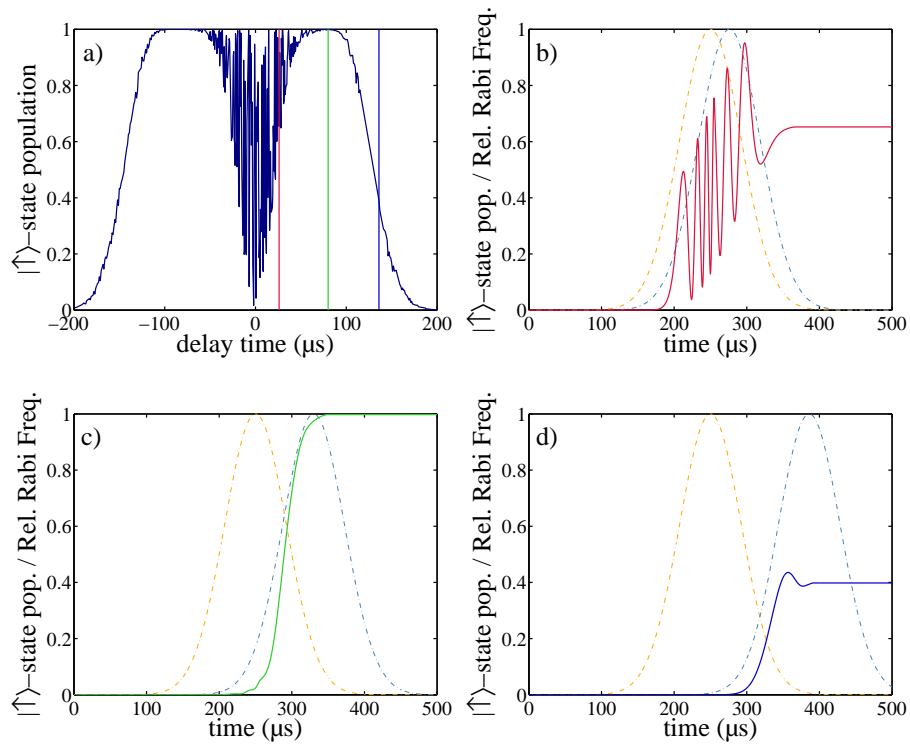


Figure 28: **Simulated delay time dependence for the STIRAP sequence.**
 a) Final state population as a function of delay time of the two STIRAP pulses for a fixed pulse length. The colored bars indicate the fixed delay times for which the time evolution of the population transfer is displayed in b) 26 μs , c) 80 μs , d) 136 μs . In the background of the plots for the time evolution the pulses are displayed (dashed lines, orange: Stokes laser, blue: Pump laser).

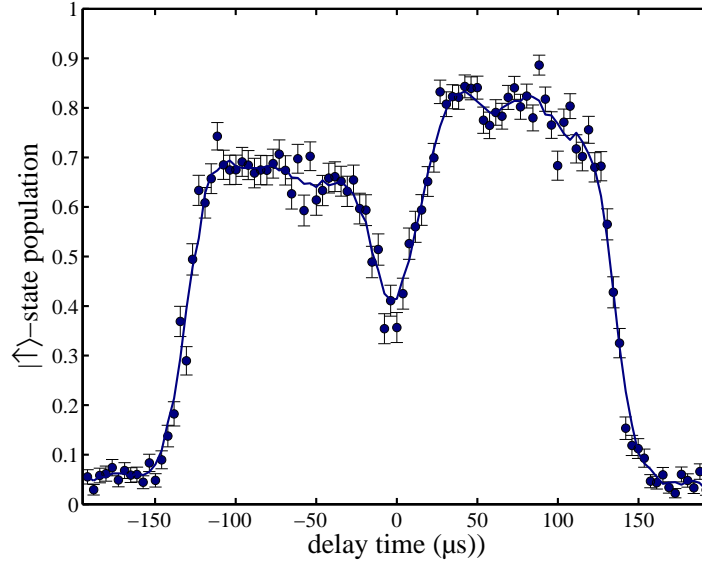


Figure 29: **Scan of the delay time between the two STIRAP pulses.** For the measurements the ion was initialized in the ground state and the laser was driving a carrier transition. The plotted line is a moving average of the data and is added to guide the eye.

almost completely from state $|1\rangle$ to $|3\rangle$, whereas for a delay time of $136\ \mu\text{s}$ the overlap of the pulses is too small, so that the transfer is incomplete.

We investigated the delay time dependence of the population experimentally for the same pulse length for a carrier transition with the ion initialized in the motional ground state, see Figure 29. Here we see that for the counter-intuitive pulse order, the maximum transfer is on the order of 80 %, limited by offresonant excitation. In contrast, the transfer efficiency reaches only 70 % for the intuitive pulse order. This can be explained by the off-resonant couplings involved during the different pulse orders: At the beginning of the sequence the ion is initialized in the $|\downarrow\rangle$ state and the σ^+ polarized Raman beam can only couple off-resonantly to the cycling transition. For this coupling the state is not changed during one excitation/spontaneous emission process. In contrast, for a π polarized beam this process may lead to a change of the atomic state, hindering the subsequent STIRAP transfer. For the population in the $|\uparrow\rangle$ state, which is the atomic state at the end of the sequence, the off-resonant coupling of both lasers is on the same order leading to a comparable depumping. Altogether, this leads to a reduced transfer efficiency for the intuitive pulse order. Therefore, the counterintuitive pulse order is used in our experiment. Despite this reduced contrast, the measured data is in agreement with the simulated one.

We further investigated the transfer probability with respect to the pulse length for different delays between the pulses. For this we in-

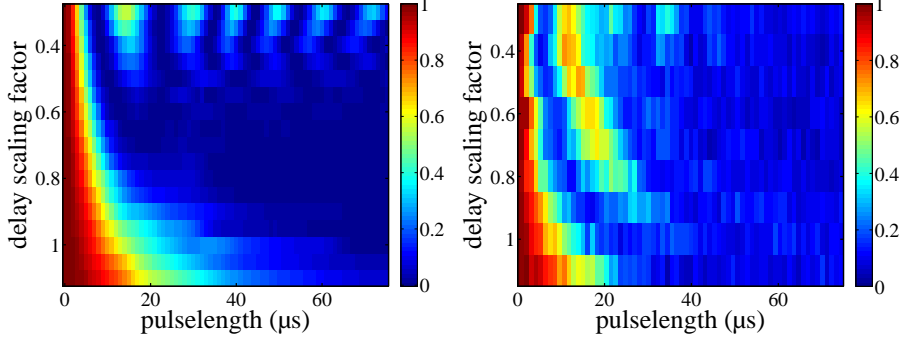


Figure 30: **Simulated and measured transfer probability for different delay scaling factors and pulse length for carrier transitions.** Red corresponds to no and blue to complete transfer. For the simulations and the measurements the ion was initialized in the ground state of motion and the pulse length was scanned for different delay scaling factors according to Equation (62).

roduce a scaling factor s for the delay time, which is related to the pulse length as:

$$t_{\text{delay}} = s \cdot t_{\text{pulse}}. \quad (62)$$

To investigate the transfer efficiency in our setup, we first simulated the transfer probability for carrier transitions with the ion initialized in the motional ground state and compare the result with the measured transfer probability for the same parameters in Figure 30. Experiment and simulation agree qualitatively and show the same effect as in Figure 29, i.e. the transfer depends on the exact pulse length for small delay scaling factors. The behavior can be understood as a superposition of an oscillating part of the time evolution of the vector $|\alpha^-\rangle$ and an adiabatic evolution for the population in state $|\alpha^0\rangle$. The transfer is slightly faster in the experiment than in the simulations, which may be due to a higher Rabi frequency used in the experiment and the imperfect pulse shape of the STIRAP pulses. The effective Rabi frequency of the Raman transition in the experiment was measured to be 104 kHz, which is slightly higher than the 100 kHz assumed for simulation. Additionally, the from the ideal pulse shape may lead to the enhanced oscillations in the experiment, since here the pulses envelope is less smooth (see Figure 27). Furthermore, the off-resonant excitation leads to a degradation of the experimental signal for longer pulse sequences. Despite these differences, the experimental data is in qualitative agreement with the simulations and we can identify a region of efficient adiabatic transfer. We can also compare the experimental data with simulations for the blue sideband transition. As described in Section 2.4, the Rabi frequency for sideband transitions is reduced by the Lamb Dicke factor, which is approximately 0.3 for our system parameters. Therefore, we need a longer pulse length to fulfill the adiabatic criterion and to achieve efficient transfer. As can be seen

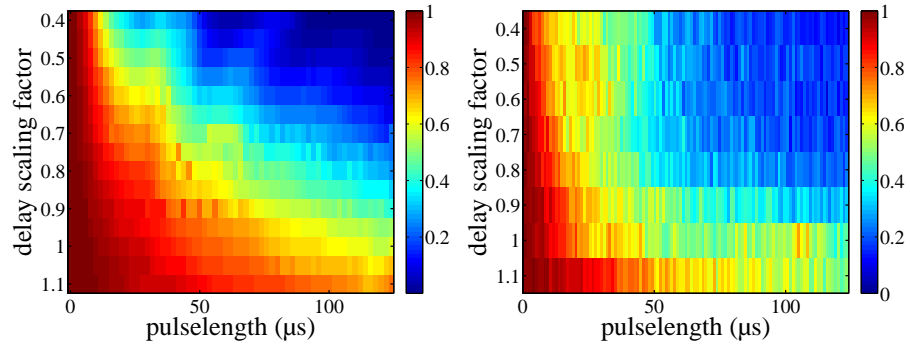


Figure 31: **Simulated transfer probability for different delay scaling factors and pulse length on for BSB transition.** Red corresponds to no and blue to complete transfer. For the simulations and the measurements the ion was initialized in the ground state and the pulse length was scanned for different delay scaling factors according to Equation (62).

in Figure 31, we can again identify a region where we have efficient adiabatic transfer for our given laser power and detuning. For the carrier transition we achieve the best transfer for a delay scaling factor around $s = 0.7$ and pulse length of larger than $50 \mu\text{s}$, whereas for sideband transitions smaller scaling factors and longer pulse length are necessary. For both transitions off-resonant excitation to the excited $^2P_{3/2}$ -state is limiting the final transfer efficiency. But, since we need longer pulse lengths due to the smaller coupling for sideband transitions, while the off-resonant scattering remains unchanged, it has a stronger effect for blue sideband transitions, limiting the transfer efficiency to 85 %.

5.3.2 Motional dependence of the STIRAP transfer

After estimation of the appropriate parameters for the transfer we are now in a position to investigate the motional dependence of the transfer efficiency. This will be the main result of this chapter. Using the simulations we investigated the transfer efficiency depending on the motional state for the lowest 15 trap levels for carrier and sideband transitions. Employing the red sideband transition, we are able to distinguish the ground state population as described in the introduction of this chapter.

In Figure 32 we can see that for the carrier transition the transfer efficiency is reduced for higher motional levels. This is due to the decrease in coupling strength associated with higher motional levels. For the sideband transitions, the transfer becomes more adiabatic at higher motional levels as the coupling strength increases with the motional quantum number. In the experiment, we can not probe each of

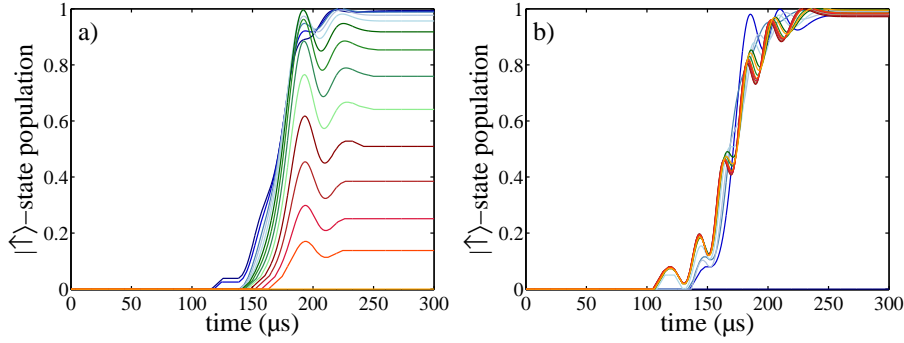


Figure 32: **Simulated transfer probability of the population for the lowest 15 motional levels.** The transfer probability is displayed for a) the carrier and b) the red sideband transition. Fock states are used in the simulations, where dark blue corresponds to the motional ground state and the color gets brighter for higher motional levels and changes from blue to green, to red and finally to yellow for $n=15$.

the motional states individually. Therefore, we experimentally tested the motional dependence of the transfer by investigating the pulse length dependence of the transfer for the ion initialized in the motional ground state and compare it to the efficiency for the ion initialized in a thermal state. As can be seen from Figure 33, the transfer for sideband transitions is slower when the ion is initialized in the motional ground state. This is due to the fact that higher motional states with their associated stronger couplings are involved in the transfer when the ion is initialized in a thermal state. For pulse lengths longer than $100 \mu\text{s}$, the two curves for the transfer on the blue sideband overlap with each other. This means that if the pulse lengths of the STIRAP sequence are chosen long enough, we can transfer the population independent of the motional state of the ion. This is exactly what we need for the spectroscopy experiment.

Additionally, the transfer efficiency for a red sideband transition is plotted in Figure 33 for the ion initialized in a thermal state of motion. If we assume that for a pulse length of $120 \mu\text{s}$ the transfer is complete, we can calculate the mean value of the transferred population for a pulse length between $120 \mu\text{s}$ and $150 \mu\text{s}$. For the measurement, the difference in transferred population for the blue and red sideband is on the order of 0.08 ± 0.01 . This corresponds to a ground state population of a thermal distribution with a temperature of 1.3 ± 0.2 times the Doppler cooling temperature in agreement with temperatures measured for ion trap experiments [112].

With this investigation we showed that we can detect the residual ground state population efficiently using a red sideband STIRAP pulse. Additionally, the detection efficiency does not depend on the specific motional distribution as long as the transfer for the ground state is

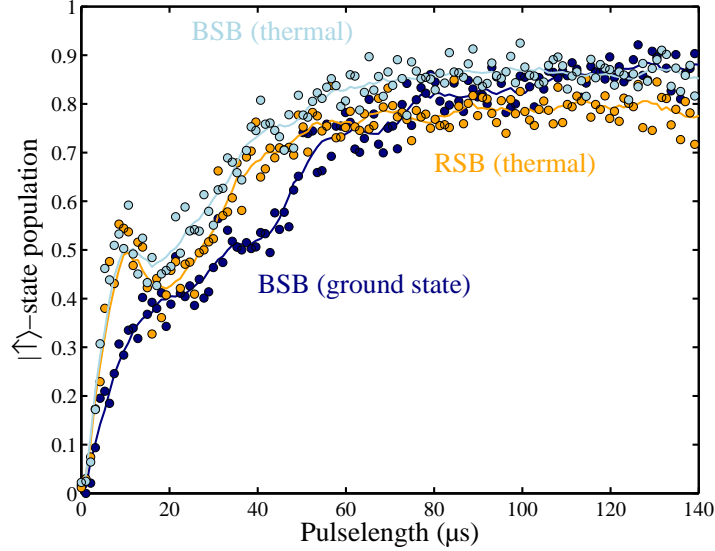


Figure 33: **Scan of the transfer time for a STIRAP pulse sequence** The ion was initialized in the ground state (dark blue) and a thermal state (light blue) for a blue sideband transition. Additionally the transfer is displayed for a red sideband pulse, where the ion was initialized in a thermal state (orange). The plotted line is a moving average of the data and is added to guide the eye. For clarity the errorbars are omitted in the graph.

complete. In contrast, the π pulse technique suffers from incomplete state transfer for any pulse length as shown in the next section.

5.3.3 Comparison of the transfer efficiency for STIRAP and Rabi oscillations

After showing the feasibility of motional state independent transfer we can compare the transfer efficiency of the **STIRAP** process with that of using Rabi oscillations for a Doppler cooled ion. For the comparison, we consider the total duration of the transfer process and therefore need to translate the full width at half maximum (**FWHM**) for the **STIRAP** pulses to the total duration of the transfer. We considered only the relevant part of the pulses and cut the parts where only one laser is switched on at the beginning and the end of the sequence. This leads to an effective transfer time of $t_{\text{trans}} = t_{\text{FWHM}} + s \cdot t_{\text{FWHM}}$ for the **STIRAP** process. Here, we assumed that the power of the Gaussian pulse does not affect the transfer for times longer than t_{FWHM} after the maximum of the Gaussian. In the experiment, we also cut the pulses accordingly, reducing the effective transfer time. Here we can see that the transfer using a Raman Rabi oscillations is faster. After approximately $12 \mu\text{s}$ the maximum transfer efficiency of below 80 % is reached for the blue sideband transition. This transfer is sensitive to the system parameters, especially to variations in Rabi frequency. The

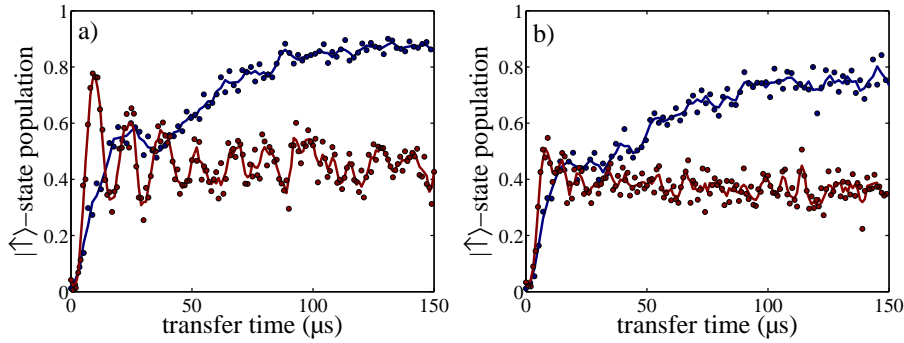


Figure 34: **Comparison Rabi and Stirap transfer for a thermal distributed state.** The transfer probability is displayed for a) the blue sideband and b) the carrier transition. For the measurements the ion was initialized using Doppler cooling. The plotted line is a moving average of the data and is added to guide the eye. Additionally, for clarity the errorbars are omitted in the graph.

STIRAP transfer, however, is slower but reaches a transfer efficiency of higher than 85 % for transfer times on the order of 150 μs . One should mention here, that the transfer using **STIRAP** is limited by off-resonant excitation, which can be circumvented using a larger Raman detuning, whereas the transfer using Rabi oscillations is fundamentally limited by the different couplings between the motional states. Additionally, for the **STIRAP** technique the transfer is robust against variations of the Rabi frequency. On the carrier, the stronger motional state dependence of the Rabi frequency leads to a faster dephasing of the Rabi oscillations, as can be seen in Figure 34 b). Therefore, the transfer efficiency using Raman Rabi oscillations is reduced to 50 % whereas the transfer using the **STIRAP** technique is still on the order of 75 % for our system parameters. Here the transfer efficiency with respect to the blue sideband is reduced since the Rabi frequency has a zero crossing at a motional state of $n = 15$. Population in a range around this state can not be transferred efficiently.

In summary the **STIRAP** technique leads to higher transfer efficiencies for our system parameters (limited by off-resonant excitation) than the transfer based on Raman Rabi oscillations, but the time needed for the transfer is longer. However, the transfer time is not that critical for our experiments since the 150 μs needed for the **STIRAP** process is short compared to the total time of the spectroscopy sequence, which is on the millisecond range, as described in the following chapter.

5.4 DISCUSSION

In this chapter we have investigated the **STIRAP** technique to transfer population between two hyperfine states of a $^{25}\text{Mg}^+$ ion. After the determination of appropriate system parameters used for efficient

population transfer, we explored the dependence of the transfer efficiency on the motional state of the ion. There, we showed that we can transfer the population efficiently even for an ion in a thermally distributed state. Using this result, we presented an efficient way to detect the motional ground state population based on a [STIRAP](#) red sideband pulse. This detection is robust against fluctuations of the Rabi frequencies and does not depend on the specific motional distribution. In contrast, for the transfer using Rabi oscillations, the optimum π time depend on the specific motional distribution, thus hindering the determination of the motional ground state population. Furthermore a separate Raman laser system providing a larger detuning would allow transfer efficiencies approaching 100 % for the [STIRAP](#), making it an appropriate tool to determine the motional ground state population. From this, a temperature can be determined for a motionally excited ion. More elaborate pulse sequences using a combination of [STIRAP](#) red sideband and [RF](#) pulses would even allow the detection of higher motional state populations, enhancing the accuracy of the determined temperature. Furthermore, the technique enables us to perform photon recoil spectroscopy with high detection efficiency, as described in the next chapter.

ISOTOPE SHIFT MEASUREMENTS OF CALCIUM IONS

The precise knowledge of isotope shifts is desirable in different fields of physics ranging from the search for possible changes of fundamental constants in astrophysical investigations [113] to nuclear physics. The precise determination of the mean square nuclear charge radius from optical isotope shift measurements serves as an important complement to the investigation of nuclear properties by means of muonic scattering and x-ray measurements [28, 29]. For example optical isotope shift measurements are used to determine the presence of halo neutrons in ${}^7\text{Li}$ [7] and ${}^9\text{Be}$ [6]. The standard experimental tool to measure isotope shifts of ions is fast ion beam collinear laser spectroscopy, which has achieved uncertainties on the order of a few MHz for typical transition linewidth of tens of MHz. In the last years many new spectroscopy techniques for precision measurements of such broad transitions were developed for trapped ions [114, 38, 115, 116, 117, 118]. These techniques have the potential to reduce the uncertainty of the measured isotopic shift of many different species to below 1 MHz. The techniques presented in [115, 116, 118] are variations of the laser-induced fluorescence technique, where a laser is used to directly measure the detuning dependence of the scattering rate of the atomic transition. Here the sensitivity is limited by poor collection efficiencies and does not reach the sensitivity of the photon recoil spectroscopy technique we present here. In contrast in the technique presented in [117] the loss of coherence of a superposition state due to the scattering of photons on a transition including one of the two involved states is measured. This technique has a high sensitivity, on average the scattering of two photons could be detected, but it relies on the specific level structure of the spectroscopy ion, thus limiting its applicability to a few species. In the cat-state spectroscopy technique [38], where an entangled state is used to amplify the momentum kick that the ion experiences during scattering, the highest sensitivity was achieved by the detection of a single scattering event per experimental cycle. However, in the experiment the authors did not perform an absolute frequency measurement or a systematic shift analysis, whereas the PRS technique has been characterized and used to perform an absolute frequency measurement [114].

Up to now the most accurate isotope shift measurement of trapped ions was performed on trapped Mg^+ ions in an ion chain with a measurement uncertainty of less than 100 kHz [119]. Magnesium provides only two stable naturally abundant even isotopes. This limits

the accuracy of the nuclear constants derived from the measurements [28]. Here we present isotope shift measurements of the ${}^2S_{1/2} \rightarrow {}^2P_{1/2}$ and the ${}^2D_{3/2} \rightarrow {}^2P_{1/2}$ transitions of the stable and natural abundant even Ca^+ isotopes using photon recoil spectroscopy [114]. For the technique, a two-ion crystal consisting of the so called "logic" ion ${}^{25}\text{Mg}^+$ and the investigated Ca^+ isotope is used.

After a brief introduction to the theory of isotope shift, the potential problems and solutions for isotope selective loading of the different Ca^+ ions are presented in Section 6.2. In Section 6.3 the photon recoil spectroscopy technique used to measure the isotopic shift is described. How the technique is extended to enable the measurement of non-closed transitions is discussed in Section 6.4. The results of the isotope shift measurements and a comparison to calculations is presented in Section 6.5. The chapter ends with a summary and outlook in Section 6.7.

Parts of the following results were submitted for publication [120].

6.1 ISOTOPE SHIFT THEORY

The energy difference between two electronic states of an atom depends on the structure and the mass of the nucleus and varies between different isotopes. The difference of the transition frequencies between two different isotopes is called isotope shift. The influence of nuclear properties on atomic spectra was first investigated in the middle of the last century and can be found in the literature, for example in [58, 121, 122, 123]. The following discussion is based on the description in [121].

There are two different effects contributing to the isotopic shift, namely the field and the mass shift. For light atoms the change in mass of the core is the dominant contribution to the isotope shift. In the center of mass system of the atom the sum of the momenta of the nucleus p_{nuc} and the electrons p_i is zero [121]:

$$p_{\text{nuc}} + \sum p_i = 0. \quad (63)$$

The kinetic energy of the system can be calculated as:

$$\frac{p_{\text{nuc}}^2}{2M} + \frac{1}{2m_e} \sum p_i^2 = \frac{1}{2M} \left(\sum p_i \right)^2 + \frac{1}{2m_e} \sum p_i^2 \quad (64)$$

with M as the nuclear and m_e as the electrons mass. Thus, the part of the Hamiltonian concerning the motion of the nucleus can be written as:

$$\mathcal{H}_{\text{nuc}} = \frac{1}{2M} \left(\sum p_i \right)^2. \quad (65)$$

This energy can be understood as the recoil energy due to the finite mass of the nucleus. In the literature the mass shift is divided into two parts [123]:

$$\frac{1}{2M} \left(\sum p_i \right)^2 = \frac{1}{2M} \sum (p_i)^2 + \frac{1}{M} \left(\sum_{i<j} p_i p_j \right), \quad (66)$$

where the first part is called the normal mass shift which is sometimes also called the Bohr reduced mass correction [122, 58] and the second one is called the specific mass shift. The specific mass shift is difficult to calculate since it involves two-body operators of correlated electron momenta as can be seen from Equation (66). We see that the mass shift is proportional to the inverse nuclear mass and if we now compare two different isotopes of mass A and A' , we can express the change of the transition frequency as:

$$\delta\nu_{\text{mass}}^{AA'} = k \left(\frac{1}{A} - \frac{1}{A'} \right) = k \frac{A' - A}{AA'}, \quad (67)$$

where we introduced the mass shift constant $k = k_{\text{nms}} + k_{\text{sms}}$, resulting from the normal k_{nms} and the specific k_{sms} mass shift. The factor containing the inverse masses of the isotopes vanishes quickly with increasing mass and the effect becomes small for ions with large mass numbers. Therefore, in heavy atoms another effect, namely the field shift due to the finite size of the nucleus plays the dominant role. This field shift arises since the core constituents, the protons and the neutrons, order differently when the number of neutrons in the core is changed, leading to a change in the nuclear charge distribution. This results in a change of the binding energies of the electrons penetrating the core and therefore alters the transition frequency. The effect is largest for S states since the wavefunction of other states vanishes for small distances of the electron to the core center ($r \rightarrow 0$). To evaluate the shift we can calculate the change in the electron energy in the true electrostatic potential $\phi(r)$ of the field of the nucleus in comparison to the Coulomb potential $-Ze/4\pi\epsilon_0 r$ [121]:

$$\Delta E = -e \int \left(\phi(r) - \frac{Z}{4\pi\epsilon_0 r} \right) \psi^2(r) dV, \quad (68)$$

where $\psi(r)$ is the electronic wave function and ϵ_0 is the vacuum permittivity. The shape of the core potential can be approximated in a simple model assuming an uniform electronic charge density over the size of the core, leading to a quadratic potential energy (see for example [58]). In this model we can evaluate the integral for an S state and get [121, 58]:

$$\Delta E = \frac{Ze^2}{6\epsilon_0} |\psi(0)|^2 \langle r^2 \rangle. \quad (69)$$

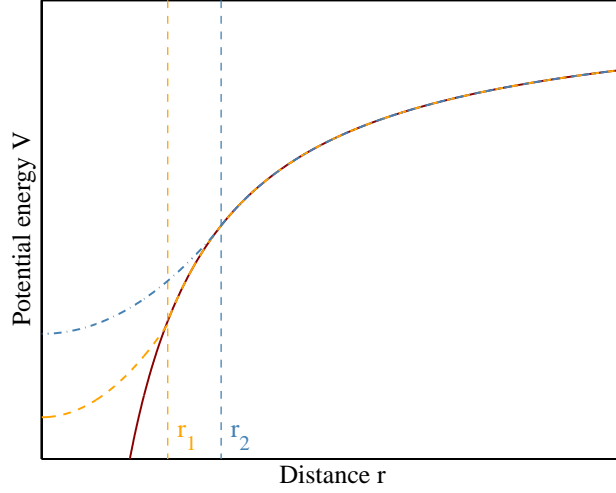


Figure 35: **Modification of the potential energy of the electron due to the non-zero size of the core.** The red line corresponds to a pointlike core. To indicate the effect of the finite size, the potential energy for two different core sizes is displayed: The yellow line corresponds to a smaller core than the blue line. The vertical yellow and blue lines indicate the different nuclear charge radii $r_1 < r_2$.

with $\psi(0)$ as the electronic wave function at $r = 0$ and $\langle r^2 \rangle$ as the mean square nuclear charge radius. It is instructive to plot the modification of the electronic potential, due to the finite size of the core. As indicated in Figure 35 and Equation (69), the field shift increases for large nuclear charge radii. The change of the transition frequency, however, depends on the relative strength of the effect for the two involved energy levels. By introducing the field shift constant F and neglecting higher moments of the nuclear charge distribution we can write [28]:

$$\delta v_{\text{field}}^{AA'} = F \delta \langle r^2 \rangle^{AA'}, \quad (70)$$

and in total the isotope shift can be expressed as:

$$\delta v^{AA'} = F \delta \langle r^2 \rangle^{AA'} + k \frac{A' - A}{AA'}. \quad (71)$$

For two different transitions i and i' it follows that [28]:

$$\delta v_i^{AA'} = \delta v_{i'}^{AA'} \frac{F_i}{F_{i'}} + \frac{A' - A}{AA'} \cdot \left(k_i - k_{i'} \frac{F_i}{F_{i'}} \right), \quad (72)$$

and we can plot the modified isotope shift:

$$m \delta v_i^{AA'} = \delta v_{i'}^{AA'} \frac{AA'}{A' - A}, \quad (73)$$

for two different transitions (i, i') and all pairs of A and A' against each other in a so called King plot [30]. The data for the different pairs A and A' should lie on a straight line with slope $F_i/F_{i'}$ and intercept $k_i - k_{i'} F_i/F_{i'}$. These values can be compared to calculations

and check for consistency of the theoretical models used for the calculations. Additionally, deviations from the linear model could lead to unexpected results such as higher order field shifts or relativistic effects in mass shift.

Furthermore, we can use experimental data of the nuclear charge radius for the analysis. The radius can be measured using x-ray spectroscopy of muonic atoms, where the transitions are strongly affected by the size of the nuclei due to the larger mass of the muon and the resulting high probability of presence of the muon in the core (see [124]), or electron scattering experiments. From Equation (71) it follows that [28]:

$$m\delta v_i^{AA'} = F_i m\delta \langle r_t^2 \rangle^{AA'} + k_i, \quad (74)$$

where we introduced the modified mean square nuclear charge radius:

$$m\delta \langle r_t^2 \rangle^{AA'} = \delta \langle r_t^2 \rangle^{AA'} \frac{AA'}{A' - A} \quad (75)$$

The isotope shift can be plotted against the nuclear charge radius (corresponding to $F_i = 1$ and $k_i = 0$) and from the slope and the intercept the field and the mass shift constant can be extracted directly.

In a more elaborate analysis, we can combine the two techniques and perform a multidimensional King plot analysis [125], where we use the isotope shifts of different transitions in combination with measured changes in mean square nuclear charge radii. To account for all experimental uncertainties we estimate the desired nuclear parameters and their uncertainties from a Monte-Carlo type analysis, where we minimize the squared distances of the isotope shifts to the fitted line and simultaneously optimize the position of the $m\delta \langle r_m^2 \rangle^{AA'}$ on it for Gaussian distributed input parameters according to:

$$\begin{aligned} \chi^2 = & \sum_{AA'} \left(\frac{m\delta v_i^{AA'} - (F_1 m\delta \langle r_t^2 \rangle^{AA'} + k_1)}{\sigma_{m\delta v_i^{AA'}}} \right)^2 \\ & + \sum_{AA'} \left(\frac{m\delta v_{i'}^{AA'} - (F_2 m\delta \langle r_t^2 \rangle^{AA'} + k_2)}{\sigma_{m\delta v_{i'}^{AA'}}} \right)^2 \\ & + \sum_{AA'} \left(\frac{m\delta \langle r_m^2 \rangle^{AA'} - m\delta \langle r_t^2 \rangle^{AA'}}{\sigma_{m\delta \langle r_m^2 \rangle^{AA'}}} \right)^2. \end{aligned} \quad (76)$$

with respect to the parameters $F_1, F_2, k_1, k_2, m\delta \langle r_t^2 \rangle^{40,42}, m\delta \langle r_t^2 \rangle^{40,44}$ and $m\delta \langle r_t^2 \rangle^{40,48}$. The $\sigma^{AA'}$ are the corresponding errors of the measured modified isotope shifts and charge radii. The analysis enables, although seeded with experimental modified relative mean square nuclear charge radii $m\delta \langle r_t^2 \rangle^{AA'}$, the determination of more accurate values for these changes, using precise measurements of the isotope

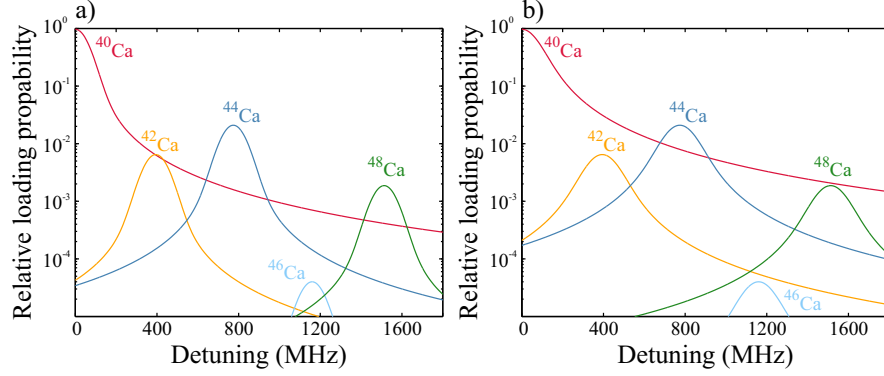


Figure 36: **Estimated relative ionization probabilities.** The relative ionization probability of the isotopes were referenced to the most abundant ^{40}Ca isotope. For the estimation Doppler and saturation broadening were considered with saturation parameter a) $s_0 = 0.1$ and b) $s_0 = 10$.

shift. In other words, we restrict the values for $m\delta \langle r_t^2 \rangle^{\Lambda, \Lambda'}$ by accurately measured isotope shifts using the linear model in Equation (74). A variation of this technique was used in [120] to extract the nuclear parameters, providing almost the same values as the ones given below. To provide more accurate isotope shift data, we performed precision measurements on the isotope shift of Ca^+ ions using a new spectroscopy technique, described in Section 6.3 and Section 6.4.

6.2 ISOTOPE-SELECTIVE LOADING

For the precision isotope shift measurements we loaded consecutively different two-ion crystals consisting of the $^{25}\text{Mg}^+$ logic ion and the different Ca^+ isotopes as the spectroscopy ion. This was accomplished via two-step photoionizing an atom beam from a heated steel tube filled with a powder of the corresponding material as described in Section 3.2. Isotope-selective loading of the different Ca^+ isotopes was achieved by tuning the frequency of a laser in resonance with the $^1\text{S}_0 \rightarrow ^1\text{P}_1$ transition of neutral Ca, taking into account the isotopic shift [64]. The transition frequencies of the different isotopes differ by approximately 200 MHz per mass unit. This shift is much larger than the linewidth of the excitation laser, i.e. the frequency doubled ECDL. In view of the natural linewidth of the transition of 35,4 MHz it allows for isotope-selective loading as long as additional broadening mechanisms of the atomic resonance line are not too large. For loading we used a calcium powder with natural abundances of the different isotopes. Due to the low natural abundance of some of the isotopes (as can be seen in Table 1) the relative loading rate of these isotopes is expected to be small. We estimated the relative loading rates of the different calcium isotopes with respect to ^{40}Ca from the

mass number	Natural abundance	$f_{IS,422}$ (MHz)	$f_{theory,ip}$ (MHz)
40	96.900%	0	1.922
42	0.647%	394	1.889
44	2.090%	774	1.857
46	0.004%	1160	1.826
48	0.187%	1513	1.796

Table 1: **Important properties for loading different isotopes of calcium.**

Natural abundance, isotope shift of the $^1S_0 \rightarrow ^1P_1$ transition of the neutral Ca and normal mode frequencies calculated according to Equation (10) for the different isotopes considering a $^{25}\text{Mg}^+$ single ion trap frequency of 2.215 MHz.

excitation probability of the $^1S_0 \rightarrow ^1P_1$ transition in neutral calcium multiplied by the natural abundance of the corresponding isotope, as shown in Figure 36 for two laser intensities described by the saturation parameter:

$$s_0 = I/I_{\text{sat}} \quad (77)$$

where I is the intensity in the laser beam and I_{sat} is the saturation intensity of the transition given by [58]:

$$I_{\text{sat}} = \frac{\pi \hbar c}{3 \lambda^3 \tau} \quad (78)$$

Here $\tau = 1/\Gamma$ is the radiative lifetime and λ the wavelength of the transition, c is the speed of light and \hbar is Planck's constant. For the $^1S_0 \rightarrow ^1P_1$ transition in neutral Ca, the saturation intensity is on the order of $30 \mu\text{W}/\text{mm}^2$ and can easily be saturated. In figure Figure 36 we see that for a certain detuning range the probability to load $^{42}\text{Ca}^+$, $^{44}\text{Ca}^+$ and $^{48}\text{Ca}^+$ ions is higher than for $^{40}\text{Ca}^+$ as long as the laser power is low. In the estimation Doppler and saturation broadening were considered. The effect of transit time broadening was estimated to be on the order of 1 MHz and thus was neglected. The oven temperature was assumed to be around 500°C . We considered an atomic beam axis aligned perpendicular to the excitation laser. The velocity of the atoms parallel to the excitation laser was estimated considering an aperture of 1 mm at a distance of 4 mm from the oven design. Only the lower part of the oven is heated and the upper part serves as aperture. Furthermore, the relative loading rate was estimated for two different laser intensities with a saturation parameter of $s_0 = I/I_{\text{sat}} = 0.1$ and $s_0 = 10$. In the experiment we were able to reproducibly load single $^{40}\text{Ca}^+$, $^{42}\text{Ca}^+$, $^{44}\text{Ca}^+$ and $^{48}\text{Ca}^+$ ions by careful adjustment of the laser power, thus avoiding saturation broaden the transition of the Ca atoms. However, due to the very low abundance of $^{48}\text{Ca}^+$ and limited control of the laser frequency,

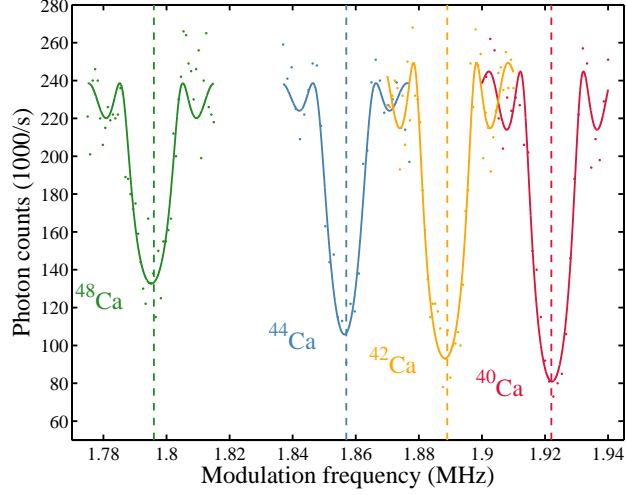


Figure 37: **Mass spectroscopy signal for the different isotopes** Measured photon counts for different modulation frequencies applied to the endcaps of the ion trap for the two ion crystals containing the different Ca^+ isotopes; red $^{40}\text{Ca}^+$, orange $^{42}\text{Ca}^+$, blue $^{44}\text{Ca}^+$, green $^{48}\text{Ca}^+$. A fit to the data gives the normal mode frequency of the in phase mode of the two ion crystal. Dashed lines: expected trap frequencies according to Table 1.

the loading rate of this isotope was only small, on the order of 1 ion per 20 h.

After loading, the different isotopes can be distinguished by the motional normal mode frequencies of the two ion crystal in the trapping potential given by Equation (10). The calculated frequencies for the two axial modes in the trap are displayed in Table 1 together with the isotope abundances and the isotope shift of the $^1S_0 \rightarrow ^1P_1$ transition of the neutral Ca atom taken from [64].

Experimentally, we determined the normal mode frequencies of the two-ion crystal by adding an AC-component with variable frequency to the voltage between the endcaps of the ion trap [126]. As soon as its frequency is resonant with the normal mode frequency, the ions experienced a Doppler shift due to the increase in motional energy. This leads to a reduction in fluorescence of the $^{25}\text{Mg}^+$ ion, which is measured using a photo multiplier tube. As shown in [67], the dependence of the scattering rate on the AC frequency $\delta\omega$ can be calculated from the change in the ions' velocity, due to the displacement of the ions' motional state by the additional electrical field. This field accelerates the oscillation velocity in the trap and, depending on the modulation frequency, the fluorescence due to the Doppler shift can be calculated as:

$$\Gamma_{\text{sc}} = \frac{\Gamma}{2} \frac{s}{1 + s^2} \frac{1}{\sqrt{1 + [b \cdot \text{sinc}(\delta\omega_t/2)]^2}}, \quad (79)$$

where s is the saturation parameter, Γ is the resonant scattering rate of the transition and the parameter b takes the form:

$$b = \frac{4k}{\Gamma\sqrt{1+s^2}} \sqrt{\frac{\hbar\omega_T}{2m}} \Omega_d t. \quad (80)$$

Here ω_T is the trap frequency, k is the magnitude of the wavevector and Ω_d is the displacement strength. This parameter together with the center frequency, the amplitude, and an additional offset serve as the fit parameters for the scans of the modulation frequency shown in Figure 37. The modulation frequency was scanned for different two-ion crystals containing the different Ca isotopes while the fluorescence was measured using the PMT. The modulation frequency is tuned to be resonant with the in-phase mode of the two-ion crystals. A fit to Equation (10) leads to the center frequencies of 1.9221(3) MHz, 1.8883(3) MHz, 1.8564(5) MHz, and 1.7952(5) MHz for ^{40}Ca , ^{42}Ca , ^{44}Ca and ^{48}Ca , respectively. Good agreement is found with the ones calculated from Equation (10), which are listed in Table 1.

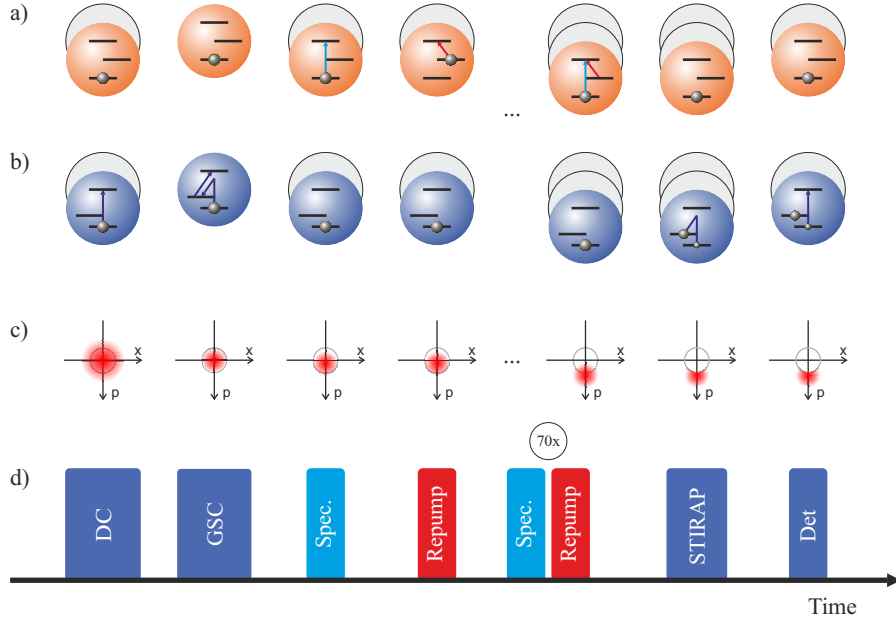


Figure 38: **Photon recoil spectroscopy sequence.** a) Motion and simplified electronic level structure of the spectroscopy ion including the $^2S_{1/2}$, $^2P_{1/2}$ and $^2D_{3/2}$ level. b) Motion and simplified level structure of the logic ion, including the two qubit states and the excited $^2P_{3/2}$ state. c) Wigner function of the motional state of the in-phase mode of the two-ion crystal. d) Experimental sequence. The abbreviations stand for: DC: Doppler cooling; GSC: Ground state cooling; Spec: Spectroscopy laser; Det: State detection. A more detailed description is given in the text.

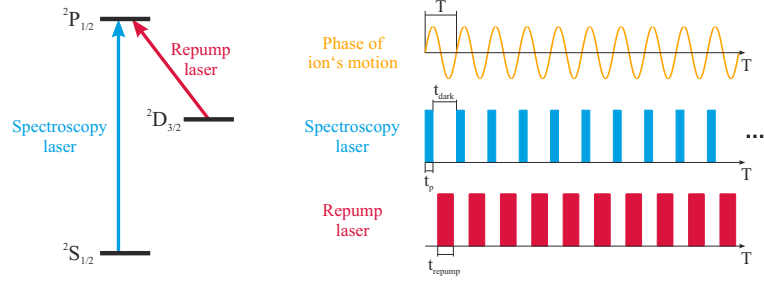


Figure 39: **Pulse timing for photon recoil spectroscopy** The time $T = 1/\nu_t = 1/1.92$ MHz is used to synchronize the pulses to the ion's motion. The pulse length was chosen to be $t_p \approx 130$ ns which corresponds to a duty cycle of $d = 0.25$. The repump time $t_{\text{repump}} \approx 200$ ns was chosen so that the repump pulses do not overlap with the spectroscopy pulses.

6.3 PHOTON RECOIL SPECTROSCOPY

After loading the two-ion crystals, isotope shift measurements for the ${}^2S_{1/2} \rightarrow {}^2P_{1/2}$ transition of the different Ca^+ isotopes were performed using the photon recoil spectroscopy (PRS) technique we implemented and characterized in our setup [114]. The experimental sequence of the technique is displayed in Figure 38. After Doppler cooling, we further cool the axial motional modes of the two ion crystal via sideband cooling using a Raman beam configuration coupling to the ${}^2S_{1/2} \rightarrow {}^2P_{3/2}$ transition at 280 nm in ${}^{25}\text{Mg}^+$ [66, 114]. After preparing the motional ground state of the two-ion crystal we apply the spectroscopy laser. The recoil, imprinted onto the ion during photon absorption, excites the motion of the two-ion crystal. This motional excitation can be enhanced using pulsed laser excitation, where the laser pulse repetition is matched to the motion of the two-ion crystal [127, 38, 126]. The correct timing of the laser pulses with respect to the phase of the ions' motion (see Figure 39) restricts the absorption to a period of time, when the ion is moving along the laser direction. Thus, the photon and ion momentum are in phase and the ions' motion is efficiently enhanced. Since the motion of the ion is seeded by the first absorption, matching the pulse repetition rate to the normal mode frequency assures the synchronization of the pulses with the phase of the ions' motion. The excitation is illustrated in Figure 40 a), where the phase space representation of the motional state is displayed. The phase matching assures excitation along the momentum axis and efficiently reduces the overlap of the final state with the ground state. It can be shown that this excitation is equivalent to a displacement of the motional state in phase space during photon absorption [67]. After excitation, the ${}^2P_{1/2}$ state decays spontaneously to the electronic ground state at an arbitrary motional phase and along a random direction. Therefore, this process leads to a diffusive part similar to the behavior in Figure 40 b), where the

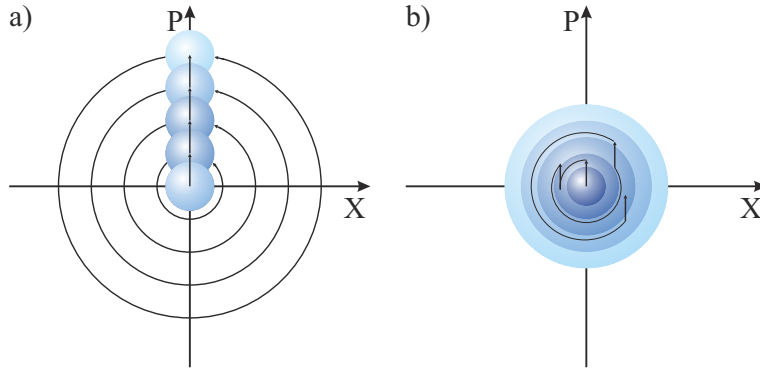


Figure 40: **Excitation during photon recoil spectroscopy.** a) The motional excitation is coherent if short pulses synchronized to the trap frequency are used for spectroscopy. b) The excitation is diffusive in phase space if the excitation is continuous.

motional state of the ions becomes larger in phase space. This part increases the motion of the ion as well but is much less efficient than the coherent part. Furthermore, the non zero pulse length of the spectroscopy pulse leads to a reduced efficiency in the excitation of the motion.

In the experiment the spectroscopy laser is applied in short pulses with a duration of 125 ns and a repetition frequency matched with the normal mode frequency of the in-phase mode of the two-ion crystal (column 4 of Table 1). The duty cycle of the spectroscopy pulse was $d = \frac{t_p}{T} = 0.25$. During the dark time $t_{\text{dark}} = T - t_p$ between two excitation pulses, the repump laser at 866 nm is applied in order to prevent populating the metastable $^2D_{3/2}$ state. Altogether the spectroscopy/repump cycles are repeated 70 times to provide the maximum motional excitation possible without onset of saturation for the chosen experimental parameters. The motional excitation is then measured using a red sideband **STIRAP** pulse (Chapter 5) combined with the subsequent determination of the $^{25}\text{Mg}^+$ internal state. Further details of the technique can be found in [67, 114].

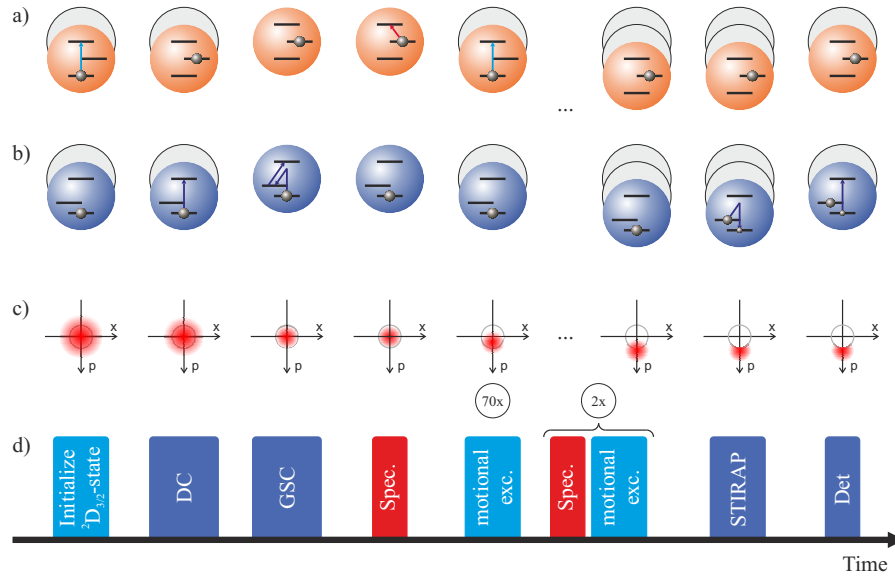


Figure 41: **Photon recoil spectroscopy sequence for non-closed transitions.** a) Motion and simplified electronic level structure of the spectroscopy ion including the $^2S_{1/2}$, $^2P_{1/2}$ and $^2D_{3/2}$ level. b) Motion and simplified level structure of the logic ion, including the two qubit states and the excited $^2P_{3/2}$ state. c) Wigner function of the motional state of the in-phase mode of the two-ion crystal. d) Experimental sequence. The abbreviations stand for: DC: Doppler cooling; GSC: Ground state cooling; Spec: Spectroscopy laser; Det: State detection. A more detailed description is given in the text.

6.4 EXTENSION OF THE PHOTON RECOIL SPECTROSCOPY TECHNIQUE TO NON-CLOSED TRANSITIONS

Additionally to the isotope shift of the $^2S_{1/2} \rightarrow ^2P_{1/2}$ transition, we measured the isotope shifts of the $^2D_{3/2} \rightarrow ^2P_{1/2}$ transition in Ca^+ . Here, the $^2P_{1/2}$ state decays dominantly to the $S_{1/2}$ ground state, from where the ion can not be excited with the spectroscopy laser. We adapted the experimental sequence for PRS as shown in Figure 41.

During initialization the Ca^+ ion is prepared in the $^2D_{3/2}$ state by optical pumping using the laser resonant with the $^2S_{1/2} \rightarrow ^2P_{1/2}$ transition. After ground state cooling, the spectroscopy laser driving the $^2D_{3/2} \rightarrow ^2P_{1/2}$ transition is applied and if it was resonant with the transition, it pumped the ion into the $^2S_{1/2}$ state with high probability (>93 % assuming only one scattered photon). Afterwards, a laser resonant with the $^2S_{1/2} \rightarrow ^2P_{1/2}$ transition (drive laser) is applied in a pulsed fashion with a pulse length of 125 ns synchronized to the ions' motion (see Figure 42). The $^2P_{1/2}$ state decays with a branching ratio of 1 : 14.5 [128] into the $^2D_{3/2}$ state and the $^2S_{1/2}$ state, respectively. Therefore, after 70 drive laser pulses, the ion was most probably in the $^2D_{3/2}$ state. After a short wait time t_{wait} , we apply the sequence of spectroscopy and drive laser again and thus

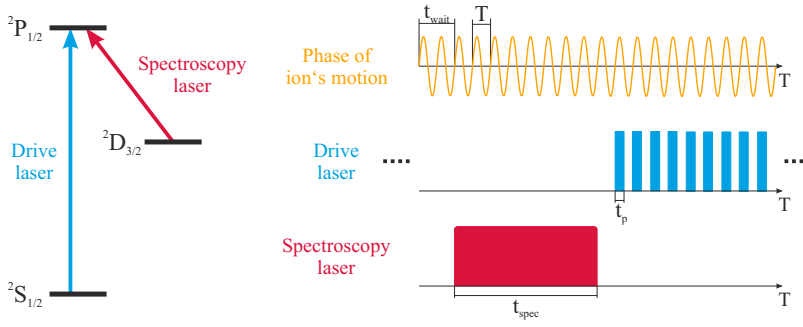


Figure 42: **Pulse timing for photon recoil spectroscopy of non-closed transitions.** The spectroscopy pulse length was chosen to be $t_{\text{spec}} \approx 4 \mu\text{s}$ to assure the depletion of the meta stable $^2D_{3/2}$ state when the laser is applied on resonance. The time $T = 1/\nu_t = 1/1.92 \text{ MHz}$ between consecutive drive laser pulses assures synchronization to the ion's motion and the pulse length was chosen to be $t_p \approx 130 \text{ ns}$ which corresponds to a duty cycle of $d = 0.25$. Additionally, a wait time was introduced in between two spectroscopy/excitation cycles for matching the phase of the ion's motion to the drive laser frequency of consecutive excitation pulse trains.

enhance the spectroscopy signal in form of motional excitation. The consecutive pulse trains from the drive laser are timed with respect to the trap frequency to assure coherent enhancement of the motional excitation. After three of these spectroscopy/excitation sequences the maximum possible excitation without onset of saturation effects is reached in our experiment. The pulse timing and the laser couplings are illustrated in Figure 42.

6.4.1 Measurement of the transition frequencies

For the isotope shift measurements described in Section 6.5, we measured the transition frequencies of the different isotopes using the techniques described in the two preceding sections. Details of the photon recoil spectroscopy technique to measure the $^2S_{1/2} \rightarrow ^2P_{1/2}$ transition are found in [67, 114]. There, we performed an absolute frequency measurement of the $^2S_{1/2} \rightarrow ^2P_{1/2}$ transition in $^{40}\text{Ca}^+$ with an uncertainty of 88 kHz, of which 78 kHz result from systematic and 42 kHz from statistical uncertainties. This means that we resolve the line center of the transition to $1/300$ of its observed linewidth. Furtheron, we showed that we can achieve a signal to noise ratio of one by absorbing 9.5(1.2) photons during one experimental cycle, which enables spectroscopy of non-closed transitions or transitions with an intrinsically low fluorescence rate. This is the case for example in molecular, highly charged, and complex metal ions, and the $^2D_{3/2} \rightarrow ^2P_{1/2}$ transition in Ca^+ .

In the following experimental results of the spectroscopy performed

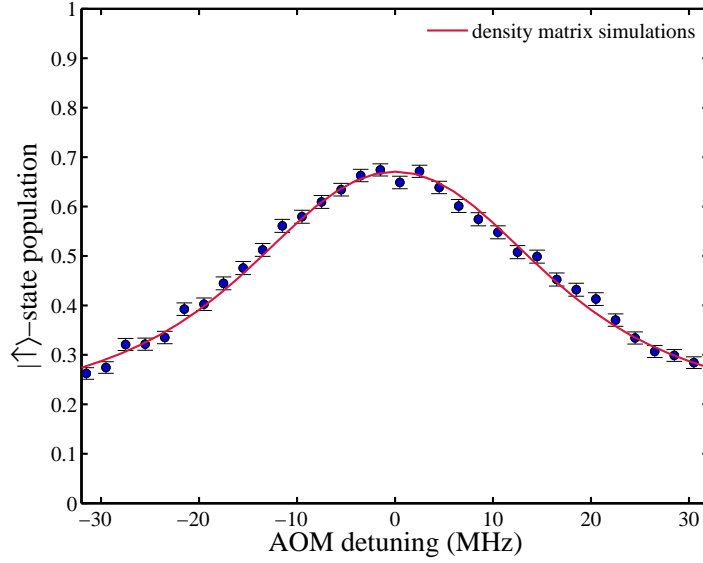


Figure 43: **Resonance line scan.** The displayed curve is the average of eight single frequency scans of the $^2D_{3/2} \rightarrow ^2P_{1/2}$ transition measured on $^{40}\text{Ca}^+$. The red line is the result of a density matrix simulation of the 8 level system (see Figure 9) and has been adjusted in amplitude by a factor of 0.89 and an offset of 0.16 to account for experimental imperfections.

on the $^2D_{3/2} \rightarrow ^2P_{1/2}$ transition are presented. Figure 43 shows a frequency scan across the $^2D_{3/2} \rightarrow ^2P_{1/2}$ transition of $^{40}\text{Ca}^+$. In the figure, the red line is the result of an 8-level (see Figure 9) density matrix simulation considering the dynamics according to the sequence shown in Figure 41 and corrected in amplitude by a factor of 0.89 and an offset of 0.16 taking into account experimental imperfections. The reduced amplitude results from the limited *STIRAP* efficiency and is in agreement with the results presented in Section 5.3, where the transfer was shown to be limited by off-resonant excitation. The additional offset was attributed to state initialization errors and incomplete ground state cooling. This could be confirmed in a measurement where the spectroscopy laser was applied far off-resonant. The correction factors are taken from a least square analysis comparing the measured with the simulated data. In the analysis the Rabi frequency of the spectroscopy laser is used as an additional fit parameter and was extracted to be $2(1)$ MHz. Additionally, the extracted linewidth of 34 MHz is in agreement with the natural linewidth of the transition, broadened due to Zeeman broadening in the bias magnetic field necessary for ground state cooling of the $^{25}\text{Mg}^+$ logic ion. For the spectroscopy sequence described in Section 6.4, not only the timing of the pulses in one pulse train is important, but the phase of the laser pulse repetition of all drive laser pulses need to be matched with the phase of the ion's oscillation in the trap. If the time between two pulse trains is not optimized the excitation can even be reduced.

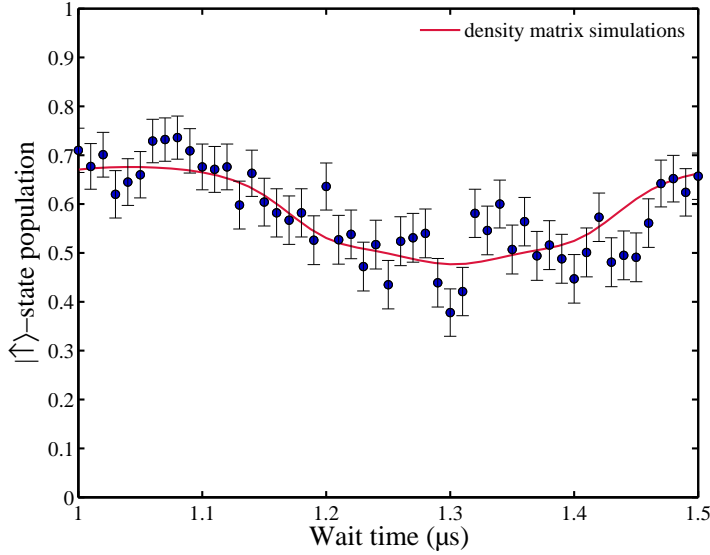


Figure 44: **Wait time dependence of the spectroscopy signal.** The red line is the result of density matrix simulations with the same parameters as used in the experiment.

For example if two pulse trains are applied with a relative phase of 180° with respect to the motion of the ions, the photon and ion momentum are 180° out of phase, resulting in motional de-excitation. This leads to a cancellation of the coherent part of the motional excitation leaving only the diffusive part for the signal generation. To optimize the over-all excitation effect we introduced a wait time between two consecutive spectroscopy/motional excitation procedures (see Figure 42), i.e. a well-defined difference between the repetition phases of individual pulse trains. Figure 44 shows its effect on the $|\uparrow\rangle$ state population after the complete spectroscopic sequence. The red line in Figure 44 is the result of density matrix simulations and is in good agreement with the data. The relatively high remaining signal for a wait time of $1.3 \mu\text{s}$, corresponding to a 180° phase shift between consecutive pulse trains with respect to the ions' motion, results from the odd number of repetitions of the sequence. For this case the coherent part of the first two of the pulse trains cancel, but the third pulse train excites the motion again. For the isotope shift measurements we optimized the wait time to yield the maximum signal to noise ratio.

6.5 EXPERIMENTAL RESULTS

After the discussion of the techniques used to perform the measurements, we will now present their application determining the isotope shift of Ca^+ isotopes. We performed the measurements on different isotopes in an interleaved fashion to minimize systematic errors, as explained in the following. We first determined the atomic transition

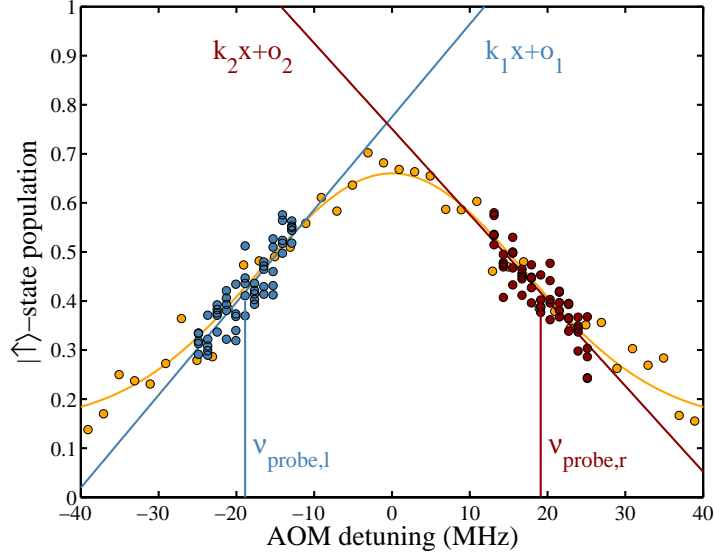


Figure 45: **Determination of the frequency discriminant** The frequency discriminant D is determined from the slopes k_1 , k_2 of the linear fits to the measured data ± 6 MHz around the probe frequencies at the **FWHM** of the resonance curve. As an example, the measurements used to determine the frequency discriminant for the $^2D_{3/2} \rightarrow ^2P_{1/2}$ transition of ^{40}Ca are shown. Error bars are omitted for clarity.

frequency of ^{40}Ca as a reference. Afterwards, we loaded a new two ion crystal containing the logic ion and the calcium isotope under investigation and measured its resonance frequency. After this measurement we reloaded again and determined the transition frequency of another ^{40}Ca reference ion. During the measurements the spectroscopy laser frequency was counted using the frequency comb, as described in Section 3.4. This way we are able to check for possible systematic effects that may affect the measurements on long time scales.

For fast data acquisition we applied the two point sampling technique described in detail in [67, 114]. In brief, the population at half maximum below (left) and above (right) the resonance line was measured and the difference was used to correct the center frequency of the two probing frequencies $\nu_{\text{probe}} = (\nu_{\text{probe,r}} + \nu_{\text{probe,l}}) / 2$ for the next scan using a digital proportional-integral control loop. The population difference δp in combination with the experimentally determined slope at this position, the so called frequency discriminant D , was used in the post evaluation to derive the center frequency of the atomic transition, according to:

$$\nu = \nu_{\text{probe}} - D\delta p, \quad (81)$$

The frequency discriminant D was measured on each measurement day scanning the laser by ± 6 MHz across both half-width points of

the resonance, as shown in Figure 45. From such measurements of the slope we determined the frequency discriminant according to:

$$D = \frac{1}{|k_1| + |k_2|}, \quad (82)$$

where k_1 and k_2 are the left and the right slopes, respectively. The uncertainty of a single frequency measurement can be calculated using the error propagation law, and is given by:

$$\sigma_\nu = \sqrt{(D\sigma_{\delta p})^2 + (\delta p\sigma_D)^2}, \quad (83)$$

where $\sigma_{\delta p}$ and σ_D are the measurement uncertainties of the population and the frequency discriminant, respectively. For each transition frequency we averaged over approximately 100 single frequency measurements. These consisted of 5 measurements on each side of the resonance taken in a random order. Each of the five measurements consisted of 250 cycles of the experimental sequence to derive the state of the ion after spectroscopy. The transition frequency was then calculated as the mean of the single frequency measurements weighted by the measurement uncertainty, calculated from eq. (83). After averaging, the isotope shift $\delta\nu^{AA'}$ was calculated as the difference of the two measured transition frequencies $\delta\nu^A$ and $\delta\nu^{A'}$:

$$\delta\nu^{AA'} = \delta\nu^{A'} - \delta\nu^A \quad (84)$$

The frequency uncertainty of the averaged frequency measurement is given by the standard deviation of the mean and the statistical error of the isotope shift results from the error propagation law of the two measured transition frequencies:

$$\delta\nu_{IS} = \sqrt{(\nu_A\delta\nu_{A'})^2 + (\nu_{A'}\delta\nu_A)^2} \quad (85)$$

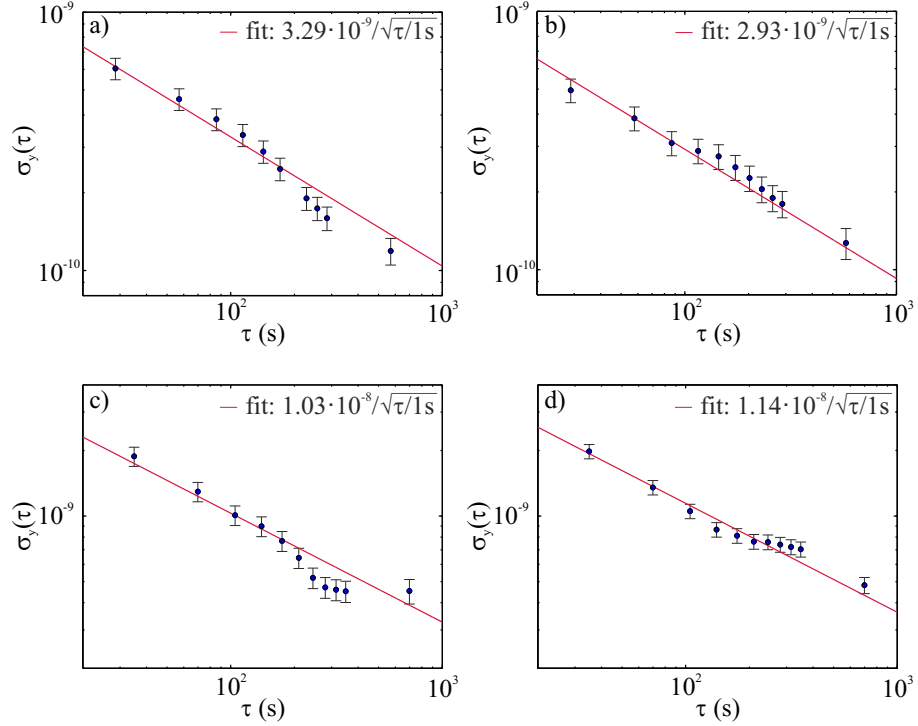


Figure 46: **Overlapped Allan deviation.** Overlapped Allan deviation of the measurement of the ${}^2S_{1/2} \rightarrow {}^2P_{1/2}$ transition for (a) ${}^{40}\text{Ca}$ and (b) ${}^{48}\text{Ca}$ and for the ${}^2D_{3/2} \rightarrow {}^2P_{1/2}$ transitions for (c) ${}^{40}\text{Ca}$ and (d) ${}^{48}\text{Ca}$

We investigated the statistical properties of the frequency measurements by plotting the overlapped Allan deviation for each measurement. There was no sign of drifts or other unknown systematic effects for the measurements we performed. As an example, the overlapped Allan deviation for the measurement of the ${}^2S_{1/2} \rightarrow {}^2P_{1/2}$ and ${}^2D_{3/2} \rightarrow {}^2P_{1/2}$ transition for ${}^{40}\text{Ca}^+$ and ${}^{48}\text{Ca}^+$ is shown in Figure 46.

6.5.1 Systematic effects

Additionally to the statistical uncertainty, there can be systematic effects that shift the measured frequency and need to be considered. Since the isotope shift measurements were performed interleaved, changes of the magnetic field or the laser power and the resulting Stark and Zeeman shifts would be detectable in the two data sets of the ${}^{40}\text{Ca}$ reference measurements taken at the beginning and the end of each measurement day. No such shifts were detected for the performed measurements of the different isotopes at the level of the statistical uncertainty.

This is also the case for the shift caused by the limited bandwidth of the AOM creating the short pulses discussed in [114]. The cen-

effect	${}^2S_{1/2}$ - ${}^2P_{1/2}$	${}^2D_{3/2}$ - ${}^2P_{1/2}$	removed
Stark shift	< 1	< 1	y
Zeeman shift	< 1	< 1	y
AOM shift	< 1	< 1	y
laser calibration	< 1	< 1	y
lineshape	≈ 10	< 1	n
2nd order Doppler	< 1	< 1	y
RF Stark shift	< 1	< 1	y

Table 2: **Systematic shifts.** All shifts are given in kHz. In column 2 and 3 systematic shifts for the two transitions are displayed. The third column shows if the shift is removed, due to the interleaved fashion of the measurement (y: yes; n:no). More details are given in the text.

ter frequency of the 8 MHz broad spectroscopy laser (resulting from the 125 ns short pulses) is shifted due to the frequency-dependent transmission profile of the acousto optical modulator. We confirmed that this shift does not change during the day by interferometrically measuring the spectrum of the beat-note between the first and zeroth diffraction order output beams of the AOM before and after measuring the isotope shift. For the measurement of the ${}^2D_{3/2} \rightarrow {}^2P_{1/2}$ transition this effect is orders of magnitude smaller than in the photon recoil spectroscopy scheme, since the pulses resonant with the measured transition in this scheme are 4 μ s long, reducing the spectral width of the envelope to 250 kHz.

An effect inherent to the photon recoil spectroscopy technique is the detuning-dependent Doppler shift as described in [114]. This shift is present for the ${}^2S_{1/2} \rightarrow {}^2P_{1/2}$ transition and it differs for the different isotopes due to the change in the normal mode frequency arising from the mass difference. The shift was calculated using the simple model derived in [114] and is smaller than 10 kHz for the different isotopes. The uncertainty of these values is on the order of a kHz and can be neglected with respect to the statistical uncertainty on the order of 100 kHz of our measurements. The measured isotope shifts were corrected by the calculated values of the shift. For the measurement of the ${}^2D_{3/2} \rightarrow {}^2P_{1/2}$ transition this shift is expected to be much smaller, since the motional excitation takes place on the ${}^2S_{1/2} \rightarrow {}^2P_{1/2}$ transition. Therefore, the influence of the spectroscopy laser on the motion of the ion is small. Density matrix simulations of the line profile show that the effect for the parameters used in the experiment is below 1 kHz and is therefore negligible with respect to the statistical uncertainty.

Another effect that may shift the measured frequency is the frequency stability of the spectroscopy lasers. As described in Section 3.5 the uncertainty of the laser lock and the laser linewidth are orders of magni-

tude smaller than the frequency uncertainty required here and thus can be neglected for the analysis.

Another effect we investigated was the effect of excess micromotion and the resulting second order Doppler and Stark shifts. These shifts are estimated in [67] for our system to be below 1 Hz and are even reduced due to the differential measurement. Therefore they have no influence on the measurement uncertainty. The resulting isotopic shifts with the corresponding uncertainties are listed in Table 3. For comparison, the previously most accurate measurements of the isotope shifts are given.

	$\delta\nu_{397}^{AA'}$	$\delta\nu_{397}^{AA'}$	$\delta\nu_{866}^{AA'}$	$\delta\nu_{866}^{AA'}$
A'	this work	[32]	this work	[31]
42	425.706(94)	425(10)	-2349.974(99)	-2353.4(2.8)
44	849.534(74)	842(9)	-4498.883(80)	-4501.8(3.5)
48	1705.389(60)	1696(12)	-8297.769(81)	-8301.3(6.2)

Table 3: **Measured isotope shifts of the two transitions.** All shifts are given in MHz and are referenced to the transitions in $A = {}^{40}\text{Ca}$. For comparison previous measurements are provided in column 2 ([32]) and 4 ([31]).

6.6 KING PLOT ANALYSIS OF THE ISOTOPE SHIFT

We performed the three dimensional King plot analysis described in Section 6.1. The measured isotope shifts of the two transitions and the change of the mean square nuclear charge radius taken from [129] were used. First, we illustrate the improved accuracy of the measurements by plotting the isotope shift measurements of the two transitions against each other and compare them to the previous best measurements [31, 32] in Figure 47.

This plot represents a projection of the three dimensional analysis onto the two isotope shift axis. Here we can see agreement with the former measurements, but an offset is observed. This is attributed to difficulty in calibrating the acceleration voltage used to scan the resonance frequency through the Doppler shift in fast ion beam colinear laser spectroscopy used for the previous data. The small systematic shifts of our measurements allow the calibration of this voltage and thus significantly reduce systematic effects in this technique. In Figure 48, the projections onto the other two planes are displayed. From the measured isotope shifts we can determine the electronic factors that connect the nuclear properties to the measured electronic transition frequencies, as described in Section 6.1. The measured field and mass shift constants are compared with theoretical calculations in Ta-

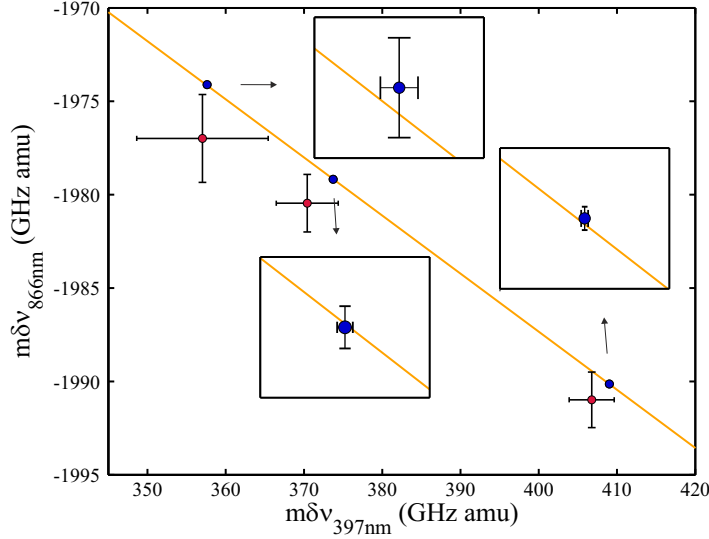


Figure 47: **King plot of the measured isotope shifts.** Isotope shift measurements of the ${}^2D_{3/2} \rightarrow {}^2P_{1/2}$ transition plotted against the measured shifts of the ${}^2S_{1/2} \rightarrow {}^2P_{1/2}$ transition. The red dots represent the formerly most accurate measurements and the blue dots are the measurements presented here. For the insets the relevant ranges were enlarged by a factor of approximately 30 and are illustrating the quality of the fit.

ble 4. As can be seen from the table, the field shift constants are in well agreement with the calculations. The calculated mass shift constants are out of the range of the measurement uncertainties, since these highly complex calculations do not provide the accuracy of our measurements. This is mainly due to the fact that the field shift constants are calculated from wave functions at the nucleus which can be performed with a high accuracy, but the mass shift constants have to be calculated from two body operators of correlated electron momenta, as explained in Section 6.1. Therefore the determined values may serve as a benchmark for future calculations.

transition	${}^2S_{1/2} \rightarrow {}^2P_{1/2}$	${}^2D_{3/2} \rightarrow {}^2P_{1/2}$
$F_{i,\text{meas}}$ (MHz/fm ²)	-281.8(7.0)	87.7(2.2)
$F_{i,\text{calc}}$ (MHz/fm ²) [32]	-285(3)	88(3)
$F_{i,\text{calc}}$ (MHz/fm ²) [130]	-287	92
$k_{i,\text{meas}}$ (GHz amu)	408.73(40)	-1990.05(13)
$k_{i,\text{calc}}$ (GHz amu) [130]	359	-2207

Table 4: **Comparison of measured and calculated field and mass shift constants.** The constants were extracted from the multidimensional King plot analysis in Equation (76).

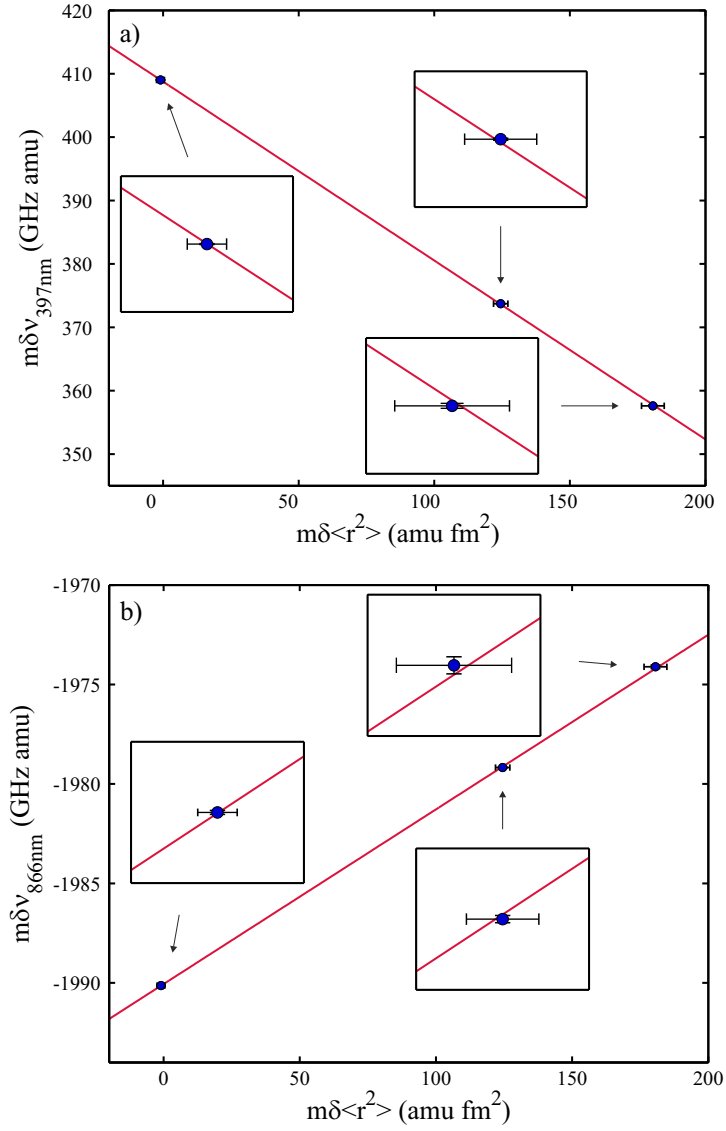


Figure 48: **King plot of isotopic shifts plotted against the nuclear charge radius.** Measured isotope shifts of a) the $^2S_{1/2} \rightarrow ^2P_{1/2}$ and b) the $^2D_{3/2} \rightarrow ^2P_{1/2}$ transition plotted against the nuclear charge radii taken from [129]. For the insets the relevant ranges were enlarged by a factor of approximately 8 and are illustrating the quality of the fit.

isotope	$\delta \langle r_t^2 \rangle$ (fm ²)	$\delta \langle r^2 \rangle$ (fm ²)	$\delta \langle r^2 \rangle$ (fm ²)
	this work	[125]	[129]
42	0.2160(49)	0.2153(49)	0.210(7)
44	0.2824(65)	0.2832(64)	0.290(9)
48	0.0045(60)	-0.0044(60)	-0.005(6)

Table 5: **Extracted change of mean square nuclear charge radius.** The values were extracted from the three dimensional King plot analysis in Equation (76) and are compared to former measurements

Additionally to the field and mass shift constants the three dimensional analysis provides more precise values for the change of the mean square nuclear charge radius (see Equation (76)). For comparison the values extracted from former isotope shift measurements are given. The results are shown in Table 5. We see that the new analysis improves the accuracy of the changes in mean square nuclear charge radius and is in excellent agreement with the values derived for neutral calcium [125].

6.7 SUMMARY AND OUTLOOK

In conclusion we measured the isotope shifts of the stable, even isotopes in calcium ions with the PRS technique and improved the accuracy of these shifts by up to 2 orders of magnitude. A modified technique has been introduced to measure non-closed transitions with high accuracy. We showed that the technique of photon recoil spectroscopy is highly accurate and sensitive and is suitable to perform precision isotope shift measurements of different species such as Fe⁺ or Ti⁺ for the investigation of the variation of fundamental constants, where quasar absorption spectra are compared to laboratory data. The isotope shifts are not resolved in the quasar absorption spectra and precise laboratory data for the isotope shifts can resolve a possible source of systematic error in this analysis [131].

With the highly accurate isotope shift results we performed a multi-dimensional King plot analysis and extracted the field and mass shift constants of the measured transitions, using measured mean square nuclear charge radii from [129]. To our knowledge we determined the most precise mass shift constant of a complex atomic system. Furthermore, in the analysis we were able to reduce the uncertainty of the relative mean square nuclear charge radii of the measured isotopes. The improved uncertainty of the mass and the field shift constants from the King plot analysis may be used to validate calculations and determine optimal models used in current isotope shift calculations, as for example in [7, 6], but the complicated structure of Ca⁺ makes

these calculations challenging.

SUMMARY AND OUTLOOK

In this thesis precision measurements of the isotope shift in calcium ions using the photon recoil spectroscopy technique have been presented. For the new spectroscopy technique new technologies enabling the high precision were developed and implemented in the setup. One major improvement was the incorporation of a new photonic crystal fiber which provides single mode transmission of UV radiation. In a collaboration with the Max Planck institute for the science of light in Erlangen the guiding properties of the hollow core PCF in the UV spectral region were characterized. The fiber exhibits an attenuation as low as 0.8 dB/m, acceptable bend sensitivity for bending radii used in the setup, and a single output mode. Most importantly, we observed no UV induced damage during transmission of more than 15 mW of UV radiation at a wavelength of 280 nm for more than 100 h. The implementation of the fiber in the setup led to a reduction of beam pointing fluctuations at the ion's position and consequently improved the coherent control of our hyperfine qubit states. These fluctuations were one of the main error contributions in the context of coherent control operations of these qubits [75]. Furthermore, the investigated hollow core PCF promises application in many fields of physics, such as atomic clocks, quantum computation and quantum simulation, where single mode guidance of UV radiation is desired.

Another technique that has been investigated in the scope of this thesis was STIRAP, which, among other adiabatic techniques, promises motional state independent transfer between electronic energy levels of atoms or ions. Here, we determined the parameter regime where efficient transfer is possible in our setup and we found agreement between the measurements and density matrix simulations performed for our system parameters. We were able to show that the technique provides motional state-independent transfer of population between two hyperfine states. Furthermore, using a STIRAP red sideband pulse, we were able to efficiently detect the motional ground state population and determine the temperature of the ion after Doppler cooling, in agreement with typical temperatures after Doppler cooling in ion trap experiments. Furthermore, we showed that for our system the STIRAP technique is favorable compared to Rabi π -pulse technique to transfer population between different hyperfine states for a thermally distributed motional state of the ion. In future experiments the technique may be used to determine the population in different motional states using more elaborate pulse sequences, consisting of STIRAP red sideband and consecutive repump pulses on carrier transitions. Thus,

enabling the determination of the motional state distribution of the ion in the trap.

Using this new technologies, the photon recoil spectroscopy technique was used to perform isotope shift measurements in Ca^+ ions. Extending the technique to non-closed transitions, we were able to measure the isotope shift of the $^2\text{S}_{1/2} \rightarrow ^2\text{P}_{1/2}$ and the $^2\text{D}_{3/2} \rightarrow ^2\text{P}_{1/2}$ transition of the even isotopes $^{42}\text{Ca}^+$, $^{44}\text{Ca}^+$ and $^{48}\text{Ca}^+$ with respect to $^{40}\text{Ca}^+$. For all measurements an uncertainty below 100 kHz was achieved, which represents an improvement by up to two orders of magnitude over previous experiments. We extracted the relative and absolute field and mass shift constants with a multi-dimensional King plot analysis [125] of the spectroscopy data, including the measured isotope shifts of both transitions and the nuclear charge radius, taken from [129]. We found agreement between the measured field shift constants and calculated values [32, 130], but the calculated mass shift constants differ significantly from the experimental results. The complex calculations due to the many body structure of the ion are challenging and do not yet reach the level of precision of our measurements, making the determined mass shift constant a benchmark for future calculations. In a future experiment the isotope shift of the $^2\text{S}_{1/2} \rightarrow ^2\text{P}_{3/2}$ -transition in calcium ions will be measured in our system. The difference of the specific mass shift constants of the $^2\text{P}_{1/2}$ - and the $^2\text{P}_{3/2}$ -state is calculated to be on the order of $4 \text{ GHz} \cdot \text{amu}$ [130] leading to a difference of 17 MHz for the isotope shift between $^{40}\text{Ca}^+$ and $^{48}\text{Ca}^+$. This may enable the detection of differences of the isotope shift between the $^2\text{P}_{1/2}$ and the $^2\text{P}_{3/2}$ level in calcium for the first time.

In an absolute frequency measurement of the $^{40}\text{Ca}^+ ^2\text{S}_{1/2} \rightarrow ^2\text{P}_{1/2}$ transition [114] we showed that the PRS technique is highly sensitive. Only on the order of 10 photons need to be scattered during one spectroscopic cycle to achieve a signal to noise ratio of 1. This may enable measurements of absolute frequencies and isotope shifts in complex metal ions such as titanium or iron, where the number of scattered photons during one experimental cycle is expected to be low. Also for the spectroscopy of highly charged ions, whose hyperfine transitions are located in the visible range, this high sensitivity may be an interesting alternative to the original QLS. These measurements are relevant for the investigations of possible changes of fundamental constants, where especially the highly charged ions are predicted to have a high sensitivity [27]. Furthermore, the sensitivity of the developed spectroscopy technique can be improved using non-classical states of motion to transfer the spectroscopic information. For spectroscopy techniques utilizing the motion of the ions, the sensitivity is proportional to the spread of the wavefunction of the ion. This is enlarged for a squeezed state of motion, which for example can be created by a parametric drive induced by an optical dipole force

modulated at twice the normal mode frequency [54]. This may lead to single photon sensitivity using the PRS technique. For example, a motional Schrödinger cat state was utilized to demonstrate single photon sensitivity [38].

In another approach, the technique can be modified to enable non-destructive rotational state spectroscopy of molecular ions (see for example [67]). Here the logic ion is trapped together with a molecular ion. A Raman coupling between two motional states via an optical lattice can be used to non-destructively detect the rotational state of the molecular ion. These states are coupled by black-body radiation changing the rotational state of the molecule on timescales of seconds [132]. The probability of the ion to be in a specific rotational state can be detected by means of quantum jumps. By that, the molecular ion may serve as an in situ temperature probe in the ion trap. Furthermore, after the detection of the ion in a specific rotational state, spectroscopy of a pure vibrational transition could be performed. This investigations are relevant in the context of variations of fundamental constants, where they provide a high sensitivity to temporal changes of the proton to electron mass ratio m_p/m_e .

BIBLIOGRAPHY

- [1] J. Fraunhofer. Bestimmung des Brechungs- und des Farbenzerstreuungs-Vermögens verschiedener Glasarten in Bezug auf die Vervollkommnung achromatischer Fernrohre. *Ann. Phys.*, 55:264, 1817.
- [2] A. J. Angström. Optische Untersuchungen. *Ann. Phys.*, 170:141, 1855.
- [3] A. L. Schawlow. Spectroscopy in a new light. *Rev. Mod. Phys.*, 54(3):697–707, 1982. URL <http://link.aps.org/doi/10.1103/RevModPhys.54.697>.
- [4] W. Demtröder. *Laser Spectroscopy, fourth edition*. Springer, 2008.
- [5] ATLAS Collaboration. Observation of a new particle in the search for the standard model higgs boson with the ATLAS detector at the LHC. *Phys. Lett. B*, 716(1):1–29, 2012. URL <http://linkinghub.elsevier.com/retrieve/pii/S037026931200857X>.
- [6] W. Nörtershäuser, D. Tiedemann, M. Žáková, Z. Andjelkovic, K. Blaum, M. Bissell, R. Cazan, G. Drake, Ch. Geppert, M. Kowalska, J. Krämer, A. Krieger, R. Neugart, R. Sánchez, F. Schmidt-Kaler, Z.-C. Yan, D. Yordanov, and C. Zimmermann. Nuclear charge radii of $\text{Be}^{7,9,10}$ and the one-neutron halo nucleus Be^{11} . *Phys. Rev. Lett.*, 102(6), 2009. URL <http://link.aps.org/doi/10.1103/PhysRevLett.102.062503>.
- [7] R. Sánchez, W. Nörtershäuser, G. Ewald, D. Albers, J. Behr, P. Bricault, B. Bushaw, A. Dax, J. Dilling, M. Domsbky, G. Drake, S. Götte, R. Kirchner, H.-J. Kluge, Th. Kühl, J. Lassen, C. Levy, M. Pearson, E. Prime, V. Ryjkov, A. Wojtaszek, Z.-C. Yan, and C. Zimmermann. Nuclear charge radii of $\text{Li}^{9,11}$: The influence of halo neutrons. *Phys. Rev. Lett.*, 96(3), 2006. URL <http://link.aps.org/doi/10.1103/PhysRevLett.96.033002>.
- [8] W. Paul. Nobel lecture: Electromagnetic traps for charged and neutral particles. *Rev. Mod. Phys.*, 62:531–540, 1990. URL <http://link.aps.org/doi/10.1103/RevModPhys.62.531>.
- [9] W. Neuhauser, M. Hohenstatt, P. Toschek, and H. Dehmelt. Optical-sideband cooling of visible atom cloud confined in parabolic well. *Phys. Rev. Lett.*, 41:233–236, 1978. URL <http://link.aps.org/doi/10.1103/PhysRevLett.41.233>.

- [10] D. J. Wineland, R. E. Drullinger, and F. L. Walls. Radiation-pressure cooling of bound resonant absorbers. *Phys. Rev. Lett.*, 40:1639–1642, 1978. URL <http://link.aps.org/doi/10.1103/PhysRevLett.40.1639>.
- [11] D. J. Wineland and Wayne M. Itano. Laser cooling of atoms. *Phys. Rev. A*, 20:1521–1540, 1979. URL <http://link.aps.org/doi/10.1103/PhysRevA.20.1521>.
- [12] W. D. Phillips. Nobel lecture: Laser cooling and trapping of neutral atoms. *Rev. Mod. Phys.*, 70:721, 1998. URL http://www.nobelprize.org/nobel_prizes/physics/laureates/1997/phillips-lecture.html.
- [13] F. Diedrich, J. C. Bergquist, Wayne M. Itano, and D. J. Wineland. Laser cooling to the zero-point energy of motion. *Phys. Rev. Lett.*, 62:403–406, 1989. URL <http://link.aps.org/doi/10.1103/PhysRevLett.62.403>.
- [14] C. Monroe, D. M. Meekhof, B. E. King, S. R. Jefferts, W. M. Itano, D. J. Wineland, and P. Gould. Resolved-sideband raman cooling of a bound atom to the 3d zero-point energy. *Phys. Rev. Lett.*, 75(22):4011, 1995. URL <http://journals.aps.org/prl/abstract/10.1103/PhysRevLett.75.4011>.
- [15] C. W. Chou, D. B. Hume, J. C. J. Koelemeij, D. J. Wineland, and T. Rosenband. Frequency comparison of two high-accuracy Al^+ optical clocks. *Phys. Rev. Lett.*, 104:070802, 2010. URL <http://link.aps.org/doi/10.1103/PhysRevLett.104.070802>.
- [16] N. Huntemann, M. Okhapkin, B. Lipphardt, S. Weyers, Chr. Tamm, and E. Peik. High-accuracy optical clock based on the octupole transition in $^{171}\text{Yb}^+$. *Phys. Rev. Lett.*, 108:090801, 2012. URL <http://link.aps.org/doi/10.1103/PhysRevLett.108.090801>.
- [17] N. Huntemann, B. Lipphardt, Chr. Tamm, V. Gerginov, S. Weyers, and E. Peik. Improved limit on a temporal variation of m_p/m_e from comparisons of Yb^+ and Cs atomic clocks. *Phys. Rev. Lett.*, 113:210802, 2014. URL <http://link.aps.org/doi/10.1103/PhysRevLett.113.210802>.
- [18] R. M. Godun, P. B. R. Nisbet-Jones, J. M. Jones, S. A. King, L. A. M. Johnson, H. S. Margolis, K. Szymaniec, S. N. Lea, K. Bongs, and P. Gill. Frequency ratio of two optical clock transitions in $^{171}\text{Yb}^+$ and constraints on the time variation of fundamental constants. *Phys. Rev. Lett.*, 113:210801, 2014. URL <http://link.aps.org/doi/10.1103/PhysRevLett.113.210801>.

- [19] T. Rosenband, D. B. Hume, P. O. Schmidt, C. W. Chou, A. Brusch, L. Lorini, W. H. Oskay, R. E. Drullinger, T. M. Fortier, J. E. Stalnaker, S. A. Diddams, W. C. Swann, N. R. Newbury, W. M. Itano, D. J. Wineland, and J. C. Bergquist. Frequency ratio of Al^+ and Hg^+ single-ion optical clocks; metrology at the 17th decimal place. *Science*, 319(5871):1808–1812, 2008. URL <http://www.sciencemag.org/cgi/doi/10.1126/science.1154622>.
- [20] J. K. Webb, M. T. Murphy, V. V. Flambaum, V. A. Dzuba, J. D. Barrow, C. W. Churchill, J. X. Prochaska, and A. M. Wolfe. Further evidence for cosmological evolution of the fine structure constant. *Phys. Rev. Lett.*, 87:091301, 2001. URL <http://link.aps.org/doi/10.1103/PhysRevLett.87.091301>.
- [21] R. Srianand, H. Chand, P. Petitjean, and B. Aracil. Limits on the time variation of the electromagnetic fine-structure constant in the low energy limit from absorption lines in the spectra of distant quasars. *Phys. Rev. Lett.*, 92:121302, 2004. URL <http://link.aps.org/doi/10.1103/PhysRevLett.92.121302>.
- [22] M. T. Murphy and J. C. Berengut. Laboratory atomic transition data for precise optical quasar absorption spectroscopy. *Mon. Not. R. Astron. Soc.*, 438(1):388–411, 2014. URL <http://mnras.oxfordjournals.org/cgi/doi/10.1093/mnras/stt2204>.
- [23] J. K. Webb, J. A. King, M. T. Murphy, V. V. Flambaum, R. F. Carswell, and M. B. Bainbridge. Indications of a spatial variation of the fine structure constant. *Phys. Rev. Lett.*, 107(19), 2011. URL <http://link.aps.org/doi/10.1103/PhysRevLett.107.191101>.
- [24] J. C. Berengut, E. M. Kava, and V. V. Flambaum. Is there a spatial gradient in values of the fine-structure constant? A reanalysis of the results. *A&A*, 542:A118, 2012. URL <http://www.aanda.org/10.1051/0004-6361/201219286>.
- [25] M. G. Kozlov, V. A. Korol, J. C. Berengut, V. A. Dzuba, and V. V. Flambaum. Space-time variation of the fine-structure constant and evolution of isotope abundances. *Phys. Rev. A*, 70:062108, 2004. URL <http://link.aps.org/doi/10.1103/PhysRevA.70.062108>.
- [26] P. O. Schmidt, T. Rosenband, W. M. Langer, C. and Itano, J. C. Bergquist, and D. J. Wineland. Spectroscopy using quantum logic. *Science*, 309(5735):749–752, 2005. URL <http://www.sciencemag.org/cgi/doi/10.1126/science.1114375>.
- [27] J. C. Berengut, V. A. Dzuba, and V. V. Flambaum. Enhanced laboratory sensitivity to variation of the fine-structure constant using highly charged ions. *Phys. Rev. Lett.*, 105(12), 2010. URL <http://link.aps.org/doi/10.1103/PhysRevLett.105.120801>.

- [28] K. Heilig and A. Streudel. Changes in mean square nuclear charge radii from optical isotope shifts. *At. Data Nucl. Data Tables*, 1974. URL [http://dx.doi.org/10.1016/S0092-640X\(74\)80006-9](http://dx.doi.org/10.1016/S0092-640X(74)80006-9).
- [29] D. N. Stacey. Isotope shifts and nuclear charge distributions. *Rep. Prog. Phys.*, 29(1):171, 1966. URL <http://iopscience.iop.org/0034-4885/29/1/304>.
- [30] W. H. King. Comments on the article 'Peculiarities of the isotope shift in the samarium spectrum'. *J. Opt. Soc. Am.*, 53(5):638–639, 1963. URL <http://www.opticsinfobase.org/abstract.cfm?uri=josa-53-5-638>.
- [31] W. Nörtershäuser, K. Blaum, K. Icker, P. Müller, A. Schmitt, K. Wendt, and B. Wiche. Isotope shifts and hyperfine structure in the transitions in calcium II. *Eur. Phys. J. D*, 2(1):33–39, 1998. URL <http://link.springer.com/article/10.1007/s100530050107>.
- [32] A. M. Mårtensson-Pendrill, A. Ynnerman, H. Warston, L. Vermeeren, R. E. Silverans, A. Klein, R. Neugart, C. Schulz, P. Lievens, and ISOLDE Collaboration. Isotope shifts and nuclear-charge radii in singly ionized $^{40-48}\text{Ca}$. *Phys. Rev. A*, 45(7):4675, 1992. URL http://pra.aps.org/abstract/PRA/v45/i7/p4675_1.
- [33] J. Berengut, V. Dzuba, and V. Flambaum. Isotope-shift calculations for atoms with one valence electron. *Phys. Rev. A*, 68(2), 2003. URL <http://link.aps.org/doi/10.1103/PhysRevA.68.022502>.
- [34] G. Ewald, W. Nörtershäuser, A. Dax, S. Götze, R. Kirchner, H.-J. Kluge, T. Kühl, R. Sánchez, A. Wojtaszek, B. Bushaw, G. Drake, Z.-C. Yan, and C. Zimmermann. Nuclear charge radii of $\text{Li}^{8,9}$ determined by laser spectroscopy. *Phys. Rev. Lett.*, 93(11), 2004. URL <http://link.aps.org/doi/10.1103/PhysRevLett.93.113002>.
- [35] N. Yamamoto, L. Tao, and A. P. Yalin. Single-mode delivery of 250 nm light using a large mode area photonic crystal fiber. *Opt. Express*, 17(19):16933–16940, 2009. URL <http://www.opticsinfobase.org/abstract.cfm?uri=oe-17-19-16933>.
- [36] R. F. Cregan. Single-mode photonic band gap guidance of light in air. *Science*, 285(5433):1537–1539, 1999. URL <http://www.sciencemag.org/cgi/doi/10.1126/science.285.5433.1537>.
- [37] F. Benabid. Stimulated raman scattering in hydrogen-filled hollow-core photonic crystal fiber. *Science*, 298(5592):399–402,

2002. URL <http://www.sciencemag.org/cgi/doi/10.1126/science.1076408>.
- [38] C. Hempel, B. P. Lanyon, P. Jurcevic, R. Gerritsma, R. Blatt, and C. F. Roos. Entanglement-enhanced detection of single-photon scattering events. *Nature Photon.*, 7(8):630–633, 2013. URL <http://www.nature.com/nphoton/journal/v7/n8/abs/nphoton.2013.172.html>.
- [39] S. Kotler, N. Akerman, N. Navon, Y. Glickman, and R. Ozeri. Measurement of the magnetic interaction between two bound electrons of two separate ions. *Nature*, 510(7505):376–380, 2014. URL <http://www.nature.com/doi/10.1038/nature13403>.
- [40] J. L. Sørensen, D. Møller, T. Iversen, J. B. Thomsen, F. Jensen, P. Staunum, D. Voigt, and M. Drewsen. Efficient coherent internal state transfer in trapped ions using stimulated raman adiabatic passage. *New J. Phys.*, 8(11):261–261, 2006. URL <http://stacks.iop.org/1367-2630/8/i=11/a=261?key=crossref.316be66fb81074e2e56720c1c797d7a4>.
- [41] A. Friedenauer, H. Schmitz, J. T. Glueckert, D. Porras, and T. Schätz. Simulating a quantum magnet with trapped ions. *Nature Physics*, 4(10):757–761, 2008. URL <http://www.nature.com/doi/10.1038/nphys1032>.
- [42] H. Häffner, W. Hänsel, C. F. Roos, J. Benhelm, D. Chek-al kar, M. Chwalla, T. Körber, U. D. Rapol, M. Riebe, P. O. Schmidt, C. Becher, O. Gühne, W. Dür, and R. Blatt. Scalable multi-particle entanglement of trapped ions. *Nature*, 438(7068):643–646, 2005. URL <http://www.nature.com/doi/10.1038/nature04279>.
- [43] D. J. Berkeland, J. D. Miller, J. C. Bergquist, W. M. Itano, and D. J. Wineland. Minimization of ion micromotion in a Paul trap. *J. Appl. Phys.*, 83:5025–5033, 1998. URL <http://tf.nist.gov/general/pdf/1226.pdf>.
- [44] Richard J. Cook, Donn G. Shankland, and Ann L. Wells. Quantum theory of particle motion in a rapidly oscillating field. *Phys. Rev. A*, 31(2):564, 1985. URL <http://journals.aps.org/prabstract/10.1103/PhysRevA.31.564>.
- [45] D. Leibfried, R. Blatt, C. Monroe, and D. Wineland. Quantum dynamics of single trapped ions. *Rev. Mod. Phys.*, 75(1):281, 2003. URL <http://journals.aps.org/rmp/abstract/10.1103/RevModPhys.75.281>.

- [46] D. J. Wineland, C. Monroe, W. M. Itano, D. Leibfried, B. E. King, and D. M. Meekhof. Experimental issues in coherent quantum-state manipulation of trapped atomic ions. *J. Res. Natl. Inst. Stand. Tech.*, 103:259–328, 1998. URL <http://tf.nist.gov/general/pdf/1275.pdf>.
- [47] P.K. Gosh. *Ion Traps*. Clarendon Press, 1995.
- [48] B. Hemmerling. *Towards Direct Frequency Comb Spectroscopy Using Quantum Logic*. PhD thesis, Gottfried Wilhelm Leibniz Universität Hannover, 2011.
- [49] J. B. Wübbena, S. Amairi, O. Mandel, and P. O. Schmidt. Sympathetic cooling of mixed-species two-ion crystals for precision spectroscopy. *Phys. Rev. A*, 85(4), 2012. URL <http://link.aps.org/doi/10.1103/PhysRevA.85.043412>.
- [50] D. F. V. James. Quantum dynamics of cold trapped ions with application to quantum computation. *App. Phys. B*, 66(2):181–190, 1998. URL <http://www.springerlink.com/index/01E0NUG5VLV9DTA2.pdf>.
- [51] G. Morigi and H. Walther. Two species coulomb chains for quantum information. *Eur. Phys. J. D*, 13(2):261–269, 2001. URL <http://link.springer.com/article/10.1007/s100530170275>.
- [52] D. Kielpinski, B. E. King, C. J. Myatt, C. A. Sackett, Q. A. Turchette, W. M. Itano, C. Monroe, D. J. Wineland, and W. H. Zurek. Sympathetic cooling of trapped ions for quantum logic. *Phys. Rev. A*, 61(3):032310, 2000. URL <http://journals.aps.org/pr/abstract/10.1103/PhysRevA.61.032310>.
- [53] J. B. Wübbena. *Controlling motion in quantum logic clocks*. PhD thesis, Gottfried Wilhelm Leibniz Universität Hannover, 2014.
- [54] D. M. Meekhof, C. Monroe, B. E. King, W. M. Itano, and D. J. Wineland. Generation of nonclassical motional states of a trapped atom. *Phys. Rev. Lett.*, 76(11):1796, 1996. URL <http://journals.aps.org/prl/abstract/10.1103/PhysRevLett.76.1796>.
- [55] S. Stenholm. The semiclassical theory of laser cooling. *Rev. Mod. Phys.*, 58(3):699, 1986. URL <http://journals.aps.org/rmp/abstract/10.1103/RevModPhys.58.699>.
- [56] T. W. Hänsch and A. L. Schawlow. Cooling of gases by laser radiation. *Opt. Comm.*, 13(1):68–69, 1975. URL <http://www.sciencedirect.com/science/article/pii/0030401875901595>.

- [57] D. J. Wineland and H. Dehmelt. Proposed 10^{14} laser fluorescence spectroscopy on Ti^+ mono-ion oscillator III. *Bull. Am. Phys. Soc.*, 20:637, 1975.
- [58] C. J. Foot. *Atomic Physics*. Oxford University Press, Oxford, Great Britain, 2005.
- [59] D. J. Heinzen and D. J. Wineland. Quantum-limited cooling and detection of radio-frequency oscillations by laser-cooled ions. *Phys. Rev. A*, 42(5):2977, 1990. URL <http://journals.aps.org/prabstract/10.1103/PhysRevA.42.2977>.
- [60] C. Gerry and P Knight. *Introductory quantum optics Traps*. Cambridge University Press, 2005.
- [61] M.P. Fewell. Adiabatic elimination, the rotating-wave approximation and two-photon transitions. *Opt. Comm.*, 253(1-3):125–137, 2005. URL <http://linkinghub.elsevier.com/retrieve/pii/S0030401805003962>.
- [62] J. Steinbach, J. Twamley, and P. L. Knight. Engineering two-mode interactions in ion traps. *Phys. Rev. A*, 56(6):4815, 1997. URL <http://journals.aps.org/prabstract/10.1103/PhysRevA.56.4815>.
- [63] N. Kjaergaard, L. Hornekaer, A.M. Thommesen, Z. Videsen, and M. Drewsen. Isotope selective loading of an ion trap using resonance-enhanced two-photon ionization. *Appl. Phys. B*, 71(2):207–210, 2000. URL <http://link.springer.com/10.1007/s003400000296>.
- [64] D. Lucas, A. Ramos, J. Home, M. McDonnell, S. Nakayama, J.-P. Stacey, S. Webster, D. Stacey, and A. Steane. Isotope-selective photoionization for calcium ion trapping. *Phys. Rev. A*, 69(1), 2004. URL <http://link.aps.org/doi/10.1103/PhysRevA.69.012711>.
- [65] B. Hemmerling, F. Gebert, Y. Wan, D. Nigg, I. V. Sherstov, and P. O. Schmidt. A single laser system for ground-state cooling of $^{25}\text{Mg}^+$. *Appl. Phys. B*, 104(3):583–590, 2011. URL <http://link.springer.com/10.1007/s00340-011-4444-0>.
- [66] Y. Wan, F. Gebert, F. Wolf, and P. O. Schmidt. Efficient sympathetic motional-ground-state cooling of a molecular ion. *Phys. Rev. A*, 91:043425, 2015. URL <http://link.aps.org/doi/10.1103/PhysRevA.91.043425>.
- [67] Y. Wan. *Quantum Logic Spectroscopy of Atomic and Molecular Ions*. PhD thesis, Gottfried Wilhelm Leibniz Universität Hannover, 2014.

- [68] P. Pham. *A general-purpose pulse sequencer for quantum computing*. PhD thesis, Massachusetts Institute of Technology, 2005. URL <http://18.7.29.232/handle/1721.1/32106>.
- [69] H. Dehmelt. Proposed 10^{14} laser fluorescence spectroscopy on Tl^+ mono- ion oscillator II (spontaneous quantum jumps). *Bull. Am. Phys. Soc.*, 20:60, 1975.
- [70] W. M. Itano, J. C. Bergquist, J. J. Bollinger, J. M. Gilligan, D. J. Heinzen, F. L. Moore, M. G. Raizen, and D. J. Wineland. Quantum projection noise: Population fluctuations in two-level systems. *Phys. Rev. A*, 47(5):3554, 1993. URL <http://journals.aps.org/prabstract/10.1103/PhysRevA.47.3554>.
- [71] B. Hemmerling, F. Gebert, Y. Wan, and P. O. Schmidt. A novel, robust quantum detection scheme. *New J. Phys*, 14(2):023043, 2012. URL <http://stacks.iop.org/1367-2630/14/i=2/a=023043?key=crossref.1561972a263832ecf0ed86e8b9a902c2>.
- [72] T. Kessler, C. Hagemann, C. Grebing, T. Legero, U. Sterr, F. Riehle, M. J. Martin, L. Chen, and J. Ye. A sub-40-mHz-linewidth laser based on a silicon single-crystal optical cavity. *Nature Photon.*, 6(10):687–692, 2012. URL <http://dx.doi.org/10.1038/nphoton.2012.217>.
- [73] D. A. Howe, D. W. Allan, and J. A. Barnes. Properties of signal sources and measurement methods. *Thirty Fifth Annual Frequency Control Symposium.*, pages 669 – 716, 1981.
- [74] F. Riehle. *Frequency Standards*. Wiley-VCH, Weinheim, Germany, 2004.
- [75] J. P. Gaebler, A. M. Meier, T. R. Tan, R. Bowler, Y. Lin, D. Hanneke, J. D. Jost, J. P. Home, E. Knill, D. Leibfried, and D. J. Wineland. Randomized benchmarking of multiqubit gates. *Phys. Rev. Lett.*, 108(26), 2012. URL <http://link.aps.org/doi/10.1103/PhysRevLett.108.260503>.
- [76] F. Gebert, M. H. Frosz, T. Weiss, Y. Wan, A. Ermolov, N. Y. Joly, P. O. Schmidt, and P. St.J. Russell. Damage-free single-mode transmission of deep-UV light in hollow-core PCF. *Opt. Express*, 22(13):15388, 2014. URL <http://www.opticsinfobase.org/abstract.cfm?URI=oe-22-13-15388>.
- [77] B. E. A. Saleh and M. C. Teich. *Fundamentals of Photonics*. John Wiley and sons, inc., New York, 1991.
- [78] F. Zolla, G. Renversez, A. Nicolet, B. Kuhlmeiy, S. Guenneau, and D. Falbacq. *Foundations of Photonic Crystal Fibres*. Imperial College Press, London, 2005.

- [79] T. A. Birks, J. C. Knight, and P. St.J. Russell. Endlessly single-mode photonic crystal fiber. *Opt. Lett.*, 22(13):961–963, 1997. URL <http://www.opticsinfobase.org/abstract.cfm?uri=ol-22-13-961>.
- [80] P. St.J. Russell. Photonic-crystal fibers. *J. Lightw. Technol.*, 24(12):4729–4749, 2006. URL <http://ieeexplore.ieee.org/lpdocs/epic03/wrapper.htm?arnumber=4063429>.
- [81] F. Benabid and P.J. Roberts. Linear and nonlinear optical properties of hollow core photonic crystal fiber. *J. Mod. Opt.*, 58(2):87–124, 2011. URL <http://www.tandfonline.com/doi/abs/10.1080/09500340.2010.543706>.
- [82] J. C. Knight, J. Broeng, T. A. Birks, and P. St.J. Russell. Photonic band gap guidance in optical fibers. *Science*, 282(5393):1476–1478, 1998. URL <http://www.sciencemag.org/cgi/doi/10.1126/science.282.5393.1476>.
- [83] A. Argyros, S. G. Leon-Saval, J. Pla, and A. Docherty. Antiresonant reflection and inhibited coupling in hollow-core square lattice optical fibres. *Opt. Express*, 16(8):5642–5648, 2008. URL <http://www.opticsinfobase.org/abstract.cfm?uri=oe-16-8-5642>.
- [84] F. Couny, F. Benabid, P. J. Roberts, P. S. Light, and M. G. Raymer. Generation and photonic guidance of multi-octave optical-frequency combs. *Science*, 318(5853):1118–1121, 2007. URL <http://www.sciencemag.org/cgi/doi/10.1126/science.1149091>.
- [85] G. J. Pearce, G. S. Wiederhecker, C. G. Poulton, S. Burger, and P. St.J. Russell. Models for guidance in kagome-structured hollow-core photonic crystal fibres. *Opt. Express*, 15(20):12680–12685, 2007. URL <http://www.opticsinfobase.org/abstract.cfm?uri=oe-15-20-12680>.
- [86] S. Février, B. Beaudou, and P. Viale. Understanding origin of loss in large pitch hollow-core photonic crystal fibers and their design simplification. *Opt. Express*, 18(5):5142–5150, 2010. URL <http://www.opticsinfobase.org/abstract.cfm?uri=oe-18-5-5142>.
- [87] J.-L. Archambault, Richard J. Black, Suzanne Lacroix, and Jacques Bures. Loss calculations for antiresonant waveguides. *J. Lightw. Technol.*, 11(3):416–423, 1993. URL http://ieeexplore.ieee.org/xpls/abs_all.jsp?arnumber=219574.
- [88] N. M. Litchinitser, A. K. Abeeluck, C. Headley, and B. J. Eggleton. Antiresonant reflecting photonic crystal optical waveguides. *Opt. Lett.*, 27(18):1592–1594, 2002. URL <http://www.opticsinfobase.org/abstract.cfm?uri=ol-27-18-1592>.

- [89] J. Nold, P. Hölzer, N. Y. Joly, G. K. L. Wong, A. Nazarkin, A. Podlipensky, M. Scharrer, and P. St.J. Russell. Pressure-controlled phase matching to third harmonic in Ar-filled hollow-core photonic crystal fiber. *Opt. Lett.*, 35(17):2922–2924, 2010. URL <http://www.opticsinfobase.org/abstract.cfm?uri=ol-35-17-2922>.
- [90] J. C. Travers, W. Chang, N. Y. Nold, J. Joly, and P. St.J. Russell. Ultrafast nonlinear optics in gas-filled hollow-core photonic crystal fibers. *J. Opt. Soc. Am. B*, 28(12):A11–A26, 2011. URL <http://dx.doi.org/10.1364/JOSAB.28.000A11>.
- [91] S. Février, F. Gérôme, A. Labruyère, B. Beaudou, G. Humbert, and J.-L. Auguste. Ultraviolet guiding hollow-core photonic crystal fiber. *Opt. Lett.*, 34(19):2888–2890, 2009. URL <http://www.opticsinfobase.org/abstract.cfm?uri=ol-34-19-2888>.
- [92] T. D. Bradley, Y. Wang, M. Alharbi, B. Debord, C. Fourcade-Dutin, B. Beaudou, F. Gerome, and F. Benabid. Optical properties of low loss (70 dB/km) hypocycloid-core kagome hollow core photonic crystal fiber for Rb and Cs based optical applications. *J. Lightw. Technol.*, 31(16):2752–2755, 2013. URL <http://ieeexplore.ieee.org/lpdocs/epic03/wrapper.htm?arnumber=6557420>.
- [93] R. G. Driggers. *Encyclopedia of optical engineering, Volume 3*. Marcel Dekker, Inc, New York, USA, 2003.
- [94] S. Schneider and Gerard J. Milburn. Decoherence in ion traps due to laser intensity and phase fluctuations. *Phys. Rev. A*, 57(5):3748, 1998. URL http://pra.aps.org/abstract/PRA/v57/i5/p3748_1.
- [95] R. Ozeri, W. Itano, R. Blakestad, J. Britton, J. Chiaverini, J. Jost, C. Langer, D. Leibfried, R. Reichle, S. Seidelin, J. Wesenberg, and D. Wineland. Errors in trapped-ion quantum gates due to spontaneous photon scattering. *Phys. Rev. A*, 75(4), 2007. URL <http://link.aps.org/doi/10.1103/PhysRevA.75.042329>.
- [96] B. Debord, M. Alharbi, T. Bradley, C. Fourcade-Dutin, Y.Y. Wang, L. Vincetti, F. Gérôme, and F. Benabid. Hypocycloid-shaped hollow-core photonic crystal fiber part i: Arc curvature effect on confinement loss. *Opt. Express*, 21(23):28597, 2013. URL <http://www.opticsinfobase.org/abstract.cfm?URI=oe-21-23-28597>.
- [97] Y. Colombe, D. H. Slichter, A. C. Wilson, D. Leibfried, and D. J. Wineland. Single-mode optical fiber for high-power, low-loss UV transmission. *Opt. Express*, 22:19783–19793, 2014. URL <http://dx.doi.org/10.1364/OE.22.019783>.

- [98] R. Sahl. "Defect Related Luminescence in Silicon Dioxide Network: A Review," in "Crystalline Silicon - Properties and Uses". InTech, Rijeka, Croatia, 2011.
- [99] M. Born and V. Fock. Beweis des Adiabatenatzes. *Z. Phys.*, 51 (3-4):165–180, 1928. URL <http://link.springer.com/article/10.1007/BF01343193>.
- [100] F. Bloch. Nuclear induction. *Phys. Rev.*, 70(7-8):460, 1946. URL <http://journals.aps.org/pr/abstract/10.1103/PhysRev.70.460>.
- [101] M. M. T. Loy. Observation of population inversion by optical adiabatic rapid passage. *Phys. Rev. Lett.*, 32(15):814, 1974. URL <http://journals.aps.org/prl/abstract/10.1103/PhysRevLett.32.814>.
- [102] U. Gaubatz, P. Rudecki, S. Schiemann, and K. Bergmann. Population transfer between molecular vibrational levels by stimulated raman scattering with partially overlapping laser fields. a new concept and experimental results. *J. Chem. Phys.*, 92 (9):5363–5376, 1990. URL <http://scitation.aip.org/content/aip/journal/jcp/92/9/10.1063/1.458514>.
- [103] T. Ricketts, L. P. Yatsenko, S. Steuerwald, T. Halfmann, B. W. Shore, N. V. Vitanov, and K. Bergmann. Efficient adiabatic population transfer by two-photon excitation assisted by a laser-induced stark shift. *J. Chem. Phys.*, 113(2):534, 2000. URL <http://scitation.aip.org/content/aip/journal/jcp/113/2/10.1063/1.481829>.
- [104] K. Bergmann, H. Theuer, and B. W. Shore. Coherent population transfer among quantum states of atoms and molecules. *Rev. Mod. Phys.*, 70(3):1003, 1998. URL <http://journals.aps.org/rmp/abstract/10.1103/RevModPhys.70.1003>.
- [105] N. V. Vitanov, T. Halfmann, B. W. Shore, and K. Bergmann. Laser-induced population transfer by adiabatic passage techniques. *Annu. Rev. Phys. Chem.*, 52(1):763–809, 2001. URL <http://www.annualreviews.org/doi/full/10.1146/annurev.physchem.52.1.763>.
- [106] C. Wunderlich, T. Hannemann, T. Körber, H. Häffner, Ch. Roos, W. Hänsel, R. Blatt, and F. Schmidt-Kaler. Robust state preparation of a single trapped ion by adiabatic passage. *J. Mod. Opt.*, 54 (11):1541–1549, 2007. URL <http://www.tandfonline.com/doi/abs/10.1080/09500340600741082>.
- [107] T. Watanabe, S. Nomura, K. Toyoda, and S. Urabe. Sideband excitation of trapped ions by rapid adiabatic passage for ma-

- nipulation of motional states. *Phys. Rev. A*, 84(3), 2011. URL <http://link.aps.org/doi/10.1103/PhysRevA.84.033412>.
- [108] M. P. Fewell, B. W. Shore, and K. Bergmann. Coherent population transfer among three states: Full algebraic solutions and the relevance of non adiabatic processes to transfer by delayed pulses. *Austr. J. Phys.*, 50(2):281–308, 1997. URL <http://www.publish.csiro.au/?paper=P96071>.
- [109] D. Møller. *Adiabatic Processes in Quantum Computation - Experimental and theoretical studies*. PhD thesis, Lundbeck Foundation Theoretical Center for Quantum System Research, Department of Physics and Astronomy, University of Aarhus, 2008.
- [110] MATLAB. *version 8.2.0.701 (R2013b)*. The MathWorks Inc., Natick, Massachusetts, 2013.
- [111] S. M. Tan. A quantum optics toolbox for matlab 5. *J. Opt. B*, 1:161, 1999. URL <http://copilot.caltech.edu/classes/aph190/qousersguide.pdf>.
- [112] G. Poulsen. *Sideband Cooling of Atomic and Molecular Ions*. PhD thesis, Department of Physics and Astronomy, University of Aarhus, 2011.
- [113] M. T. Murphy and J. C. Berengut. Laboratory atomic transition data for precise optical quasar absorption spectroscopy. *Mon. Not. R. Astron. Soc.*, 438:388–411, 2014. URL <http://mnras.oxfordjournals.org/content/438/1/388>.
- [114] Y. Wan, F. Gebert, J. B. Wübbena, N. Scharnhorst, S. Amairi, I. D. Leroux, B. Hemmerling, N. Lörch, K. Hammerer, and P. O. Schmidt. Precision spectroscopy by photon-recoil signal amplification. *Nat. Comm.*, 5, 2014. URL <http://www.nature.com/doi/10.1038/ncomms4096>.
- [115] T. Pruttivarasin, M. Ramm, and H. Häffner. Direct spectroscopy of the $^2S_{1/2}$ - $^2P_{1/2}$ and $^2D_{3/2}$ - $^2P_{1/2}$ transitions and observation of micromotion modulated spectra in trapped $^{40}\text{Ca}^+$. *J. Phys. B*, 47(13):135002, 2014. URL <http://stacks.iop.org/0953-4075/47/i=13/a=135002?key=crossref.6856a61e92a547d9cf7fde8e784723fd>.
- [116] A. Gardner, K. Sheridan, W. Groom, N. Seymour-Smith, and M. Keller. Precision spectroscopy technique for dipole-allowed transitions in laser-cooled ions. *Appl. Phys. B*, 117(2):755–762, 2014. URL <http://link.springer.com/10.1007/s00340-014-5891-1>.

- [117] G. Clos, M. Enderlein, U. Warring, T. Schätz, and D. Leibfried. Decoherence-assisted spectroscopy of a single Mg^+ ion. *Phys. Rev. Lett.*, 112(11), 2014. URL <http://link.aps.org/doi/10.1103/PhysRevLett.112.113003>.
- [118] M. Herrmann, V. Batteiger, S. Knünz, G. Saathoff, Th. Udem, and T. Hänsch. Frequency metrology on single trapped ions in the weak binding limit: The $^3\text{S}_{1/2}$ - $^3\text{P}_{3/2}$ transition in $^{24}\text{Mg}^+$. *Phys. Rev. Lett.*, 102(1), 2009. URL <http://link.aps.org/doi/10.1103/PhysRevLett.102.013006>.
- [119] V. Batteiger, S. Knünz, M. Herrmann, G. Saathoff, H. Schüssler, B. Bernhardt, T. Wilken, R. Holzwarth, T. Hänsch, and Th. Udem. Precision spectroscopy of the 3S - 3P fine-structure doublet in Mg^+ . *Phys. Rev. A*, 80(2), 2009. URL <http://link.aps.org/doi/10.1103/PhysRevA.80.022503>.
- [120] F. Gebert, Y. Wan, F. Wolf, Angstmann C. N., Berengut J. C., and Schmidt P. O. Precision isotope shift measurements in Ca^+ using highly sensitive detection schemes. *preprint arXiv:1504.03139*, 2015. URL <http://arxiv.org/abs/1504.03139>. submitted for publication in *Phys. Rev. Lett.*
- [121] L. D. Landau and Lifshitz E. M. *Quantum Mechanics non-relativistic Theory, third edition*. Pergamon Press, Oxford, Great Britain, 1977.
- [122] Breit G. Theory of isotope shift. *Rev. Mod. Phys.*, 1958. URL <http://dx.doi.org/10.1103/RevModPhys.30.507>.
- [123] J. C. Berengut. *Isotope Shift and Relativistic Shift in Atomic Spectra*. PhD thesis, The University of New South Wales, 2006.
- [124] R. Engfer, H. Schneuwly, J. L. Vuilleumier, H. K. Walter, and A. Zehnder. Charge-distribution parameters, isotope shifts, isomere shifts, and magnetic hyperfine constants from muonic atoms. *At. Data Nucl. Data Tables*, (14):509–597, 1974. URL <http://www.sciencedirect.com/science/article/pii/S0092640X74800033>.
- [125] C. W. P. Palmer, P. E. G. Baird, S. A. Blundell, J. R. Brandenberger, C. J. Foot, D. N. Stacey, and G. K. Woodgate. Laser spectroscopy of calcium isotopes. *J. Phys. B*, 17(11):2197, 1984. URL <http://iopscience.iop.org/0022-3700/17/11/014>.
- [126] M. Drewsen, A. Mortensen, R. Martinussen, P. Staunum, and J. Sørensen. Nondestructive identification of cold and extremely localized single molecular ions. *Phys. Rev. Lett.*, 93(24), 2004. URL <http://link.aps.org/doi/10.1103/PhysRevLett.93.243201>.

- [127] Y.-W. Lin, S. Williams, and B. Odom. Resonant few-photon excitation of a single-ion oscillator. *Phys. Rev. A*, 87(1), 2013. URL <http://link.aps.org/doi/10.1103/PhysRevA.87.011402>.
- [128] M. Ramm, T. Pruttivarasin, M. Kokish, I. Talukdar, and H. Häffner. Precision measurement method for branching fractions of excited $P_{1/2}$ states applied to $^{40}\text{Ca}^+$. *Phys. Rev. Lett.*, 111(2), 2013. URL <http://link.aps.org/doi/10.1103/PhysRevLett.111.023004>.
- [129] H. D. Wohlfahrt, E. B. Shera, M. V. Hoehn, Y. Yamazaki, and R. M. Steffen. Nuclear charge distributions in $1f_{7/2}$ -shell nuclei from muonic x-ray measurements. *Phys. Rev. C*, 23:533–548, 1981. URL <http://link.aps.org/doi/10.1103/PhysRevC.23.533>.
- [130] M. Safronova and W. Johnson. Third-order isotope-shift constants for alkali-metal atoms and ions. *Phys. Rev. A*, 64(5), 2001. URL <http://link.aps.org/doi/10.1103/PhysRevA.64.052501>.
- [131] J. C. Berengut, V. A. Dzuba, V. V. Flambaum, J. A. King, M. G. Kozlov, M. T. Murphy, and J. K. Webb. Atomic transition frequencies, isotope shifts, and sensitivity to variation of the fine structure constant for studies of quasar absorption spectra. In *From Varying Couplings to Fundamental Physics*, pages 9–16. Springer, 2011. URL http://link.springer.com/chapter/10.1007/978-3-642-19397-2_2.
- [132] J. C. J. Koelemeij, B. Roth, and S. Schiller. Blackbody thermometry with cold molecular ions and application to ion-based frequency standards. *Phys. Rev. A*, 76:023413, 2007. URL <http://link.aps.org/doi/10.1103/PhysRevA.76.023413>.

ACKNOWLEDGMENTS

I would like to thank my supervisor Piet O. Schmidt for giving me the opportunity to work on this interesting and highly relevant topic and perform the measurements presented in this thesis. Additionally I would like to thank PD Dr. Ekkehard Peik and Prof. Dr. Klemens Hammerer for consenting in participating on my PHD examination board.

Furthermore I would like to thank my colleagues on the DIFCOS experiment where I especially thank Boerge Hemmerling for introducing me to and building up the beautiful experiment, on which the experiment presented here were performed. No less, I would like to thank my colleague Yong Wan for spending a lot of time with me in the lab and helping me with matlab functions I could not find. Additionally I would like to thank my successor at the experiment Fabian Wolf and Jan Christof Heip. I think the experiment will be in good hands.

I also would like to thank the all the people from the other experiments at the QUEST institute at PTB for fruitful and interesting discussions about diverse fields of physics. Especially I would like to thank Jannes B. Wübbena and Nils Scharnhorst who supported the work on the frequency measurements by collaborating on setting up the laser stabilization of the spectroscopy lasers and discussing how to build up the stabilization appropriately. Furthermore, I would like Ian D. Leroux for fruitful discussions of the underlying theories of the experiments we performed.

All this work would not be possible without the work provided by the mechanical and electronic workshop in the institute. I would like to thank Christopher Bleuel, Julia-Aileen Fenske, Olga Lick, Sven Klitzing, Rebecca Müller, and Alexander Pablocki for their competent help on electronic and mechanical setups. Especially I would like to thank Peter Christian Carstens who always took the time to explain the basics of electronic circuits and helped us when problems occurred in the laboratory.

I would like to thank our coworkers in the collaborations. Here I would like to thank Michael Frosz for interesting discussions and providing more inside into the fields of photonic crystal fibers. Furthermore I would like to thank Julian Berengut for interesting discussions and for introducing me to isotope shift theory and atomic structure calculations.

In addition I would like to thank Harald Telle for being my PTB-Mentor and for proof reading the thesis. I also acknowledge the hours my wife, Yong Wan, Nils Scharnhorst and Fabian Wolf spend for

proof reading parts of the thesis.

CURRICULUM VITAE

Personal details

Name	Florian Gebert
Date of birth	26.06.1980
Place of birth	Braunschweig
Marital status	married

Education

since 03/2010	Physikalisch-Technische Bundesanstalt & Leibniz University of Hannover, Germany Graduate student at the QUEST Institute for Experimental Quantum Metrology Thesis topic: <i>Precision measurement of the isotopic shift in calcium ions using photon recoil spectroscopy</i>
2009-2010	University of Braunschweig, Germany Research assistant
2003-2009	University of Braunschweig, Germany Student of physics Thesis topic: <i>Ramanspektroskopische Untersuchungen einiger komplexer Metallhydride</i>
2000-2003	University of Braunschweig, Germany Student of engineering
1999-2000	Hospital Herzogin-Elizabeth-Heim, Germany Civil service
1999	Neue Oberschule Braunschweig, Germany Abitur

COLOPHON

This document was typeset using the typographical look-and-feel `classicthesis` developed by André Miede. The style was inspired by Robert Bringhurst's seminal book on typography "*The Elements of Typographic Style*". `classicthesis` is available for both \LaTeX and \LyX :

<http://code.google.com/p/classicthesis/>

Happy users of `classicthesis` usually send a real postcard to the author, a collection of postcards received so far is featured here:

<http://postcards.miede.de/>

Final Version as of May 7, 2015 (`classicthesis` version 1.0).